Computational physics from simple to complex systems

Dissertation
zur Erlangung des Doktorgrades
der Naturwissenschaften
(Dr. rer. nat.)

dem
Fachbereich Chemie
der Philipps-Universität Marburg
vorgelegt von
Edgar Martin
aus
Hermannstadt/Rumänien

Marburg/Lahn 2009

Vom Fachbereich Chemie der Philipps-Universität Marburg als Dissertation am 12.03.2009 angenommen.

Erster Gutachter: Prof. Dr. Guido Germano

Zweiter Gutachter: Prof. Dr. Enrico Scalas

Tag der mündlichen Prüfung: 19.03.2009

Contents

Zusammenfassung

Diese Arbeit befasst sich mit Computersimulationen und analytischen Rechnungen in einfachen und komplexen Systemen. In den letzten Jahrzehnten ist viel auf dem Gebiet der Komplexitätstheorie geforscht worden, und es gibt zahlreiche Definitionen von Komplexität. In dieser Arbeit wird das Attribut komplex aufgrund zweier Aspekte vergeben: Einerseits sprechen wir von einem komplexen System, wenn es sich aus vielen untereinander wechselwirkenden einfachen Systemen zusammensetzt. Aus dieser Perspektive ist jedes von uns betrachtete System komplex, allerdings ist die Klassifizierung eine andere, wenn es sich um Fluide handelt. Man unterscheidet in diesem Fall, indem man die Komplexität der intermolekularen Wechselwirkungspotentiale als Kriterium benutzt. So werden Fluide mit isotropen Wechselwirkungen, wie etwa Lennard-Jones Systeme, als einfache Fluide bezeichnet, im Gegensatz zu Flüssigkristallen, die anisotrop miteinander wechselwirken.

Nachdem in den ersten drei Kapiteln grundlegende Begriffe aus der statistischen Mechanik, der Theorie der stochastischen Prozesse und der Molekulardynamik-Computersimulation (MD) wiederholt werden, werden diese Methoden in den darauf folgenden Kapiteln systematisch auf Systeme mit steigender "Komplexität" angewendet. In den Kapiteln 4 und 5 sind die Fragestellungen fundamentaler Natur: Die Ehrenfest-Urne ist ein Modell, das zur Erklärung der vom Boltzmannschen H-Theorem postulierten Irreversibilität der makroskopischen Thermodynamik, die wiederum im Widerspruch zur mikroskopischen Zeitreversibilität steht, eingeführt worden ist. Nachdem in Kapitel 4 die Definition und Herleitung der Boltzmannschen Zustandsfunktion wiederholt wird, wird im Kapitel 5 das Modell der Ehrenfest-Urne mit Hilfe von MD-Simulationen an einem realen Fluid analysiert, und es stellt sich heraus, dass die für die statistische Mechanik fundamentale Markov-Hypothese [1] nicht nur in einem Gas, sondern selbst in der flüssigen Phase gültig ist.

Im Kapitel 6 werden flüssigkristalline Systeme behandelt. Nach der Einführung der grundlegenden Begriffe wird ein in einer zylindrischen Nanopore eingeschlossenes diskotisches System simuliert. Diskotische Flüssigkristalle sind aus technischer Sicht interessant, da man sich aufgrund der anisotropen Leitfähigkeit in der kolumnaren Phase Anwendungsmöglichkeiten wie organische Leuchtdioden und Feldeffekttransistoren verspricht.

Schließlich werden im Kapitel 7 "First Passage Times" für einen stochastischen Prozess, der für viele physikalische, chemische, biologische und andere Probleme relevant ist, analytisch berechnet und numerisch simuliert.

Abstract

This thesis deals with computer simulations and analytical calculations in simple and complex systems. In the last decades there has been a great interest in the area of complexity, and there are numerous definitions of complexity. In this work the attribute complex will be given based on two criteria. On the one hand we shall call a system "complex" if it is composed of a great number of simple interacting systems. Regarded from this perspective, every system we consider is complex, however on the other hand the classification is different when dealing with fluids. In this case one distingushes between simple and complex fluids using the interaction potentials as a criterion. Fluids with isotropic intermolecular potentials like Lennard-Jones systems are referred to as simple fluids, whereas e.g. liquid crystals belong to the class of complex fluids due to their anisotropic interaction potentials.

After explaining some basic notions of statistical mechanics the theory of stochastic processes and molecular dynamics computer simulations, these methods are applied systematically to systems with increasing "complexity" in the next chapters. In Chapters 4 and 5 the discussed problems are of a fundamental nature: The Ehrenfest urn is a model introduced in order to explain the irreversibility of macroscopic thermodynamics as stated by Boltzmann's H-theorem, although resulting from a time-reversible microscopic dynamics. After reviewing the defintition and derivation of Boltzmann's state function in Chapter 4, the model of the Ehrenfest urn is studied via MD simulations of a realistic fluid in Chapter 5, and it turns out that the Markov hypothesis lying at the foundations of statistical mechanics [1] is valid even in the liquid phase.

In Chapter 6 liquid crystalline systems are studied. After introducing basic notions a discotic system confined in a cylindrical nanopore is simulated. Discotic liquid crystals are interesting from a technical point of view, since, due to their anisotropic conductivity in the columnar phase, they are promising for applications like organic light emiting diodes field effect transistors and solar cells.

Finally in Chapter 7 first passage times for a stochastic process relevant for many physical chemical biological and other problems are calculated analytically and simulated numerically.

Introduction

Complexity results from the sum of a large number of simple steps. This is my intuition. There are certainly many people who are much more intelligent than me and recognized that, or believed to recognize it as I do, long before I was born. Of course this statement is not always true, and there are physical problems that have been solved using approaches that do not correspond to our daily experience of the real world, which is also due to our limited observation capabilities. Two famous examples are the derivation of Planck's law of black body radiation, where the quantization of the energy is postulated, and Einstein's special relativity theory, which employs a metric tensor different from the intuitive Euclidean one we know in our every day life. There is a variety of definitions of complexity, since the area of complexity and chaos research has been constantly growing in the last decades. Here is the definition proposed by Nigel Goldenfield and Leo Kadanoff [2]:

> *To us, complexity means that we have structure with variations. Thus, a living organism is complex because it has many different working parts, each formed by variations in the working out of the same genetic coding. One look at ocean or sky gives the conviction that there is some natural tendency toward the formation of structure in the physical world. Chaos is also found very, very frequently. Chaos is the sensitive dependence of a final result upon the initial conditions that bring it about. In a chaotic world, it is hard to predict which variation will arise in a given place and time. In fact, errors and uncertainties often grow exponentially with time. A complex world is interesting, because it is highly structured. A chaotic world is interesting because we do not know what is coming next. But the world contains regularities as well. For example, climate is very complex, but winter follows summer in a predictable pattern. Our world is both complex and chaotic.*

In this thesis complexity will be discussed in the context of studying the behaviour of systems composed of many interacting parts. In this sense all systems mentioned in this work can be regarded as complex. However, for instance in the case of liquids one speaks of simple or complex fluids depending on the nature of the interactions of the constituent molecules. Thus spherically symmetric molecules with isotropic intermolecular interactions are called simple fluids, and non-spherical particles with a shape and energy anisotropy like liquid crystals belong to the class of complex fluids.

Statistical mechanics was the first theory that attempted to calculate macroscopic properties of systems composed of many interacting particles using probabilistic methods, where a sophisticated analysis is developed starting from simple hypotheses. Although more than a century has passed since the pioneering works

of Maxwell, Boltzmann and Gibbs in the area of equilibrium statistical physics, the latter is still a developing field. A modern approach to statistical physics reformulates it in the language of stochastic processes, which is a subject of intensive mathematical research itself. In Chapters 1 and 2 the basics of statistical mechanics and stochastic processes are briefly reviewed.

Computer simulations are an increasingly important tool in physics, especially in condensed matter physics, where many-particle systems are investigated on a molecular scale. They allow to validate theories and can be considered as a bridge between theory and experiment. For the simulation of classical many-particle systems mainly two different approaches are used, the *Monte Carlo* (MC) and the *molecular dynamics* (MD) method. The former is based on the principle of statistical ensembles in the spirit of Gibbs, where the probability density of the ensemble of interest is used to sample the phase space of the system. The latter integrates Hamilton's equations of motion: The particle-system is treated as a dynamic system and the employed integration algorithm (integrator) can be regarded as a discretized flow in phase space. This point of view leads to the Liouville formulation of the velocity-Verlet integrator that is consistent with the symplectic structure of Hamilton's formulation of classical mechanics. The velocity-Verlet integrator is introduced in chapter 3, where MD simulations are treated in some detail because it is the computational method used most frequently in this work. An advantage of MD as compared MC is the possibility to compute dynamical features like mean square displacements ans velocity-autocorrelations. A combination of the two methods is also possible: hybrid MC.

Chapters 4 and 5 deal with foundational problems of statistical mechanics. Boltzmann's famous H-theorem states the increase of entropy of an ideal gas as an irreversible process. In Chapter 4 the definition of this thermodynamic state function and the derivation of the H-theorem is presented. Boltzmann's H is a forerunner of Shannon's entropy, which is an important quantity in information theory. It is also called self-information and is a measure to the uncertainty associated with a random variable, representing an absolute limit of the best lossless compression of data. In order to explain the irreversiblity of thermodynamics stated by the H-theorem, which is in contradiction to the time-reversible dynamics arising from Hamilton's canonical equations of motion, the Ehrenfests introduced their famous urn model. In Chapter 5 the Ehrenfest urn is studied for a realistic Lennard-Jones fluid, and the Markov hypothesis stated by Penrose [1] lying at the foundations of statistical mechanics is found to be valid even in a realistic liquid phase, although the analysis of the Ehrenfest urn applies to the gaseous phase only. MD simulations are carried out using the time-reversible velocity-Verlet integrator, that approximates the time-reversible Lagrangian and Hamiltonian mechanics. This is also the first chapter that represents original research results.

A liquid crystalline system is more complex than a Lennard-Jones fluid because the anisotropy of the constituent molecules breaks the rotational invariance and thus increases the dimensionality of phase space. In Chapter 6 liquid crystals are studied, where the emphasis lies on the simulation of discotic liquid crystals in a cylindrical confinement. This is especially interesting because confinement provides the possibility to control the alignment of the discs on a macroscopic scale, making them available for technical applications like light emitting diodes, field effect transistors and photovoltaic cells.

As mentioned before, statistical mechanics can be studied in the language of stochastic processes, that provides a very powerful tool. For example diffusion in liquids can be studied as a first passage problem. In Chapter 7 first passage time probability densities for a stochastic process that is relevant for many problems in physics, chemistry biology, and also finance are computed analytically and numerically.

Chapter 1

Basic statistical mechanics

1.1 State of a system

In classical mechanics the state of a system consisting of N particles can be specified by the Cartesian coordinates $x_1, \ldots, x_{3N}$ and the corresponding velocities $\dot{x}_1, \ldots, \dot{x}_{3N}$ if there are no constraints and no internal degrees of freedom are included. In general the state of a system with f degrees of freedom is described by the generalized positions $q_1, \ldots, q_f$ and the generalized velocities $\dot{q}_1, \ldots, \dot{q}_f$. According to Lagrange's formalism, one considers the function

$$\mathcal{L}(q_1, \ldots, q_f, \dot{q}_1, \ldots, \dot{q}_f, t) = T(\dot{q}_1, \ldots, \dot{q}_f) - U(q_1, \ldots, q_f, \dot{q}_1, \ldots, \dot{q}_f, t), \tag{1.1}$$

where T and U are the kinetic and the potential energy of the system. A calligraphic letter is used for the Lagrange function to avoid confusion with the Liouville operator introduced later. In general, the potential energy can also depend on the generalized velocities but we shall restrict to the case of a position dependent potential and a Lagrangian that has no explicit time dependence. Starting from Hamilton's principle, i.e. the variational equation

$$\delta \int_{t_1}^{t_2} \mathcal{L}\, dt = 0, \tag{1.2}$$

the equations of motion can be written in the form of the Euler-Lagrange equations

$$\frac{d}{dt}\frac{\partial \mathcal{L}}{\partial \dot{q}_i} - \frac{\partial \mathcal{L}}{\partial q_i} = 0, \quad i = 1, \ldots, f. \tag{1.3}$$

Defining the generalized momenta $p_i = \partial \mathcal{L}/\partial \dot{q}_i$, the Hamilton function H is obtained via the Legendre transformation $H = \sum_{i=1}^{f} p_i \dot{q}_i - \mathcal{L}$, and identified with the total energy of the system:

$$H(q_1, \ldots, q_f, p_1, \ldots, p_f) = T(p_1, \ldots, p_f) + U(q_1, \ldots, q_f). \tag{1.4}$$

Thus the Euler-Lagrange equations given by the system of f second-order differential equations (1.3) can be replaced by a system of $2f$ first-order differential equations, Hamilton's canonical equations of motion:

$$\begin{aligned} \dot{q}_i &= \frac{\partial H}{\partial p_i} \\ \dot{p}_i &= -\frac{\partial H}{\partial q_i}, \quad i = 1, \ldots, f. \end{aligned} \tag{1.5}$$

The generalized positions q_i and the corresponding momenta p_i are called canonically conjugated variables, and, corresponding to Hamilton's formalism, the state of a system obeying the laws of classical mechanics is specified by the generalized positions $q_1, \ldots, q_f$ and their canonical conjugate momenta $p_1, \ldots, p_f$.

1.2 Phase space and ensemble

The geometrical concept of the phase space plays a central role in statistical mechanics. For a system with f degrees of freedom it is defined as the space consisting of the vectors $\mathbf{x} = (q_1, \ldots, q_f, p_1, \ldots, p_f)$, where the entries are the generalized coordinates q_i and the generalized momenta p_i. Hence every element of the phase space can be identified with a state of the system defined in the previous section. In this formalism the system (1.5) can be written in symplectic notation as follows:

$$\frac{d\mathbf{x}}{dt} = \mathbf{J}\,\frac{\partial H}{\partial \mathbf{x}} \tag{1.6}$$

with

$$\mathbf{J} = \begin{pmatrix} \mathbf{0} & \mathbf{1} \\ -\mathbf{1} & \mathbf{0} \end{pmatrix}, \tag{1.7}$$

where $\mathbf{0}$ is the $f \times f$ zero matrix and $\mathbf{1}$ is the $f \times f$ unity matrix.

It is often convenient to adopt the terminology of the Ehrenfests [3], where one distinguishes between the Γ-space and the μ-space. The former is the phase space for the system as a whole as defined above, whereas the latter denotes the phase space for any individual particle of the system. For example the μ-space of a particle with r degrees of freedom is spanned by the vectors $\mathbf{x} = (q_1, \ldots, q_r, p_1, \ldots, p_r)$. The most complete description of a system is provided by a single point in Γ-space. Equivalently the system can be described by the number of particles lying in a certain region of the μ-space.

Instead of considering the system of interest only, and following the movement of the corresponding point $\mathbf{x} = (q_1, \ldots, q_f, p_1, \ldots, p_f)$ in the Γ-space in time, it is useful to regard a large number of systems of the same structure, an ensemble of systems. Thermodynamic quantities can then be computed by averaging over all the systems belonging to the ensemble rather then averaging the properties of the single system of interest over many instants of time.

1.3 The principle of equal *a priori* probabiltities

The typical problem in statistical mechanics is to find the macroscopic properties of a system with a large number of degrees of freedom. The most accurate way to do this would be the integration of the equations of motion of all the composing particles, which is unfeasible because of the limited knowledge of the initial conditions and of the limited computing power.

For this reason a probabilistic hypothesis of equal *a priori* probabilities is introduced, stating that every *accessible* state the system could occupy is equally likely to occur. The question of accessibility is connected to the macroscopic boundary conditions and leads to different kinds of ensembles.

1.4 Density function and ergodicity

Defining a point in Γ-space the way we did above, the time average of a quantity $f(\mathbf{x}, t)$ depending on all generalized positions and momenta, and possibly explicitly on time t, reads

$$\bar{f} = \lim_{T\to\infty} \frac{1}{T} \int_{t_0}^{t_0+T} f(\mathbf{x}, t)\, dt, \tag{1.8}$$

where the mean is taken over all the values lying in the time interval $(t_0, t_0 + T)$.

For the ensemble average a density function $\rho(\mathbf{x}, t)$, which in general will depend on the ensemble, is needed. Once it is given, the ensemble average $\langle f \rangle$ can be computed:

$$\langle f \rangle = \int f(\mathbf{x}, t)\rho(\mathbf{x}, t)\, d\mathbf{x}, \tag{1.9}$$

The two ways of computing averages leads to the concept of ergodicity. The original definition is due to Boltzmann and states that a system is called ergodic, if its trajectory $\mathbf{x}(t)$ passes arbitrarily close to every available point in phase space. A consequence of ergodicity is that the averages given by Eqs. (1.8) and (1.9) are equal.

1.5 Statistical ensembles

In this section the four most commonly used ensembles will be shortly revieved.

1.5.1 Microcanonical ensemble

The simplest ensemble is the microcanonical ensemble. It represents a system with a constant number of particles N and a constant volume V at a constant energy E, which is isolated i.e. unable to exchange either energy or matter with the rest of the universe.

In this case the accessible states are all those lying in the infinitesimal interval $(E, E + dE)$, or the set $\Omega = \{\mathbf{x} : E < H(\mathbf{x}) < E + dE\}$. Corresponding to the principle of equal *a priori* probabilities, the equilibrium density function in the microcanonical ensemble is given by

$$\rho(\mathbf{x}) = \frac{\delta(H(\mathbf{x}) - E)}{\mu(\Omega)}, \tag{1.10}$$

where $\mu(\Omega)$ is the volume (the measure) of the available phase space Ω.

1.5.2 Canonical ensemble

The canonical ensemble describes a system with a constant number of particles N in a constant volume V coupled to a heat bath keeping it at a constant temperature T. The system is allowed to exchange heat with the bath, but no matter. The probability density function in this ensemble reads

$$\rho(\mathbf{x}) = \frac{h^{-fN}}{N!} \frac{e^{-\beta H(\mathbf{x})}}{Q}, \tag{1.11}$$

where the normalizing factor Q is the canonical partition function defined by

$$Q = \frac{h^{-fN}}{N!} \int_\Gamma e^{-\beta H(\mathbf{x})}\, dv_\Gamma. \tag{1.12}$$

Here we have defined the volume element in Γ-space by $dv_\Gamma = dq_1 \cdots dq_f dp_1 \cdots dp_f$, $\beta = 1/k_\mathrm{B}T$ and h is Planck's constant.

1.5.3 Isothermal-isobaric ensemble

The isothermal-isobaric ensemble is an ensemble describing a system composed of N particles at constant pressure P and constant temperature T, and is characterized by the probability density function

$$\rho(\mathbf{x}) = \frac{h^{-fN}}{N!} \frac{e^{-\beta H(\mathbf{x}) - \beta PV}}{\Delta}, \tag{1.13}$$

with the partition function

$$\Delta = \frac{h^{-fN}}{N!} \int \int_\Gamma e^{-\beta H(\mathbf{x}) - \beta PV}\; dv_\Gamma\, dV. \tag{1.14}$$

It is interesting to note that the isothermal-isobaric partition function is the Laplace transform of the canonical partition function with respect to the volume.

1.5.4 Grand canonical ensemble

In the grand canonical ensemble the number of particles is allowed to fluctuate, keeping the system at a constant chemical potential μ, a constant volume V and a constant temperature T. The probability density is

$$\rho(\mathbf{x}) = \frac{h^{-fN}}{N!} \frac{e^{N\beta\mu} e^{-\beta H(\mathbf{x})}}{\Xi}, \tag{1.15}$$

where Ξ is the grand canonical partition function

$$\Xi = \sum_{N=0}^{\infty} \frac{h^{-fN}}{N!} e^{N\beta\mu} \int_\Gamma e^{-\beta H_N(\mathbf{x})}\, dv_\Gamma = \sum_{N=0}^{\infty} e^{N\beta\mu} Q(N). \tag{1.16}$$

1.6 Evolution in phase space

Given a quantity $f(\mathbf{x}, t)$ depending on the generalized positions, the generalized momenta and the time, its time derivative is given by

$$\begin{aligned} \frac{df}{dt} &= \frac{\partial f}{\partial \mathbf{x}} \cdot \frac{d\mathbf{x}}{dt} + \frac{\partial f}{\partial t} \\ &= \sum_{i=1}^{f} \left(\frac{\partial f}{\partial q_i} \frac{dq_i}{dt} + \frac{\partial f}{\partial p_i} \frac{dp_i}{dt} \right) + \frac{\partial f}{\partial t} \\ &= \sum_{i=1}^{f} \left(\frac{\partial f}{\partial q_i} \frac{\partial H}{dp_i} - \frac{\partial f}{\partial p_i} \frac{\partial H}{dq_i} \right) + \frac{\partial f}{\partial t}. \end{aligned} \tag{1.17}$$

In the first line the dot is an inner product, and Hamilton's equations (1.5) are used to go from the second to the third line. Using the definition of a Poisson bracket,

$$\{f, g\} = \sum_{i=1}^{f} \left(\frac{\partial f}{\partial q_i} \frac{\partial g}{\partial p_i} - \frac{\partial f}{\partial p_i} \frac{\partial g}{\partial q_i} \right), \tag{1.18}$$

Eq. (1.17) can be written as

$$\frac{df}{dt} = \{f, H\} + \frac{\partial f}{\partial t}. \tag{1.19}$$

1.7 Liouville equation

A fundamental theorem in statistical mechanics is Liouville's equation, which describes the time evolution of the phase space density function $\rho(\mathbf{x}, t)$. The total time derivative takes the form of a generalized continuity equation and is given in accordance with the previous section by:

$$\frac{d\rho}{dt} = \frac{\partial \rho}{\partial t} + \sum_{i=1}^{f} \left(\frac{\partial \rho}{\partial q_i} \dot{q}_i + \frac{\partial \rho}{\partial p_i} \dot{p}_i \right) = 0. \tag{1.20}$$

Inserting Hamilton's equations (1.5), and using the definition of the Poisson brackets (1.18), the Liouville equation takes the form:

$$\frac{\partial \rho}{\partial t} = -\{ \rho, H \} = \{ H, \rho \}. \tag{1.21}$$

The physical interpretation of the Liouville equation is that a cloud of moving points in Γ-space, each of which represents a system belonging to the ensemble, behaves like an incompressible fluid; in other words, the occupied volume in Γ-space is constant in time.

Chapter 2

Stochastic processes

Since the work of Einstein and Smoluchowsky on Brownian motion, stochastic processes have played an increasingly important role in physics. Basic concepts like the Chapman-Kolmogorov equation, the Langevin equation, the Fokker-Planck equation and the Markov property arose from these early considerations. In this section some basics of these concepts are briefly sketched. We shall not be concerned about mathematical accuracy, for which terms like probability space, σ-algebra and measures have to be introduced, but rather appeal to intuition.

A stochastic process is a process that evolves probabilistically in time, or, in other words, a process described by a time-dependent random variable $X(t)$. Sampling the values of $x_1, \ldots, x_n$ at times $t_1, \ldots, t_n$, with $t_1 \leq t_2 \leq \cdots \leq t_n$, the process is determined by the joint probability density $f(x_1, t_1; \ldots; x_n, t_n)$, i.e. the probability that $X(t_i) \in (x_i, x_i + dx)$ for all $i \in \{1, \ldots, n\}$ is given by $f(x_1, t_1; \ldots; x_n, t_n) dx_1 \ldots dx_n$. The joint probability density can be written in terms of conditional probability densities:

$$\begin{aligned} f(x_n, t_n; \ldots; x_1, t_1) &= f(x_n, t_n | x_{n-1}, t_{n-1}; \ldots; x_1, t_1) \\ &\quad \times f(x_{n-1}, t_{n-1} | x_{n-2}, t_{n-2}; \ldots; x_1, t_1) \ldots \\ &\quad \times f(x_2, t_2 | x_1, t_1) f(x_1, t_1). \end{aligned} \tag{2.1}$$

2.1 Independence

The simplest stochastic process is determined by stochastic independence, which means, that the process is entirely independent of its previous history. Mathematically this has the consequence that the density function factorizes:

$$f(x_1, t_1; \ldots; x_n, t_n) = \prod_{i=1}^{n} f(x_i, t_i). \tag{2.2}$$

2.2 Markov processes

A *Markov process* is the simplest generalization of an independent process. The *Markov property* states that the present value of the process is only determined by the last value in the past, and the rest of the history does not matter. This can again be expressed in terms of conditional probability densities:

$$f(x_n, t_n | x_{n-1}, t_{n-1}; \ldots; x_1, t_1) = f(x_n, t_n | x_{n-1}, t_{n-1}). \tag{2.3}$$

With the Markov assumption Eq. (2.1) becomes

$$f(x_n,t_n;\ldots;x_1,t_1) = f(x_n,t_n|x_{n-1},t_{n-1})f(x_{n-1},t_{n-1}|x_{n-2},t_{n-2}) \times \ldots f(x_2,t_2|x_1,t_1)f(x_1,t_1). \quad (2.4)$$

2.3 Chapman-Kolmogorov equation

Given the joint probability density $f(x_2,t_2;x_1,t_1)$, the marginal density function $f(x_2,t_2)$ can be obtained integrating over the discarded variable x_1:

$$\begin{aligned} f(x_2,t_2) &= \int_{-\infty}^{\infty} f(x_2,t_2;x_1,t_1)\,dx_1 \\ &= \int_{-\infty}^{\infty} f(x_2,t_2|x_1,t_1)f(x_1,t_1)\,dx_1, \end{aligned} \quad (2.5)$$

where Eq. (2.1) has been used in the second line. The same procedure can be applied to a conditional probability density. Sampling a process at the times $t_1 \leq t_2 \leq t_3$, one gets the conditional probability density $f(x_3,t_3|x_1,t_1)$ by integrating over all possible intermediate values x_2:

$$\begin{aligned} f(x_3,t_3|x_1,t_1) &= \int_{-\infty}^{\infty} f(x_3,t_3;x_2,t_2|x_1,t_1)\,dx_2 \\ &= \int_{-\infty}^{\infty} f(x_3,t_3|x_2,t_2;x_1,t_1)f(x_2,t_2|x_1,t_1)\,dx_2. \end{aligned} \quad (2.6)$$

Inserting the Markov property (2.3), one obtains the Chapman-Kolmogorov equation:

$$f(x_3,t_3|x_1,t_1) = \int_{-\infty}^{\infty} f(x_3,t_3|x_2,t_2)f(x_2,t_2|x_1,t_1)\,dx_2. \quad (2.7)$$

2.4 Wiener process

The Wiener process W_t or Brownian motion is one of the fundamental stochastic processes. Physically, the process can be interpreted as the fast and irregular motion of a large particle undergoing random collisions with many smaller particles. Einstein [4] has shown that the probability density $f(x,t)$ of the position of the Brownian particle obeys the well-known diffusion equation or Fick's second law

$$\frac{\partial f(x,t)}{\partial t} = D\frac{\partial^2 f(x,t)}{\partial x^2}, \quad (2.8)$$

that can be derived from Fick's first law with the diffusion coefficient D and the continuity equation.

In order to describe the one-dimensional Wiener process properly in a mathematical way, the normal distribution has to be introduced. To indicate that a real-valued random variable X is normally distributed with mean μ and variance σ^2, one writes:

$$X \sim N(\mu,\sigma^2), \quad (2.9)$$

and the corresponding probability density is:

$$f(x) = \frac{1}{\sigma\sqrt{2\pi}}\, e^{-\frac{(x-\mu)^2}{2\sigma^2}}. \tag{2.10}$$

The *central limit theorem* states that the distribution of the sum of a large number of independent and identically distributed random variables withe finite second moments converges towards a normal distribution. The Wiener process can then be characterized by the following properties:

1. $W_0 = 0$.
2. W_t is almost surely continuous.
3. W_t has independent increments with probability density $W_t - W_s \sim \mathcal{N}(0, 2D(t-s))$ for $0 \leq s < t$.

Using these properties it is clear that $f(x,t|x_0,0) \sim \mathcal{N}(0,2Dt)$ is a solution of Eq. (2.8) assuming the initial condition $f(x,0|x_0,0) = \delta(x-x_0)$. Rather than using the probability density to describe the random process, one can use the particle's position itself coupled to a source of randomness, which was first done by Langevin. Physicists often express this by an ordinary differential equation,

$$\dot{x} = \frac{dx}{dt} = \xi(t), \tag{2.11}$$

where ξ is the so-called white noise, which is a random variable with zero mean and correlation function $\langle \xi(t)\xi(t')\rangle = \delta(t-t')$. However, it must be bourne in mind that this differential equation can only have symbolic character since the paths of the Brownian motion are nowhere differentiable and the variance is not finite. Formally the Wiener process can be described by its increments. From Eq. (2.11)

$$dX_t = \xi(t)dt = dW_t, \tag{2.12}$$

and the solution is

$$\begin{aligned} X_t &= X_0 + \int_0^t dW_s \\ &= X_0 + W_t - W_0 = X_0 + W_t. \end{aligned} \tag{2.13}$$

A *stochastic* integral has to be defined in order to perform these calculations. This cannot be done in a unique way; the two conventions of Itô and Stratonovich [5] are the most useful.

2.5 Langevin equation

The Wiener process as described by Eq. (2.12) is the simplest example of a Langevin equation. The generalization to the n-dimensional case with an external field acting on the diffusing particle is

$$d\mathbf{X}_t = \boldsymbol{\mu}(\mathbf{X}_t, t)dt + \boldsymbol{\sigma}(\mathbf{X}_t, t)d\mathbf{W}_t, \tag{2.14}$$

where the vector $\boldsymbol{\mu}$ with the components μ_i is the deterministic part of the process responsible for the drift and $\boldsymbol{\sigma}$ is a $n \times n$-matrix with the components σ_{ij} determining the diffusion. As already mentioned in the previous section, this is a symbolic notation used as a shorthand for an integral equation:

$$\mathbf{X}_t = \mathbf{X}_{t_0} + \int_{t_0}^{t} \boldsymbol{\mu}(\mathbf{X}_s, s) ds + \int_{t_0}^{t} \boldsymbol{\sigma}(\mathbf{X}_s, s) d\mathbf{W}_s, \tag{2.15}$$

where we have assumed that the process starts at $\mathbf{X}_{t_0}$. The first integral is an ordinary Riemann integral, the second one a stochastic integral.

2.6 Fokker-Planck equation

Under certain assumptions the Fokker-Planck equation can be derived from the Chapman-Kolmogorov equation (2.7). Fokker was a PhD student of Planck working on Brownian motion in a radiation field. For a more thorough discussion of this topic reference [5] is recomended. In one dimension the Fokker-Planck equation reads

$$\frac{\partial}{\partial t} f(x,t|x_0,t_0) = -\frac{\partial}{\partial x}\left[\mu(x,t) f(x,t|x_0,t_0)\right] + \frac{1}{2}\frac{\partial^2}{\partial x^2}\left[\sigma^2(x,t) f(x,t|x_0,t_0)\right], \tag{2.16}$$

where μ is the so-called drift term and $\sigma^2/2$ is the diffusion term. In absence of the drift term the Fokker-Planck equation is equal to the diffusion equation (2.8) with $\sigma^2 = 2D$. The generalization of Eq. (2.16) to an n-dimensional stochastic process $\mathbf{X}(t)$ is

$$\begin{aligned} \frac{\partial f(\mathbf{x},t|\mathbf{x}_0,t_0)}{\partial t} &= -\frac{\partial}{\partial \mathbf{x}} \cdot \left[\boldsymbol{\mu}(\mathbf{x},t) f(\mathbf{x},t|\mathbf{x}_0,t_0)\right] \\ &+ \frac{1}{2}\frac{\partial}{\partial \mathbf{x}} \cdot \left[\left(\frac{\partial}{\partial \mathbf{x}}\right)^{\mathsf{T}} \left(\boldsymbol{\sigma}(\mathbf{x},t)\boldsymbol{\sigma}^{\mathsf{T}}(\mathbf{x},t) f(\mathbf{x},t|\mathbf{x}_0,t_0)\right)\right], \end{aligned} \tag{2.17}$$

where $\boldsymbol{\mu}$ is the the drift vector and $\frac{1}{2}\boldsymbol{\sigma}(\mathbf{x},t)\boldsymbol{\sigma}^{\mathsf{T}}(\mathbf{x},t)$ the diffusion tensor, which results from the presence of the stochastic force. If the diffusion tensor is zero there is no stochastic component, and Eq. (2.17) reduces to the Liouville equation (1.21).

Chapter 3

Molecular dynamics simulations

In statistical mechanics only a few problems like the ideal gas or the perfect crystal are exactly solvable, in the sense that macroscopic properties can be worked out mathematically from simple assumptions. Computer simulation provides us with a powerful tool to compute macroscopic material properties and to check the validity of existing theories for everything in between these two extremes, i.e. fluids. One of the first achievements of computer simulations was the demonstration that a system of hard spheres undergoes a first order freezing transition, which was done by Alder and Wainwright [6] and Wood and Jacobson [7]. The first simulation of a real liquid, namely argon, was performed by Rahman [8].

3.1 The idea of molecular dynamics

The idea of molecular dynamics (MD) is simple. Given a system of N particles, instead of getting information about macroscopic properties via probabilistic assumptions and performing ensemble averages, we can follow the trajectory of a point in phase space and then calculate time averages, assuming that the system is ergodic.

For a wide range of materials it is a good approximation, if the constituent molecules of the system are considered to obey the laws of classical mechanics. Therefore many problems can be tackled using classical MD, i.e. integrating numerically Newton's equations of motion

$$\ddot{\mathbf{r}}_i = \frac{\mathbf{f}_i}{m} = -\frac{1}{m}\nabla_{\mathbf{r}_i} U(\mathbf{r}_1, \ldots, \mathbf{r}_N) \equiv \frac{1}{m}\frac{\partial}{\partial \mathbf{r}_i} U(\mathbf{r}_1, \ldots, \mathbf{r}_N). \tag{3.1}$$

Here $\mathbf{f}_i$ is the force acting on particle i, which, for a conservative system, can be derived from a potential.

Numerical integration means discretisation of the time axis; the system is propagated by a small time step Δt. One of the simplest integration algorithms is the so-called Verlet algorithm [9], which can be deduced from a Taylor expansion. The coordinates of an arbitrary molecule at time $t + \Delta t$ can be expanded around the coordinates at t:

$$\mathbf{r}_i(t + \Delta t) = \mathbf{r}_i(t) + \mathbf{v}_i(t)\Delta t + \frac{\mathbf{f}_i(t)}{2m}\Delta t^2 + \frac{1}{3!}\frac{\partial^3 \mathbf{r}_i}{\partial t^3}\Delta t^3 + \mathcal{O}\left(\Delta t^4\right), \tag{3.2}$$

where $\mathbf{v}_i$ is the velocity of particle i. Similarily, an expansion of the coordinates at an earlier instant of time $t - \Delta t$ delivers

$$\mathbf{r}(t - \Delta t) = \mathbf{r}_i(t) - \mathbf{v}_i(t)\Delta t + \frac{\mathbf{f}_i(t)}{2m}\Delta t^2 - \frac{1}{3!}\frac{\partial^3 \mathbf{r}_i}{\partial t^3}\Delta t^3 + \mathcal{O}\left(\Delta t^4\right). \tag{3.3}$$

Summing Eq. (3.2) and Eq. (3.3) we get

$$\mathbf{r}_i(t + \Delta t) = 2\mathbf{r}_i(t) - \mathbf{r}_i(t - \Delta t) + \frac{\mathbf{f}_i(t)}{m}\Delta t^2 + \mathcal{O}\left(\Delta t^4\right). \tag{3.4}$$

Thus we have a prescription how to compute the positions of the molecules at the time $t + \Delta t$ with an accuracy of order $\mathcal{O}(\Delta t^4)$, knowing the positions at the two earlier instants of time t and $t - \Delta t$, and assuming a position-dependent potential, from which we can compute intermolecular forces $\mathbf{f}_i$. The velocities $\mathbf{v}_i$ do not appear in this scheme. In order to obtain the velocities, Eq. (3.3) can be subtracted from Eq. (3.2), giving

$$\mathbf{r}_i(t + \Delta t) - \mathbf{r}_i(t - \Delta t) = 2\mathbf{v}_i(t)\Delta t + \mathcal{O}\left(\Delta t^3\right). \tag{3.5}$$

Hence the velocities can be computed to an accuracy of order $\mathcal{O}(\Delta t^2)$:

$$\mathbf{v}_i(t) = \frac{\mathbf{r}_i(t + \Delta t) - \mathbf{r}_i(t - \Delta t)}{2\Delta t} + \mathcal{O}\left(\Delta t^2\right). \tag{3.6}$$

This completes the propagation of a point in phase space by the time step Δt. Notice that the velocities are not dynamical variables, i.e. they are sampled, but do not enter the approximated equations of motion. Therefore the "velocity" formulation of the Verlet algorithm is preferred, because it uses $(\mathbf{r}_i, \mathbf{v}_i)$ as dynamical variables rather than $(\mathbf{r}_{i-1}, \mathbf{r}_i)$.

Due to energy conservation, the microcanonical ensemble is the natural ensemble for MD simulations, just as the canonical ensemble is the natural ensemble for Monte Carlo (MC) simulatons. However, in many cases it is more convenient to simulate in other ensembles than the microcanonical ensemble, without loosing the advantage of beeing able to compute dynamical quantities, which would happen in the case of MC. Therefore a less heuristic approach than the one used in the derivation of the Verlet integrator is needed. Tuckerman et al. [10] have systematically derived time-reversible and area-preserving MD integrators from the Liouville formulation of classical mechanics. We review this method, which gives us the velocity Verlet algorithm used in our simulations.

Classical mechanics can be reexpressed in terms of the Lagrangian and Hamiltonian formulations, which are physically equivalent, but provide us with a deeper insight into the mathematical underlying structure. Furthermore these formalisms can be extended and generalized more easily, especially in the case of Hamiltonian mechanics, where the connection between classical mechanics and quantum mechanics is readily established. The Verlet integrator is a very useful and frequently used algorithm, and can easily be derived by means of an ordinary Taylor expansion, but understanding its structure more deeply, as well as the desire to simulate in other ensembles than the microcanonical one, requires a more general formalism.

Corresponding to the Hamiltonian formalism, propagation of a point in phase space means propagation of the positions and the conjugate momenta. In what

follows we will use the abreviations $\mathbf{r} = (\mathbf{r}_1, \ldots, \mathbf{r}_N)$ and $\mathbf{p} = (\mathbf{p}_1, \ldots, \mathbf{p}_N)$. The total energy of the system is expressed by the Hamiltonian function

$$H(\mathbf{r}, \mathbf{p}) = \sum_{i=1}^{N} \frac{\mathbf{p}_i^2}{2m} + U(\mathbf{r}), \tag{3.7}$$

and instead of integrating $3N$ second-order differential equations, we have to integrate $6N$ coupled first-order differential equations, Hamilton's equations of motion (1.5):

$$\dot{\mathbf{r}} = \frac{\partial H}{\partial \mathbf{p}} \tag{3.8}$$

$$\dot{\mathbf{p}} = -\frac{\partial H}{\partial \mathbf{r}}. \tag{3.9}$$

If g is an arbitrary function depending on the positions and the conjugate momenta, its time derivative is

$$\begin{aligned} \dot{g}(\mathbf{r}, \mathbf{p}) &= \sum_{i=1}^{N} \left(\dot{\mathbf{r}}_i \cdot \frac{\partial g}{\partial \mathbf{r}_i} + \dot{\mathbf{p}}_i \cdot \frac{\partial g}{\partial \mathbf{p}_i} \right) \\ &= \sum_{i=1}^{N} \left(\frac{\partial H}{\partial \mathbf{p}_i} \cdot \frac{\partial g}{\partial \mathbf{r}_i} - \frac{\partial H}{\partial \mathbf{r}_i} \cdot \frac{\partial g}{\partial \mathbf{p}_i} \right) \\ &= \{g, H\}, \end{aligned} \tag{3.10}$$

where we use the definition of the Poisson bracket as given in Eq. (1.18). Defining the Liouville operator through

$$iL \equiv \{\cdot, H\} = \sum_{i=1}^{N} \left(\dot{\mathbf{r}}_i \cdot \frac{\partial}{\partial \mathbf{r}_i} + \dot{\mathbf{p}}_i \cdot \frac{\partial}{\partial \mathbf{p}_i} \right), \tag{3.11}$$

we can write Eq. (3.10) in a condensed way:

$$\dot{g}(\mathbf{r}, \mathbf{p}) = iLg. \tag{3.12}$$

The formal solution of Eq. (3.12) is

$$\begin{aligned} g(\mathbf{r}(t), \mathbf{p}(t)) &= \exp(iLt) g(\mathbf{r}(0), \mathbf{p}(0)) \\ &= \exp(iL_r t + iL_p t) g(\mathbf{r}(0), \mathbf{p}(0)). \end{aligned} \tag{3.13}$$

Here we have separated the Liouville operator into two parts:

$$iL \equiv iL_r + iL_p, \tag{3.14}$$

with

$$\begin{aligned} iL_r &= \sum_{i=1}^{N} \dot{\mathbf{r}}_i \cdot \frac{\partial}{\partial \mathbf{r}_i}, \\ iL_p &= \sum_{i=1}^{N} \dot{\mathbf{p}}_i \cdot \frac{\partial}{\partial \mathbf{p}_i}. \end{aligned} \tag{3.15}$$

The operator $\exp(iLt)$ is known as the classical propagator. The imaginary unit i in Eq. (3.11) is a matter of convention, having on the one hand, the effect of making the classical propagator unitary, and on the other hand, establishing an analogy to the quantum mechanical propagator $\exp(-iHt/\hbar)$.

It can be shown that the operators iL_r and iL_p do not commute. For two noncommuting operators the exponential of the sum cannot be expressed by the product of two exponentials:

$$\exp(A+B) \neq \exp(A)\exp(B). \tag{3.16}$$

Returning to Eq. (3.13), which expresses a flow in a phase space, we can find a physical interpretation of this noncommutativity. Since iL_r acts only on the position-dependent part of g, and iL_p only on the momentum-dependent part, it is not possible to propagate either of the canonically conjugated variables by the time t without touching the other. This is consistent with the symplectic, i.e. intertwined structure of a Hamiltonian system: the positions and the momenta are connected to each other.

The Trotter theorem [11] can be used to overcome this difficulty:

$$\exp(A+B) = \lim_{P\to\infty} \left(e^{A/2P} e^{B/P} e^{A/2P}\right)^P. \tag{3.17}$$

Identifying A with $iL_p t$ and B with $iL_r t$, Eq. (3.13) becomes

$$g(\mathbf{r}(t),\mathbf{p}(t)) = \lim_{P\to\infty} \left(e^{iL_p t/2P} e^{iL_r t/P} e^{iL_p t/2P}\right)^P g(\mathbf{r}(0),\mathbf{p}(0)). \tag{3.18}$$

For a large but finite P, we have $e^{(iL_r t + iL_p t)} = \left(e^{iL_p t/2P} e^{iL_r t/P} e^{iL_p t/2P}\right)^P e^{\mathcal{O}(1/P^2)}$. Then $\Delta t = t/P$ can be interpreted as a time step and the integration algorithm is given by a discretized version of the phase space flow

$$g(\mathbf{r}(t),\mathbf{p}(t)) \simeq \left(e^{iL_p \Delta t/2} e^{iL_r \Delta t} e^{iL_p \Delta t/2}\right)^P g(\mathbf{r}(0),\mathbf{p}(0)), \tag{3.19}$$

where the propagation of the system by the time step Δt corresponds to applying the one-step propagator $e^{iL_p \Delta t/2} e^{iL_r \Delta t} e^{iL_p \Delta t/2}$ once.

The last step for completing the integration algorithm is to study the action of the one-step-propagator on the function $g(\mathbf{r}(t),\mathbf{p}(t))$. Due to the definitions (3.15) this is equivalent to regarding the action of the advancement operator $e^{c\frac{\partial}{\partial x}}$ on a function $\phi(x)$. Comparing with the Taylor expansion of $\phi(x+c)$ we get

$$\begin{aligned} e^{c\frac{\partial}{\partial x}}\phi(x) &= \sum_{k=0}^{\infty} \frac{1}{k!} \left(c\frac{\partial}{\partial x}\right)^k \phi(x) \\ &= \sum_{k=0}^{\infty} \frac{c^k}{k!} \frac{\partial^k \phi(x)}{\partial x^k} \\ &= \phi(x+c). \end{aligned} \tag{3.20}$$

It is easy to see, that the operator $e^{c\frac{\partial}{\partial x}}$ acts as an identity on a function independent of x. Hence the action of the operators occurring in the one-step propagator on a function depending on the coordinates and the momenta is clear, and the propagation from the time t to $t+\Delta t$ takes place in three steps.

The first step is the propagation of the momenta by half a time step:

$$\begin{aligned} e^{iL_p\Delta t/2} g(\mathbf{r}(t), \mathbf{p}(t)) &= g\left(\mathbf{r}(t), \mathbf{p}(t) + \frac{\Delta t}{2}\dot{\mathbf{p}}(t)\right) \\ &= g\left(\mathbf{r}(t), \mathbf{p}\left(t + \frac{\Delta t}{2}\right)\right). \end{aligned} \tag{3.21}$$

Application of $e^{iL_r\Delta t}$ to the result $g\left(\mathbf{r}(t), \mathbf{p}\left(t + \frac{\Delta t}{2}\right)\right)$ corresponds to the propagation of the positions by a whole time step using the intermediate velocities: $\dot{\mathbf{r}}\left(t + \frac{\Delta t}{2}\right) = \frac{1}{m}\mathbf{p}\left(t + \frac{\Delta t}{2}\right)$:

$$\begin{aligned} e^{iL_r\Delta t} g\left(\mathbf{r}(t), \mathbf{p}\left(t + \frac{\Delta t}{2}\right)\right) &= g\left(\mathbf{r}(t) + \Delta t\dot{\mathbf{r}}\left(t + \frac{\Delta t}{2}\right), \mathbf{p}\left(t + \frac{\Delta t}{2}\right)\right) \\ &= g\left(\mathbf{r}(t + \Delta t), \mathbf{p}\left(t + \frac{\Delta t}{2}\right)\right). \end{aligned} \tag{3.22}$$

Finally, in the third step, after recomputing the forces from the new positions, the propagation by Δt is completed

$$\begin{aligned} e^{iL_p\Delta t/2} g\left[\mathbf{r}(t + \Delta t), \mathbf{p}\left(t + \frac{\Delta t}{2}\right)\right] &= g\left(\mathbf{r}(t + \Delta t), \mathbf{p}\left(t + \frac{\Delta t}{2}\right) + \frac{\Delta t}{2}\dot{\mathbf{p}}(t + \Delta t)\right) \\ &= g\left(\mathbf{r}(t + \Delta t), \mathbf{p}(t + \Delta t)\right). \end{aligned} \tag{3.23}$$

Summarizing, for this particular symmetric factorization of the propagator the velocity Verlet algorithm comes out and the Liouville formalism even tells us how to implement it. First propagate the momenta by half a time step and use the propagated momenta for the propagation of the positions by a whole time step. Then use the new postions to compute the new forces $\mathbf{f}$ and finally update the momenta with the new forces, using the identity $\dot{\mathbf{p}} = \mathbf{f}$.

3.2 Molecular dynamics in different ensembles

As already mentioned, it is often more convenient to simulate at constant temperature or constant pressure or both rather than at constant energy. In this section we review how to perform MD simulations in other ensembles than the microcanonical (NVE) one. There are two different solutions which have been proposed in order to solve this problem. One solution is mixing Newtonian dynamics with certain Monte Carlo moves in order to get the averages required by the respective ensemble. The other solution uses the advantage of the general formulation of dynamics in phase space and reformulates the Lagrangian equations of motion: the coupling to a thermal or pressure reservoir can be regarded as a thermodynamic constraint, where the baths are represented by additional degrees of freedom. This so-called extended system approach was pioneered by Andersen in his seminal paper for the constant pressure (NPH) case [12]. Andersen was not able to find an adequate extension of the Lagrangian leading to a constant temperature (NVT) algorithm, which was done by Nosé [13] a few years later. This method has the advantage of being deterministic and time-reversible, which, unlike a stochastic thermostat for instance, allows to compute e.g. velocity autocorrelation functions.

Here we work out the equations for the more general constant temperature and constant pressure (NPT) algorithm, that gives us the NVT and NPH algorithms for a special choice of parameters. In deriving the equations of motion in extended phase space we shall adopt the notation used in Ref. [14].

3.2.1 Derivation of the equations of motion

Andersen achieved a constant pressure by allowing the volume of the simulation box to fluctuate in time. For this purpose he introduced virtual scaled coordinates, which are dimensionless numbers between zero and one:

$$\boldsymbol{\rho} = V^{-1/3}\mathbf{r}. \tag{3.24}$$

Similarly Nosé introduced a scaled time defined by

$$d\tau = sdt. \tag{3.25}$$

Then we also have scaled velocities given by

$$\frac{d\boldsymbol{\rho}}{d\tau} = \frac{d(\mathbf{r}V^{-1/3})}{sdt} = \frac{1}{s}V^{-1/3}\left(\frac{d\mathbf{r}}{dt} - \frac{\mathbf{r}}{3V}\frac{dV}{dt}\right), \tag{3.26}$$

and hence

$$\frac{d\mathbf{r}}{dt} = \frac{d\boldsymbol{\rho}}{d\tau}sV^{1/3} + \frac{\mathbf{r}}{3V}\frac{dV}{dt}. \tag{3.27}$$

The coupling of the system to a heat bath and a virtual pressure reservoir, keeping the system at the required state can be achieved by extending the Lagrangian by the additional reservoir variables V and s. This corresponds to introducing additional degrees of freedom, and the positions in real space are given by the quanties $\{\mathbf{r}, V, s\}$. In the space of virtual positions $\{\boldsymbol{\rho}, Q, S\}$, where Q is identified with the volume, and S with the Nosé variable s, we can write the following Lagrangian:

$$\begin{aligned}\mathcal{L} &= \frac{1}{2}mQ^{2/3}S^2\dot{\boldsymbol{\rho}}\cdot\dot{\boldsymbol{\rho}} - U(\boldsymbol{\rho}Q^{1/3}) + \frac{1}{2}S^2M_Q\dot{Q}^2 - P_{\text{ext}}Q \\ &\quad + \frac{1}{2}M_S\dot{S}^2 - gk_BT\ln S.\end{aligned} \tag{3.28}$$

Here M_Q and M_S can be interpreted as generalized masses or inertia factors associated with the two reservoirs. Then the third and the fifth term in the Lagrangian are kinetic energy terms arising from the additional degrees of freedom, whereas the fourth and the sixth are the corresponding potential energies, P_{ext} being the external pressure. From the Lagrangian, Eq. (3.28), the generalized momenta in virtual space can be computed as

$$\begin{aligned}\boldsymbol{\pi} &= \frac{\partial\mathcal{L}}{\partial\dot{\boldsymbol{\rho}}} = mS^2Q^{2/3}\dot{\boldsymbol{\rho}} \\ \Pi_Q &= \frac{\partial\mathcal{L}}{\partial\dot{Q}} = M_QS^2\dot{Q} \\ \Pi_S &= \frac{\partial\mathcal{L}}{\partial\dot{S}} = M_S\dot{S},\end{aligned} \tag{3.29}$$

and the Hamiltonian in virtual coordinates is obtained via a Legendre transformation:

$$\begin{aligned}\mathcal{H} &= \dot{\boldsymbol{\rho}}\cdot\boldsymbol{\pi} + \dot{Q}\Pi_Q + \dot{S}\Pi_S - \mathcal{L} \\ &= \frac{\boldsymbol{\pi}\cdot\boldsymbol{\pi}}{2mS^2Q^{2/3}} + U(\boldsymbol{\rho}Q^{1/3}) + \frac{\Pi_Q^2}{2M_QS^2} + P_{\text{ext}}Q \\ &\quad + \frac{\Pi_S^2}{2M_S} + gk_BT\ln S. \end{aligned} \tag{3.30}$$

The equations of motions in virtual space are Hamilton's equations for our extended system:

$$\begin{aligned}\frac{d\boldsymbol{\Pi}}{d\tau} &= -\frac{\partial\mathcal{H}}{\partial\boldsymbol{\rho}} = -Q^{1/3}\frac{\partial U(\boldsymbol{\rho}Q^{1/3})}{\partial(\boldsymbol{\rho}Q^{1/3})} = Q^{1/3}\mathbf{f} \\ \frac{d\boldsymbol{\rho}}{d\tau} &= \frac{\partial\mathcal{H}}{\partial\boldsymbol{\pi}} = \frac{\boldsymbol{\Pi}}{mS^2Q^{2/3}} \\ \frac{d\Pi_Q}{d\tau} &= -\frac{\partial\mathcal{H}}{\partial Q} = \frac{1}{3Q}\sum_{i=1}^{N}\left(\frac{\boldsymbol{\pi}_i\cdot\boldsymbol{\pi}_i}{mS^2Q^{2/3}} + Q^{1/3}\mathbf{f}_i\cdot\boldsymbol{\rho}_i\right) - P_{\text{ext}} \\ \frac{dQ}{d\tau} &= \frac{\partial\mathcal{H}}{\partial\Pi_Q} = \frac{\Pi_Q}{M_QS^2} \\ \frac{d\Pi_s}{d\tau} &= -\frac{\partial\mathcal{H}}{\partial S} = \sum_{i=1}^{N}\frac{\boldsymbol{\pi}_i\cdot\boldsymbol{\pi}_i}{mS^3Q^{2/3}} + \frac{\Pi_Q^2}{M_QS^3} - \frac{gk_{\text{B}}T}{S} \\ \frac{dS}{d\tau} &= \frac{\partial\mathcal{H}}{\partial\Pi_S} = \frac{\Pi_S}{M_S}, \end{aligned} \tag{3.31}$$

where $\mathbf{f}_i = -\partial U/\partial\mathbf{r}_i$ is the force acting on particle i.

In principle these equations of motions can be integrated numerically in virtual space, however this would produce a trajectory spaced unevenly in real space, since a constant virtual time step $\Delta\tau$ results in a non-constant Δt in real space. Therefore it is convenient to transform back into real space. The relations

$$\begin{aligned} dt &= \frac{d\tau}{s}, \\ \mathbf{r} &= \boldsymbol{\rho}Q^{1/3}, \quad V = Q, \quad s = S, \\ \mathbf{p} &= \frac{\boldsymbol{\pi}}{SQ^{1/3}}, \quad \frac{P_V}{S} = Q, \quad P_s = \Pi_S, \end{aligned} \tag{3.32}$$

provide us with a transformation from the space of virtual coordinates, momenta and times $\{\boldsymbol{\rho}, \boldsymbol{\pi}, Q, \Pi_Q, S, \Pi_S\ , \tau\}$ to the real space $\{\mathbf{r}, \mathbf{p}, V, P_V, s, P_s, t\}$. Setting

$$\begin{aligned} \eta &= \ln s, \\ P_\eta &= P_s, \end{aligned} \tag{3.33}$$

which is a convention introduced by Hoover [15], we get the following equations of

motion:

$$\begin{aligned}
\dot{\mathbf{r}} &= \frac{\mathbf{p}}{m} + \mathbf{r}\frac{1}{3V}\frac{P_V}{M_V} \\
\dot{\mathbf{p}} &= \mathbf{f} + \mathbf{p}\frac{P_\eta}{M_\eta} - \mathbf{p}\frac{1}{3V}\frac{P_V}{M_V} \\
\dot{V} &= \frac{P_V}{M_V} \\
\dot{P_V} &= F_V - P_V\frac{P_\eta}{M_\eta} \\
\dot{\eta} &= \frac{P_\eta}{M_\eta} \\
\dot{P_\eta} &= F_\eta, \qquad (3.34)
\end{aligned}$$

where we have defined the generalized force associated with the barostat

$$F_V(\mathbf{r}, \mathbf{p}, V) = \frac{1}{3V}\left(\frac{\mathbf{p}\cdot\mathbf{p}}{m} + \mathbf{r}\cdot\mathbf{f}\right) - P_{\text{ext}}, \qquad (3.35)$$

and the generalized force associated with the thermostat

$$F_\eta(\mathbf{p}, P_V) = \frac{\mathbf{p}\cdot\mathbf{p}}{m} + \frac{P_V^2}{M_V} - gk_{\text{B}}T, \qquad (3.36)$$

where $g = 3N + 1$ are the degrees of freedom. The conserved energy of the system is the extended Hamiltonian in real coordinates:

$$H = \frac{\mathbf{p}\cdot\mathbf{p}}{2m} + U(\mathbf{r}, V) + \frac{P_V^2}{2M_V} + P_{\text{ext}}V + \frac{P_\eta^2}{2M_\eta} + gk_{\text{B}}T\eta. \qquad (3.37)$$

However, since the transformation given by Eqs. (3.32) is non-canonical, the equations of motion in real space cannot be derived from Eq. (3.37).

3.2.2 Integration algorithm

The strategy for integrating the equations of motion, and herewith propagating the point $\mathbf{\Gamma} = \{\mathbf{r}, \mathbf{p}, V, P_V, \eta, P_\eta\}$ in extended phase space, follows immediately from the Liouville formalism presented in the previous section. The equations of motion can be written as $\dot{\mathbf{\Gamma}} = iL\mathbf{\Gamma}$, and a suitable Trotter factorization has to be found for the propagator e^{iLt}. Using the chain rule the Liouville-operator is written as:

$$\begin{aligned}
iL &= \frac{\mathbf{p}}{m}\cdot\frac{\partial}{\partial\mathbf{r}} + \frac{1}{3V}\frac{P_V}{M_V}\mathbf{r}\cdot\frac{\partial}{\partial\mathbf{r}} + \frac{P_V}{M_V}\frac{\partial}{\partial V} + \mathbf{f}\cdot\frac{\partial}{\partial\mathbf{p}} - \frac{P_\eta}{M_\eta}\mathbf{p}\cdot\frac{\partial}{\partial\mathbf{p}} \\
&\quad - \frac{1}{3V}\frac{P_V}{M_V}\mathbf{p}\cdot\frac{\partial}{\partial\mathbf{p}} + F_V\frac{\partial}{\partial P_V} - P_V\frac{P_\eta}{M_\eta}\frac{\partial}{\partial P_V} + \frac{P_\eta}{M_\eta}\frac{\partial}{\partial\eta} + F_\eta\frac{\partial}{\partial P_\eta} \\
&=: iL_0 + iL_1 + iL_2 + iL_3 + iL_4 + iL_5 + iL_6 + iL_7 + iL_8 + iL_9. \qquad (3.38)
\end{aligned}$$

Applying the generalization of the symmetric Trotter factorization (3.17) and defining $U_j(\Delta t) = e^{iL_j\Delta t}$ with $j = 0, \ldots, 9$, the one-step propagator $G(\Delta t)$ takes the

form,

$$\begin{aligned} G(\Delta t) &= U_9\left(\frac{\Delta t}{2}\right) U_8\left(\frac{\Delta t}{2}\right) U_7\left(\frac{\Delta t}{2}\right) U_6\left(\frac{\Delta t}{2}\right) U_5\left(\frac{\Delta t}{2}\right) U_4\left(\frac{\Delta t}{2}\right) U_3\left(\frac{\Delta t}{2}\right) \\ &\times U_2\left(\frac{\Delta t}{2}\right) U_1\left(\frac{\Delta t}{2}\right) U_0(\Delta t)\; U_1\left(\frac{\Delta t}{2}\right) U_2\left(\frac{\Delta t}{2}\right) U_3\left(\frac{\Delta t}{2}\right) U_4\left(\frac{\Delta t}{2}\right) \\ &\times U_5\left(\frac{\Delta t}{2}\right) U_6\left(\frac{\Delta t}{2}\right) U_7\left(\frac{\Delta t}{2}\right) U_8\left(\frac{\Delta t}{2}\right) U_9\left(\frac{\Delta t}{2}\right). \end{aligned} \tag{3.39}$$

Translating the action of the single operators U_j on the phase space vector $\mathbf{\Gamma}$ analogously to the case of the velocity Verlet algorithm in the previous section, the following integration algorithm is obtained [14]:

$$\begin{aligned} P_\eta(\Delta t/2) &= P_\eta(0) + \frac{\Delta t}{2} F_\eta(0) \\ \eta(\Delta t/2) &= \eta(0) + \frac{\Delta t}{2M_\eta} P_\eta(\Delta t/2) \\ P_V(\Delta t/2) &= P_V(0) + \exp\left[-\frac{\Delta t}{2M_\eta} P_\eta(\Delta t/2)\right] + \frac{\Delta t}{2} F_V(0) \\ \mathbf{p}(\Delta t/2) &= \mathbf{p}(0) \exp\left[-\frac{\Delta t}{2M_V}\frac{p_V(\Delta t/2)}{3V(0)} - \frac{\Delta t}{2M_\eta} P_\eta(\Delta t/2)\right] + \frac{\Delta t}{2}\mathbf{f}(0) \\ V(\Delta t/2) &= V(0) + \frac{\Delta t}{2M_V} P_V(\Delta t/2) \\ \mathbf{r}(\Delta t) &= \left\{\mathbf{r}(0) \exp\left[\frac{\Delta t}{2M_V}\frac{P_V(\Delta t/2)}{3V(\Delta t/2)} + \frac{\Delta t}{m}\mathbf{p}(\Delta t/2)\right]\right\} \exp\left[\frac{\Delta t}{2M_V}\frac{P_V(\Delta t/2)}{3V(\Delta t/2)}\right] \\ V(\Delta t) &= V(\Delta t/2) + \frac{\Delta t}{2M_V} P_V(\Delta t/2) \\ \mathbf{p}(\Delta t) &= \left[\mathbf{p}(\Delta t/2) + \frac{\Delta t}{2}\mathbf{f}(\Delta t)\right] \exp\left[-\frac{\Delta t}{2M_\eta} P_\eta(\Delta t/2) - \frac{\Delta t}{2M_V}\frac{P_V(\Delta t/2)}{3V(\Delta t)}\right] \\ P_V(\Delta t) &= \left[P_V(\Delta t/2) + \frac{\Delta t}{2} F_V(\Delta t)\right] \exp\left[-\frac{\Delta t}{2M_\eta} P_\eta(\Delta t/2)\right] \\ \eta(\Delta t) &= \eta(\Delta t/2) + \frac{\Delta t}{2M_\eta} P_\eta(\Delta t/2) \\ P_\eta(\Delta t) &= P_\eta(\Delta t/2) + \frac{\Delta t}{2} F_\eta(\Delta t). \end{aligned} \tag{3.40}$$

This can easily be translated into a piece of computer code. In C++ the code can be written elegantly using the operator + =, and e.g. the first line of the algorithm is implemented by the line

```
peta += feta*deltat/2.
```

Chapter 4

Boltzmann's H-theorem

4.1 Foreword

A fundamental question in statistical mechanics is the reconciliation of the irreversibility of thermodynamics with the reversibility of the microscopic equations of motion governed by classical mechanics. In 1872 Ludwig Boltzmann gave an answer with his H-theorem [16], describing the increase in the entropy of an ideal gas as an irreversible process. However, the proof of this theorem contained the *Stoßzahlansatz*, i.e. the assumption of molecular chaos. The result was subject to two main objections: Loschmidt's *Umkehreinwand* (reversibility paradox) [17, 18] and Zermelo's *Wiederkehreinwand* (recurrence paradox) [19]. Boltzmann's reply to the two objections was not fully understood at the time, but is now considered as a corner stone of statistical mechanics. It is summarized in the article that Paul and Tatiana Ehrenfest wrote for the German *Encyclopedia of Mathematical Sciences* [3]. Subsequently, Boltzmann's approach has been reformulated in the language of stochastic processes [20, 21, 1].

Essentially, even in the presence of a deterministic microscopic dynamics, the *coarse graining* of configuration space due to the observer's state of knowledge results in a stochastic process, where the number of particles in a given cell varies at random as a function of time.

4.2 Definition of H

In the following two sections the definition of Boltzmann's H and the derivation of the H-theorem will be reviewed. We shall thereby follow the route of Tolman in his classical textbook [22].

In statistical mechanics one is not interested in finding the precise states of molecules in μ-space, but rather small intervals where the generalized coordinates and momenta could lie. This procedure is called *coarse graining* since the μ-space is divided into equal cells and the particles situated in the same cells are considered to have identical states.

Boltzmann's H is defined as

$$H = \int_{\mu} f(\mathbf{x}) \log f(\mathbf{x})\, dv_{\mu}, \tag{4.1}$$

where the integration goes over μ-space and $dv_\mu = dq_1 \dots dq_r dp_1 \dots dp_r$ is the volume element in μ-space. A vector in μ-space is defined by $\mathbf{x} = (q_1, \dots, q_r, p_1, \dots, p_r)$. The number dn of molecules lying in any volume element of μ-space is proportional to the volume:

$$dn = f(\mathbf{x}, t) dv_\mu. \tag{4.2}$$

At equilibrium the density $f(\mathbf{x})$ should be of the time-independent form $nCe^{-\epsilon((x))/k_\mathrm{b}BT}$ and hence Eq. (4.2) would reduce to the Maxwell-Boltzmann law

$$dn = nCe^{-\frac{\epsilon(\mathbf{x})}{k_B T}} dv_\mu, \tag{4.3}$$

where ϵ is the energy that depends on the generalized coordinates and momenta $\mathbf{x}$. It has been tacitly assumed that the number of molecules is big enough to be treated as a continuous function of the position in μ-space.

The transition from a continuous to a discrete version of H is made by coarse graining, i.e. dividing the μ-space into small non-infinitesimal cells labeled by integers $i = 1, 2, \dots, d$. Defining $f_i(t)$ as $f(\mathbf{x}, t)$ for all $\mathbf{x}$ contained in cell i, the occupation number of the latter is

$$n_i = f_i(t) \Delta v_\mu, \tag{4.4}$$

where $\Delta v_\mu = \Delta q_1 \cdots \Delta q_r \Delta p_1 \cdots \Delta p_r$ is the finite volume of a cell in μ-space. Then the discrete version of Eq. (4.1) becomes

$$H = \sum_{i=1}^{d} f_i \log f_i \Delta v_\mu. \tag{4.5}$$

Inserting Eq. (4.4) into Eq. (4.5) the discrete form of H can be given as a function of the number of particles n_i lying in cell i of the μ-space:

$$\begin{aligned} H &= \sum_{i=1}^{d} n_i \log\left(\frac{n_i}{\Delta v_\mu}\right) \\ &= \sum_{i=1}^{d} [n_i \log n_i - n_i \log \Delta v_\mu] \\ &= \sum_{i=1}^{d} n_i \log n_i - N \log \Delta v_\mu. \end{aligned} \tag{4.6}$$

4.3 Derivation of Boltzmann's H-theorem

Starting from its continuous form given by Eq. (4.1) the time derivative of H reads:

$$\frac{dH}{dt} = \int_\mu \left(\frac{df(\mathbf{x})}{dt} \log f\mathbf{x} + \frac{df(\mathbf{x})}{dt} \right) dv_\mu. \tag{4.7}$$

The second term in Eq. (4.7) is zero because exchanging the order of integration and differentiation it is the time-derivative of the total number of particles N, which is assumed to be constant. Hence we have

$$\frac{dH}{dt} = \int_\mu \frac{df(\mathbf{x})}{dt} \log f(\mathbf{x}) dv_\mu. \tag{4.8}$$

In order to prove the H-theorem it should be shown from Eq. (4.8) that for all possible molecular processes H can only decrease. In what follows we shall sketch the proof that, considering bimolecular collisions as a mechanism of changes in H, the latter can only decrease. This is a situation which could model a dilute gas, that is assumed to be spatially homogeneous, which means that the density function $f(\mathbf{x}, t)$ does not depend on the positions of the particles' centers of masses. If the vector in μ-space is $\mathbf{x} = (x, y, z, q_4, \ldots, q_r, p_1, \ldots, p_r) =: (x, y, z, \boldsymbol{\omega})$, this can be formulated as

$$dn = f(\boldsymbol{\omega}, t) dx dy dz d\omega, \tag{4.9}$$

with $d\omega = dq_4 \cdots dq_r dp_1 \cdots dp_r$. Here the molecular state of interest is represented by the vector $\boldsymbol{\omega}$. Inserting Eq. (4.9) into Eq. (4.8) one obtains:

$$\begin{aligned} \frac{dH}{dt} &= \int_\mu \frac{df(\boldsymbol{\omega}, t)}{dt} \log f(\boldsymbol{\omega}, t)\, dx dy dz d\omega \\ &= V \int_\Omega \frac{df(\boldsymbol{\omega}, t)}{dt} \log f(\boldsymbol{\omega}, t)\, d\omega. \end{aligned} \tag{4.10}$$

Here V is the volume of the system and $\boldsymbol{\omega} \in \Omega$ determines the range of integration.

In order to evaluate the change of H due to collisions, some notation corresponding to Ref. [22] is introduced. In the same spirit as Boltzmann, Tolman uses the following symbol to explain the effect of a bimolecular collision:

$$\begin{pmatrix} j, & i \\ k, & l \end{pmatrix}. \tag{4.11}$$

According to the concept of coarse graining, this means that two molecules originally located in cells of μ-space labeled i and j, change states due to the collision and are finally found in cells k and l respectively. Because of the assumption of spatial homogeneity used in Eq. (4.9), the molecular states of interest are determined by $\boldsymbol{\omega}$, and hence a particle is found in the state i if the corresponding vector $\boldsymbol{\omega}$ lies in the cell i with the volume $d\omega_i$. Then, corresponding to Eq. (4.4) the number of particles in the state i is

$$dn_i = V f_i d\omega_i, \tag{4.12}$$

where the factor V is obtained via integration over all the positions. The convention in Eq. (4.11) is that the first molecule undergoes the transiton $i \to k$ and the second the transition $j \to l$. This supports the physical intuition of two approaching particles which collide and afterwards move away from each other. The *corresponding collision* to the collision given by the symbol (4.11) is defined by

$$\begin{pmatrix} l, & k \\ x, & y \end{pmatrix}. \tag{4.13}$$

This is the collision starting from the initial constellation (l, k) and ending in an arbitrary final constellation (x, y). The constellation (l, k) is called the *corresponding constellation* to the final constellation (k, l) from (4.11), where the positions of the particles have been exchanged in order to ensure the occurence of a collision. The collision

$$\begin{pmatrix} l, & k \\ i, & j \end{pmatrix} \tag{4.14}$$

is called the *inverse collision* to (4.11) and describes the transition from the corresponding constellation (l,k) to the final constellation (k,l) into (i,j), which is the corresponding constellation to the initial constellation (j,i). It can be proven [22] that every collision has an inverse collision if the system of interest is composed of spherical particles. For non-spherical particles this is not true, but it is possible to construct a closed cycle of corresponding collisions,

$$\begin{pmatrix} j, & i \\ k, & l \end{pmatrix} \begin{pmatrix} l, & k \\ m, & n \end{pmatrix} \dots \begin{pmatrix} x, & y \\ i, & j \end{pmatrix}, \tag{4.15}$$

where the initial molecular state is reached again. This is the basis of the proof, that H can only decrease due to collisions, no matter how complex the particles may be. The proof will only be reviewed for spherical particles since the same principle is employed for the non-spherical case.

The most probable number of collisions of the form given by Eq. (4.11) is proportional to the number of particles in the states i and j, and can thus be written as

$$Z_{\substack{j,\ i \\ k,\ l}} = C f_i f_j, \tag{4.16}$$

with a positive constant C. The latter can be evaluated using the Liouville theorem and probabilistic methods [22], assuming that we are dealing with a dilute gas with uniform density, which means that the probability P of finding the center of mass of a specified particle inside a specified volume dV is given by $P = dV/V$. It is important to note that the number of collisions following the required pattern depends only on the number of particles in the states i and j, but not on all the other molecules, a statement which is called the *Stoßzahlansatz*, or the assumption of molecular chaos.

The number of collisions of the pattern given by Eq. (4.11) is also equal to the rates of change of the occupation numbers n_m, with $m \in I$, and the index set $I = \{i,j,k,l\}$. The rate of change will be negative for i and j, since the states are left after the collision, and positive for k and l. Using Eqs. (4.12) and (4.16) we can summarize this in an equation:

$$\begin{aligned} C f_i f_j = -\frac{dn_i}{dt} &= -V\frac{df_i}{dt}d\omega_i && (4.17)\\ = -\frac{dn_j}{dt} &= -V\frac{df_j}{dt}d\omega_j && (4.18)\\ = \quad\frac{dn_k}{dt} &= \quad V\frac{df_k}{dt}d\omega_k && (4.19)\\ = \quad\frac{dn_l}{dt} &= \quad V\frac{df_l}{dt}d\omega_l. && (4.20) \end{aligned}$$

Discretizing Eq. (4.10) the rate of change in H due to the collision given by Eq. (4.11) reads:

$$\left(\frac{dH}{dt}\right)_{\substack{l,\ k \\ i,\ j}} = \sum_{m\in I} \frac{df_m}{dt} \log f_m d\omega_m, \tag{4.21}$$

and, employing Eq. (4.17), we get after some simple algebraic manipulations:

$$\left(\frac{dH}{dt}\right)_{\substack{j,\ i \\ k,\ l}} = C f_i f_j \log\left(\frac{f_k f_l}{f_i f_j}\right). \tag{4.22}$$

It is easy to see that the right side of Eq. (4.22) can be either positive or negative, however, as it has been mentioned before, for every collision the inverse collision exists, and its effect on the change of H is

$$\left(\frac{dH}{dt}\right)_{\substack{l,\ k\\ i,\ j}} = C f_k f_l \log\left(\frac{f_i f_j}{f_k f_l}\right), \tag{4.23}$$

where C is the same constant as in Eq. (4.16), which is a consequence of the *Stoßzahlansatz*. Combining Eqs. (4.22) and (4.23), the rate of change due to the pair of mutually inverse collisions (4.11) and (4.14) takes the form

$$\frac{dH}{dt} = C(f_i f_j - f_k f_l) \log\left(\frac{f_k f_l}{f_i f_j}\right), \tag{4.24}$$

which is always negative, since the products $f_i f_j$ and $f_k f_l$ are always positive. The existence of the inverse collision guarantees that on average H will always decrease. If $f_i f_j = f_k f_l$ holds, equilibrium is reached and $dH/dt = 0$.

For the case of non-spherical particles the discussion is similar, although the treatment is more difficult since a closed cycle of collisions of the shape given by Eq. (4.15) has to be considered instead of a pair of inverse collisions.

4.4 Statistical equilibrium

The statement about the behaviour of H is of statistical nature. Far away from equilibrium the probability that H decreases is high, and as the system approaches equilibrium the fluctuations about the minimum will be small. The requirement that equilibrium is reached when H is at its minimum also gives us the distribution of the numbers n_i in terms of a variational problem with constraints. Starting from Eq. (4.6), which has the shape

$$H = \sum_{i=1}^{d} n_i \log n_i + c, \tag{4.25}$$

where c is aconstant, the minimum condition of H reads

$$\delta H = \sum_{i=1}^{d} (\log n_i + 1)\delta n_i = 0. \tag{4.26}$$

As we are dealing with an isolated system, the subsidiary conditions arise in terms of particle and energy conservation,

$$\begin{aligned} \delta n &= \sum_{i=1}^{d} \delta n_i = 0, \\ \delta E &= \sum_{i=1}^{d} \epsilon_i \delta n_i = 0 \end{aligned} \tag{4.27}$$

and hence

$$\sum_{i=1}^{d} (\log n_i + \alpha + \beta\epsilon_i)\, \delta n_i = 0, \tag{4.28}$$

where α and β are Lagrange multipliers. Then the equilibrium distribution is

$$n_i = e^{-\alpha-\beta\epsilon_i}, \tag{4.29}$$

thus recovering the Maxwell-Boltzmann law, Eq. (4.3).

Chapter 5

Ehrenfest urn revisited

5.1 The model

Almost exactly 100 years ago [23], the Ehrenfests gave a simple and convincing interpretation of Boltzmann's ideas in term of an urn stochastic process that is a periodic Markov chain in their original formulation [3, 24, 25]. There are N marbles or balls to be divided into two equal parts of a box. In order to fix the ideas, let us call P the number of balls in the left part and Q the number of balls in the right part. The balls are labeled from 1 to N. At each step of the process, an integer between 1 and N is selected with probability $1/N$ and the corresponding ball is moved from one part to the other. Rather than urns and balls, later variants of the model used dogs and fleas jumping from one dog to the other, but this does not change the mathematics. Indeed, according to Ref. [25], the Ehrenfests already had something similar to fleas in mind because they used the verb *hüpfen*, meaning *hop*, that is more appropiate for fleas than for marbles. Assuming $P > Q$, in terms of the random variable $\Delta z = |P - Q|$, the unconditional equilibrium probability of a certain value of Δz is given by

$$p_{\mathrm{eq}}(\Delta z) = \binom{N}{P}\left(\frac{1}{2}\right)^N = \binom{N}{(N+\Delta z)/2}\left(\frac{1}{2}\right)^N. \tag{5.1}$$

In the limit for $N \to \infty$ [20]

$$p_{\mathrm{eq}}(\Delta z) \sim \sqrt{\frac{2}{N\pi}}\exp\left[-\frac{(\Delta z)^2}{2N}\right]. \tag{5.2}$$

The transition probabilities of a decrease, $p_{\mathrm{d}}(\Delta z - 2 \,|\, \Delta z)$, and of an increase, $p_{\mathrm{u}}(\Delta z + 2 \,|\, \Delta z)$, of Δz are given by

$$p_{\mathrm{d}}(\Delta z - 2 \,|\, \Delta z) = \frac{P}{N} = \frac{N + \Delta z}{2N} \tag{5.3a}$$

$$p_{\mathrm{u}}(\Delta z + 2 \,|\, \Delta z) = \frac{Q}{N} = \frac{N - \Delta z}{2N}. \tag{5.3b}$$

Eqs. (5.3) completely determine the Ehrenfest urn Markov chain. It is possible to define an aperiodic version of this process, but both versions share the same stationary distribution (invariant measure) given by Eq. (5.1), that in the aperiodic case is also the equilibrium distribution [24, 26]. As noticed by Kohlrausch and

Schrödinger [27, 28], Eq. (5.1) can be regarded as the equilibrium distribution for a fictitious walker obeying a suitable forward Kolmogorov equation:

$$p(P, t+1) = \frac{P+1}{N} p(P+1, t) + \frac{N-P+1}{N} p(P-1, t). \tag{5.4}$$

By means of this stochastic process, the Ehrenfests were able to present convincing evidence in favour of Boltzmann's approach. In this example, the random variable Δz is the analogous of H and it almost always decreases from any higher value; moreover this is true both in the direct and reverse time direction as required by Loschmidt's *Umkehreinwand*, and Δz is quasiperiodic as required by Zermelo's *Wiederkehreinwand* [3].

But what happens if this game is played with a real fluid or, more modestly, with a realistic model [8, 9] of a fluid? As argued by Boltzmann, in this case the deterministic microscopic dynamics induces a stochastic process and, again, the number of fluid particles in the left side of the box P and in the right side of the box Q fluctuate as a function of time. Here, the coarse graining is simply due to the division into two equal parts of the box that contains the fluid. Hence the analogy to Boltzmann's H arises if we use Eq. (4.6). Neglecting the constant term we have:

$$\begin{aligned} H &= \sum_{i=1}^{2} n_i \log n_i \\ &= P \log P + Q \log Q \\ &= \frac{N}{2} \log \left(N^2 - (\Delta z)^2\right) + \frac{\Delta z}{2} \log \left[\frac{N + \Delta z}{N - \Delta z}\right] - N \log 2, \end{aligned} \tag{5.5}$$

which is a monotonically increasing function of Δz. The behaviour of the processes Δz and H is compared in Fig. (5.1).

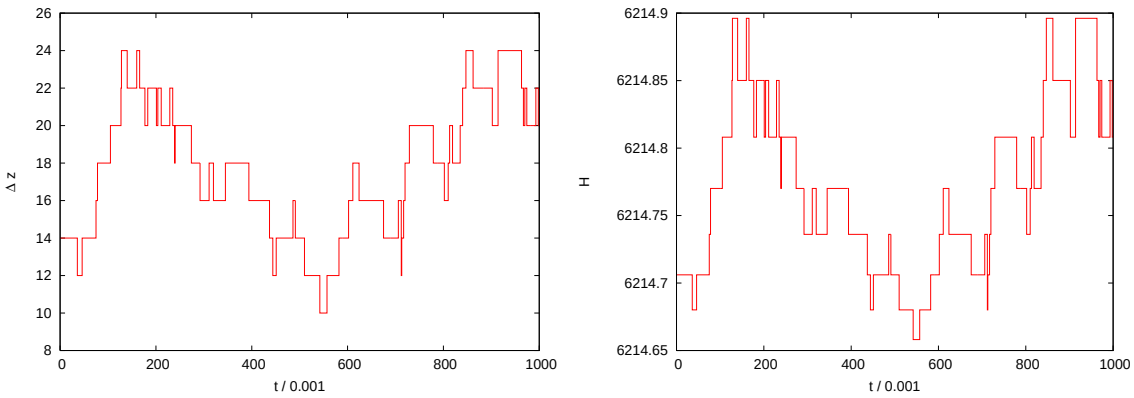

Figure 5.1: The pure-jump stochastic processes $\Delta z = |P - Q|$ (left) and H (right) as a function of the first 1000 time steps of the first simulation run in Table 5.1.

The Markov hypothesis, clearly explained by Penrose [1], is instrumental in deriving the properties of statistical equilibrium. There is, however, a further complication. P, Q, and Δz can be constant for a certain time before changing their values. The waiting times between these jumps are randomly distributed as well. The mathematical model for such a process is called a *continous-time pure-jump stochastic process* [24]. A pure-jump process is Markovian if and only if the waiting time

between two consecutive jumps is exponentially distributed (this distribution may depend on the initial non-absorbing state) [24]. The following remark is important. It is possible to define a pure-jump process by coupling a Markov chain, such as the Ehrenfest urn process defined above, with a point process for the inter-jump waiting times. If the latter is non exponential, the pure-jump process is non-Markovian.

In the present work, we investigate the Markovian character of the pure-jump process induced by the simulation of a Lennard-Jones fluid in a box.

5.2 Methodology

Systems with $N = 500,\ 1000,\ 2000$ and $100\,000$ atoms interacting with the cut and shifted Lennard-Jones pair potential

$$\begin{aligned} U &= \sum_{i<j} \left[U_{ij}(r_{ij}) - U_{ij}(r_{\text{cut}})\right], \\ U_{ij}(r_{ij}) &= 4\epsilon \left[\left(\frac{\sigma}{r_{ij}}\right)^{12} - \left(\frac{\sigma}{r_{ij}}\right)^{6}\right], \end{aligned} \tag{5.6}$$

where r_{ij} is the interatomic distance, were simulated using classical molecular dynamics [29, 30]. We employed a parallelepiped unit box with side ratios 1:1:1 when $N = 1000$ or 2:1:1 in the other cases, and periodic boundary conditions in all three directions of space. For $N = 1000$, we used also two parallel soft walls in the x-direction with periodic boundary conditions in the y, z-directions only, i.e. "slab" boundary conditions. The wall potential was given by integrating the Lennard-Jones potential over a semi-infinite wall of atoms distributed with a density ρ_{w} [31]:

$$\begin{aligned} U_{\text{w}} &= \sum_{i} \left[U_{i\text{w}}(r_{i\text{w}}) - U_{i\text{w}}(r_{\text{cut}}^{\text{w}})\right], \\ U_{i\text{w}}(r_{i\text{w}}) &= 4\pi\rho_{\text{w}}\sigma^3\epsilon \left[\frac{1}{45}\left(\frac{\sigma}{r_{i\text{w}}}\right)^{9} - \frac{1}{6}\left(\frac{\sigma}{r_{i\text{w}}}\right)^{3}\right], \end{aligned} \tag{5.7}$$

where $r_{i\text{w}}$ is the atom-wall distance. We did not put walls along all three directions of space to avoid too large surface effects with small values of N. We use reduced units with $\sigma = \epsilon = m = k_{\text{B}} = 1$, where m is the mass of each atom and k_{B} is the Boltzmann constant. This defines the time unit as $\sigma\sqrt{m/\epsilon}$ and the temperature unit as ϵ/k_{B}. We used the common bulk cutoff value $r_{\text{cut}} = 2.7$ and a wall cutoff $r_{\text{cut}}^{\text{w}} = \sqrt[6]{2/5}$ corresponding to the minimum of the wall potential, so that the cut and shifted wall potential is purely repulsive. ρ_{w} was set to 1, i.e. slightly below the densities of bcc (1.06) and fcc (1.09) lattices. We chose four points in the phase diagram with $(\rho,\, T) = (0.05, 1.2),\ (0.7, 1.2),\ (0.05, 1.6),\ (0.7, 1.6)$ lying around the critical point, whose accepted value for the Lennard-Jones fluid is (0.35,1.35) [32, 33]; see Fig. 5.2.

Production runs of 10 million time steps were done in the microcanonic ensemble with the velocity Verlet integrator [10, 34], while equilibration runs were performed in the canonic ensemble with an extended system thermostat [10, 13, 14, 15]. At every time-step we measured P as the number of atoms on the left part of the box, that is with $r_x < 0$. Thus, as mentioned before, one has $\Delta z = |P - Q| = |2P - N|$; see Fig. 5.1. While a time-step $\Delta t = 0.025$ is sufficient for an acceptable energy

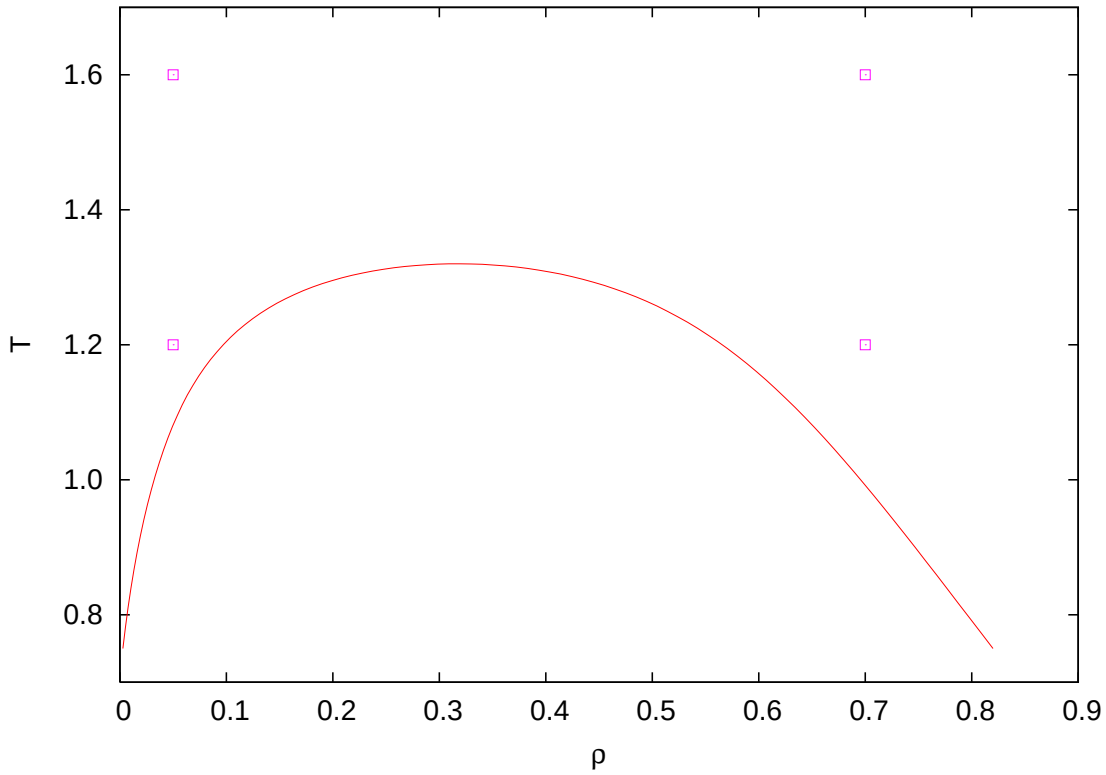

Figure 5.2: The four simulated points (squares) in the phase diagram of the Lennard-Jones fluid. The liquid-vapour curve (solid line) is a Bezier fit to data from Ref. [33]. The critical point corresponds to the maximum of the liquid-vapour curve.

conservation in this kind of system [14], to get a good resolution of the waiting times we started employing a smaller $\Delta t = 0.001$; for $N = 1000$, we obtained $\sigma_E/|\langle E\rangle|$ in the range from $7.0 \cdot 10^{-6}$ to $1.1 \cdot 10^{-4}$ depending on ρ and T. Nevertheless, any time-step we tried down to 0.0001 was still large enough to observe a few percent of jumps in Δz greater than 2; the shorter the average waiting time, the higher the percentage. There were even occasional variations greater than 4 or, for some parameter combinations, 6, 8 or 10.

A trajectory of 10 million time-steps with $N = 1000$ took about 20 hours at $\rho = 0.05$ and about 80 hours at $\rho = 0.7$ on a 2.4 GHz Intel Pentium IV processor with our own C++ code using Verlet neighbour lists. With $N = 100\,000$, the lower density lasted 17.5 hours on 64 IBM Power4+ processors at 1.7 GHz, and the higher density almost 9 days on 64 AMD Opteron 270 processors at 2.0 GHz, with a Fortran code using domain decomposition and linked cell lists [35]. Trajectories of this length are the main difference with respect to the pioneering simulations of 40 years ago, when for $N = 864$ atoms and $\rho \simeq 0.8$ one time-step took 45 seconds on a CDC-3600 [8], while trajectories consisted typically of 1200 time-steps [9].

5.3 Results

5.3.1 Analysis of jumps

In this section, we study the random variable Δz. We compare simulation results with the Ehrenfest theory to see whether Δz obeys the Markov-chain equations (5.1–5.4).

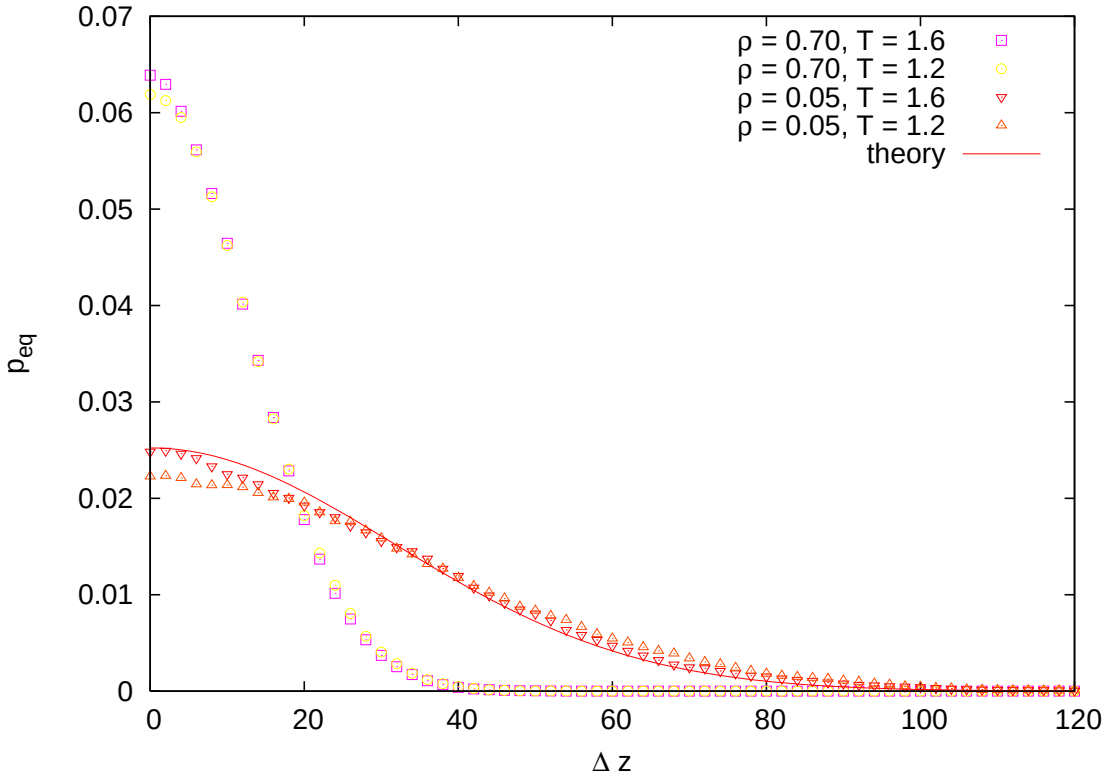

Figure 5.3: Histograms of the values of Δz from the runs of the $N = 1000$ systems without walls. The theoretical line given by Eq. (5.2) matches the gas states.

In Fig. 5.3, the empirical estimate for $p_{\rm eq}(\Delta z)$ is plotted and compared with Eq. (5.2). There is visibly a good agreement between the quantitative prediction of Eq. (5.2) and the empirical histogram for the gas phase, and this agreement is slightly better for the higher temperature.

In Fig. 5.4, we report results on the one-step transition probabilities. The Ehrenfest prediction is given by Eqs. (5.3). Again, in the gas phase of the Lennard-Jones fluid there is agreement between the sampled transition probabilities and the Ehrenfest theory. Even if linear in Δz, the sampled transition probabilities for the liquid phase deviate from Eqs. (5.3).

Sampled two-steps transition probabilites are plotted in Fig. 5.5. If the process is a Markov chain, these probabilities must be the product of two one-step transition probabilities. This property appears satisfied both for the gas and for the liquid. Moreover, for the gas, the sampled two-steps probabilities follow the Ehrenfest quantitative prediction given by Eqs. (5.3).

Even if, rigorously speaking, we have not shown that, for all n, the n-step transition probabilities are the product of n one-step transition probabilities (see Ref. [36] for processes obeying the semigroup property that are not Markov chains), at

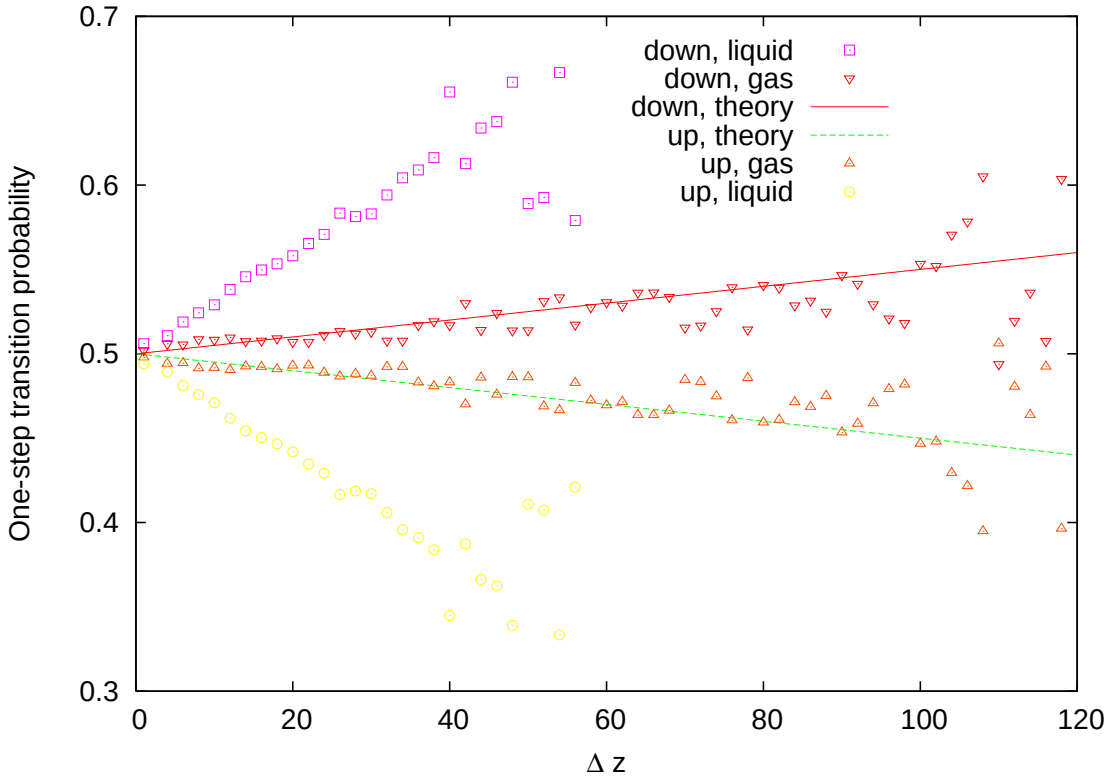

Figure 5.4: One-step transition probabilities $p_{\mathrm{d}}(\Delta z - 2 \,|\, \Delta z)$ and $p_{\mathrm{u}}(\Delta z + 2 \,|\, \Delta z)$ for $\rho = 0.7,\ T = 1.2$ (liquid) and $\rho = 0.05, T = 1.6$ (gas), $N = 1000$ without walls. The theoretical lines $1/2 \pm \Delta z/(2N)$ [20] match the gas state.

least we can claim that we have not been able to falsify the Markov-chain hypothesis for Δz based on our statistics in all the investigated cases. Remarkably, the pure Ehrenfest Markov-chain theory is a good approximation for the gas, but does not work quantitatively for the liquid.

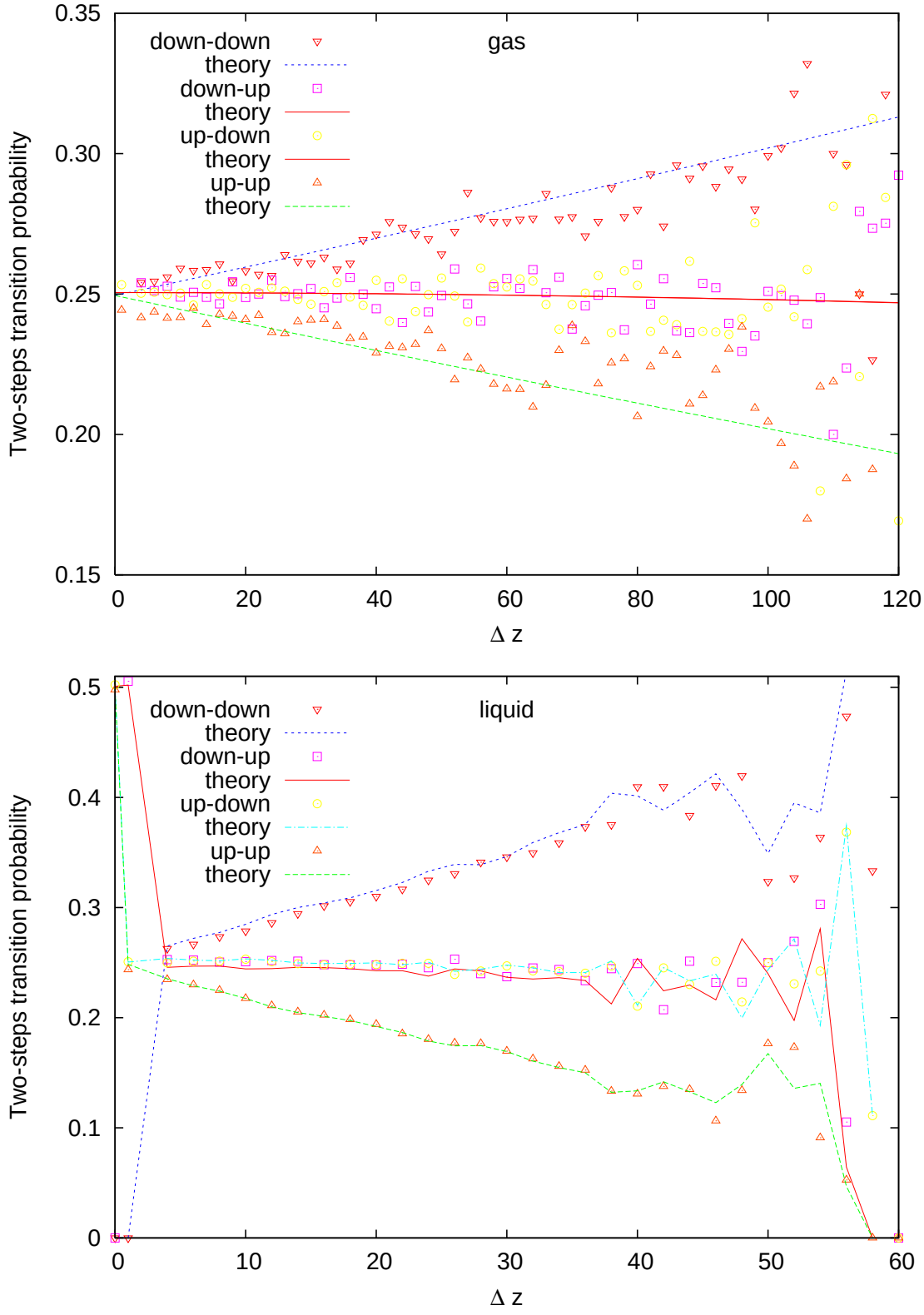

Figure 5.5: Two-steps transition probabilities $p_{\mathrm{dd}}(\Delta z - 4 \,|\, \Delta z)$, $p_{\mathrm{du}}(\Delta z \,|\, \Delta z)$, $p_{\mathrm{ud}}(\Delta z \,|\, \Delta z)$ and $p_{\mathrm{uu}}(\Delta z + 4 \,|\, \Delta z)$ for $\rho = 0.05$, $T = 1.6$ (gas, top) and $\rho = 0.7$, $T = 1.2$ (liquid, bottom), $N = 1000$ without walls. The theoretical lines are the product of the two corresponding one-step transition probabilities, e.g. $p_{\mathrm{uu}}(\Delta z + 4 \,|\, \Delta z) = p_{\mathrm{u}}(\Delta z + 4 \,|\, \Delta z + 2) p_{\mathrm{u}}(\Delta z + 2 \,|\, \Delta z)$. We use the theoretical one-step transition probabilities for the gas and the observed ones for the liquid.

5.3.2 Analysis of waiting times

The results of the simulations regarding the waiting time distribution are summarized in Table 5.1.

Δt	N	ρ	T	n	A^2	$\langle\tau\rangle$	σ_τ
1.0	1000	.05	1.2	613 751	2061	16.29	15.79
1.0	w 1000	.05	1.2	618 220	2096	16.18	15.69
1.0	1000	.05	1.6	704 881	3038	14.19	13.67
1.0	w 1000	.05	1.6	704 007	3031	14.20	13.68
1.0	1000	.70	1.2	1 386 970	18 666	7.210	6.662
1.0	w 1000	.70	1.2	1 407 654	19 428	7.104	6.562
1.0	1000	.70	1.6	1 578 866	26 525	6.334	5.779
1.0	w 1000	.70	1.6	1 565 301	25 835	6.389	5.841
1.0	500	.70	1.6	675 876	2847	14.80	14.14
1.0	2000	.70	1.6	1 561 554	25 704	6.404	5.856
0.2	2000	.05	1.2	127 237	29.84	15.72	15.59
0.1	2000	.05	1.2	64 617	3.78	15.48	15.46
.01	2000	.05	1.2	6 306	0.686	15.85	16.15
1.0	100 000	.05	1.2	4 988 531	587 570	2.005	1.419
0.1	100 000	.05	1.2	820 837	4534	1.218	1.166
0.1	100 000	.70	1.6	2 043 142	52 278	.4894	.4369

Table 5.1: For each integration time-step Δt, number of atoms N, density ρ and temperature T (a "w" before the N value indicates a system with walls in the x-direction), this table gives the number of observed waiting times n, the values of the Anderson-Darling statistics A^2 [37], the average waiting time $\langle\tau\rangle$, and the standard deviation of waiting times σ_τ. Reduced units as defined in Sec. 5.2 are used throughout, with times divided by 0.001. The standard error on $\langle\tau\rangle$ is around 0.02 for $\rho = 0.05$ and 0.006 for $\rho = 0.70$. The standard error on σ_τ is around 0.02 for $\rho = 0.05$ and 0.005 for $\rho = 0.70$. Only significant digits are given in the table. The last digit of $\langle\tau\rangle$ and σ_τ is of the same order of magnitude as $\sigma_\tau/\sqrt{n}$. See text for further explanations.

The Anderson-Darling statistics A^2 reported in the sixth column results from [37]

$$A^2 = \left\{ -\sum_{i=1}^{n} \frac{(2i-1)}{n} [\ln \Psi(\tau_{n+1-i}) + \ln(1 - \Psi(\tau_i))] - n \right\} \left(1 + \frac{0.6}{n}\right), \qquad (5.8)$$

where $\Psi(\tau)$ denotes the survival function, a short name for the complementary cumulative distribution function, i.e. the probability that waiting times are larger than τ. In Eq. (5.8) the waiting times are sorted: $\tau_1 \leq \tau_2 \leq \ldots \leq \tau_n$. The limiting value at 1% significance for accepting the null hypothesis of exponentially distributed waiting times is 1.957. Therefore, the null hypothesis can be rejected in all cases with $\Delta t \geq 0.0001$. The average waiting time $\langle\tau\rangle$ and the standard deviation σ_τ of the observed distribution, reported in columns seven and eight, must coincide for an exponential distribution. Even if their values are close, with the given statistics

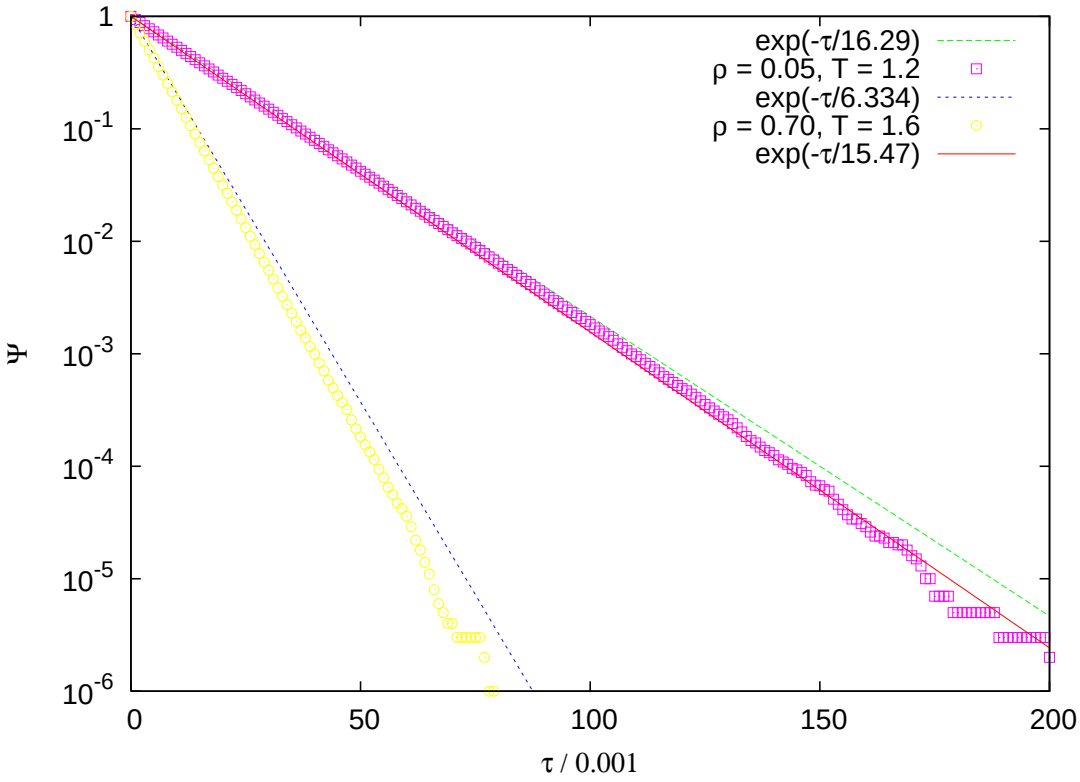

Figure 5.6: $N = 1000$, no walls. Comparison between the observed survival functions and the theoretical exponential survival functions (dashed lines) with the corresponding average waiting time $\langle\tau\rangle$, for the closest case (squares) and the most distant case (circles). The theoretical exponential survival function of the system with $N = 2000$ and $\Delta t = 10^{-5}$ is shown for reference (continuous line).

they cannot be considered equal. Fig. 5.6 further illustrates this point; there, the *closest* case to an exponential for $N = 1000$ is presented, $\rho = 0.05$, $T = 1.2$ without walls, as well as the *most distant* case, $\rho = 0.7$, $T = 1.6$ without walls. In both cases the points are the observed survival function, $\Psi(\tau)$, and the dashed line is the exponential fit. A deviation from the exponential distribution is evident at first sight. It is important to remark that this is a one-parameter fit, since the average waiting time $\langle\tau\rangle$ is sufficient to fully determine the exponential distribution, with survival function $\Psi_{\text{exp}}(\tau) = \exp(-\tau/\langle\tau\rangle)$, corresponding to a given data set. In other words, the mere fact that in log-linear scale the survival function is approximately a straight line is not sufficient to conclude that the observed distribution is exponential. In the four cases studied here, the presence of walls does not significantly affect the results.

However, the agreement improves if the integration time-step Δt is reduced from 0.001 to 0.0002: for $\rho = 0.05$, $T = 1.2$ in the $N = 2000$ system, A^2 drops from 2061 to 29.84 and $\langle\tau\rangle$ from 16.29 to 15.72; the lower value of $\langle\tau\rangle$ corresponds better to the observed survival function. The data change very little with respect to $\Delta t = 0.001$ and are not shown in Fig. 5.6 to avoid cluttering. This indicates that the discrepancy is due to the finite integration time-step and can be controlled through the latter. The hypothesis is confirmed reducing Δt further: for $\Delta t = 10^{-4}$, $A^2 = 3.78$, and finally for $\Delta t = 10^{-5}$, $A^2 = 0.686 < 1.957$, i.e. the required threshold. The same trend is evident in the $N = 100\,000$ system, see Fig. 5.7, though even smaller time

steps would be necessary to reach the threshold because the average waiting time decreases inversely proportionally to the interface area.

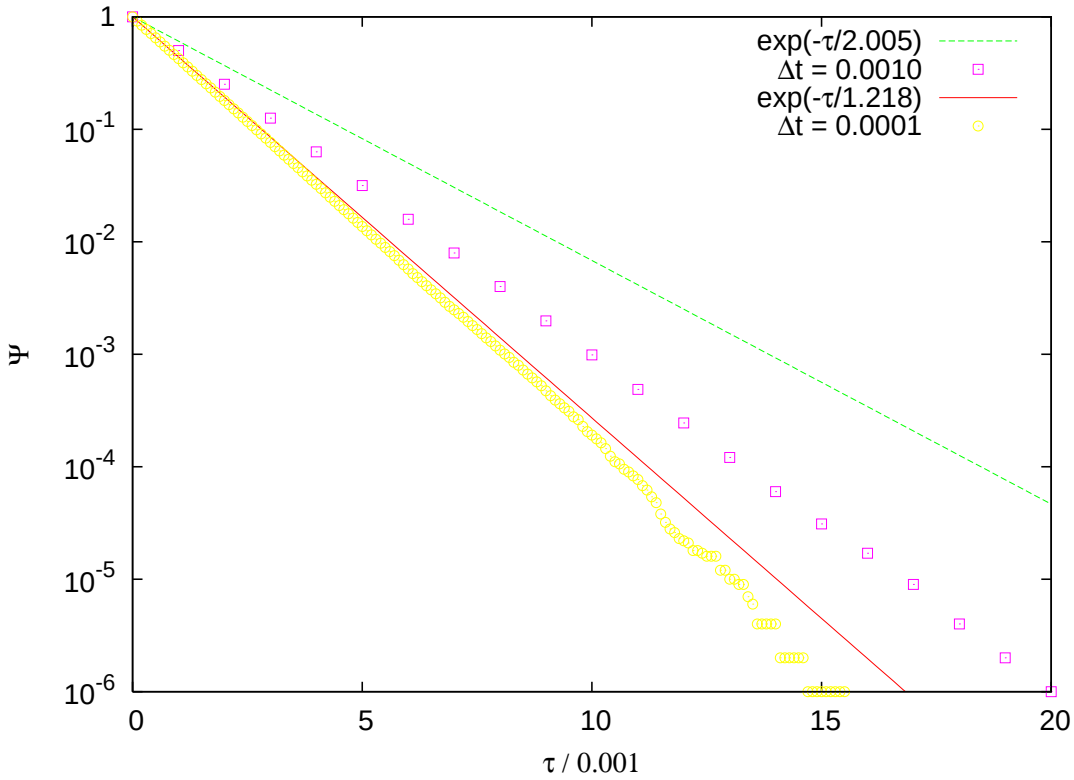

Figure 5.7: Reducing the integration time-step Δt improves the agreement between the observed survival function and an exponential function with a time constant equal to the average waiting time; system with $N = 100\,000$, $\rho = 0.05$, $T = 1.2$.

As suggested by intuition, the average waiting time decreases with higher density and temperature, but also whith a larger interface area S between the two parts of the box. Actually, the product $\langle\tau\rangle S$ is a constant for a given density and temperature. The survival functions of systems with different sizes overlap if $\langle\tau\rangle$ is multiplied with the interface area. This is shown in Fig. 5.8, where it is also clear that there are no changes due to the finite size of the system for $N \geq 1000$ (after correcting for the interface area, the survival function of $N = 500$ is slightly displaced from all the others).

A better strategy than reducing the time-step is to interpolate the time of the barrier crossing within a conventional time-step: this way the waiting times can be determined with floating-point precision rather than as integer multiples of Δt, there will not be changes in $\Delta z > 2$, and it is likely that good results can be obtained with the maximum Δt compatible with energy conservation. Though we believe that the major effect of a finite Δt is through sampling, because without interpolation waiting times are systematically overestimated by a fraction of Δt, another effect is through the approximation of the true canonical dynamics. Indeed, with a soft potential this approximation can be reduced only in the limit of $\Delta t \to 0$, but it can be avoided completely in a system of hard spheres. Work on both lines, interpolation of the waiting times and hard spheres, is in progress.

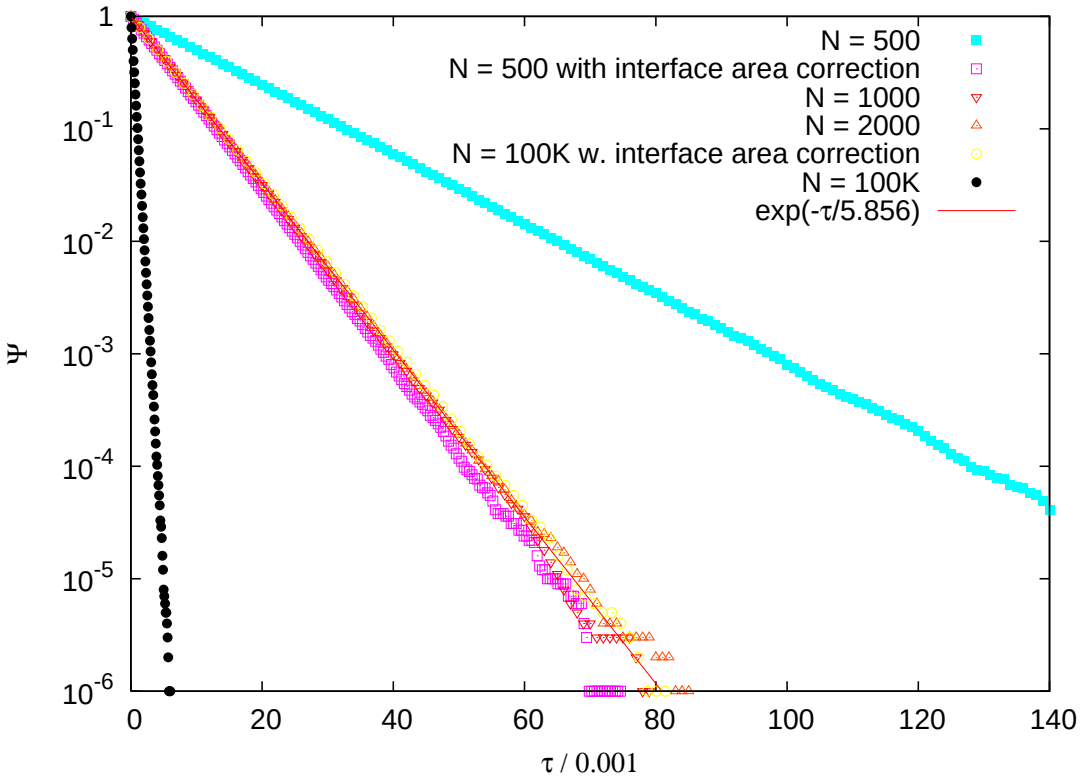

Figure 5.8: Survival functions for $\rho = 0.7$, $T = 1.6$) and different system sizes. They overlap if $\langle\tau\rangle$ is multiplied with the ratio of the interface area to the interface area of the systems with $N = 1000$ or 2000 (that are equal because the former is the only one with a cubic unit box, while all the others have side ratios of 2:1:1). A finite-size effect is noticeable only on the smallest system.

5.4 Conclusions

In summary, we have studied the Ehrenfest urn whith a realistic model of condensed matter, the Lennard-Jones fluid. The Ehrenfest urn has been defined by Mark Kac the best model ever envisaged in statistical mechanics [38], yet it has also been criticized as a marvellous exercise too far removed from reality [25]. In the 100th anniversary of the Ehrenfests' original paper, we have shown that this criticism is unjustified, since computer "experiments" allow to follow the motion of molecules and to count how many are on one side of a box or the other at a given time. We have studied the behaviour of the pure-jump stochastic process $\Delta z = |P - Q|$ induced by the deterministic dynamics under coarse graining, where P is the number of fluid particles on the left-hand side of the simulation box and Q that on the right-hand side. We have performed simulations with periodic boundary conditions and with walls in one direction, finding that the presence of walls does not affect the results. We have found that in the gas phase the observed transition probabilities follow the predictions of the Ehrenfest theory, and that the waiting time distribution between successive variations of Δz, though not strictly exponential, becomes closer to an exponential reducing the integration time-step; therefore, in the limit of a vanishing time-step, we found that the corresponding pure-jump process is Markovian. To our knowledge, this is the first characterization of a pure-jump stochastic process induced by a deterministic dynamics under coarse graining. In the future, we plan to

further study the stochastic process presented here interpolating the waiting times to higher precision, simulating systems of hard spheres to avoid approximations in the dynamics due to a finite integration time-step, and investigating the pure-jump process in a coarse grained configuration space as required by the theory developed by Boltzmann. Our results [39] corroborate the Markovian hypothesis lying at the foundation of statistical mechanics [1].

Chapter 6

Liquid crystals

As we have seen in the previous chapters and already noticed by Penrose [1], Markovianity is an important concept in physics, accounting for the memory of the system of interest. Markovianity holds for dilute gases, and partially even for dense Lennard-Jones fluids, which allows us to derive well-known thermodynamic relations. In the original derivation of his equation and the H-theorem, Ludwig Boltzmann used the *Stoßzahlansatz*, which corresponds to Markovianity. A consequence of these considerations is that the velocity distribution of molecules obeys the Maxwell-Boltzmann law. However, of course not every process is memoryless. A reason why a system looses its memory is the large number of particles and the central limit theorem. For example a system composed of three hard spheres under periodic boundary conditions is clearly non Markovian, as Fig. 6.1 shows. The waiting times are not exponentially distributed and the velocity density follows a semicircle law instead of a Gaussian law leading to the Maxwell-Boltzmann law for the velocity modulus.

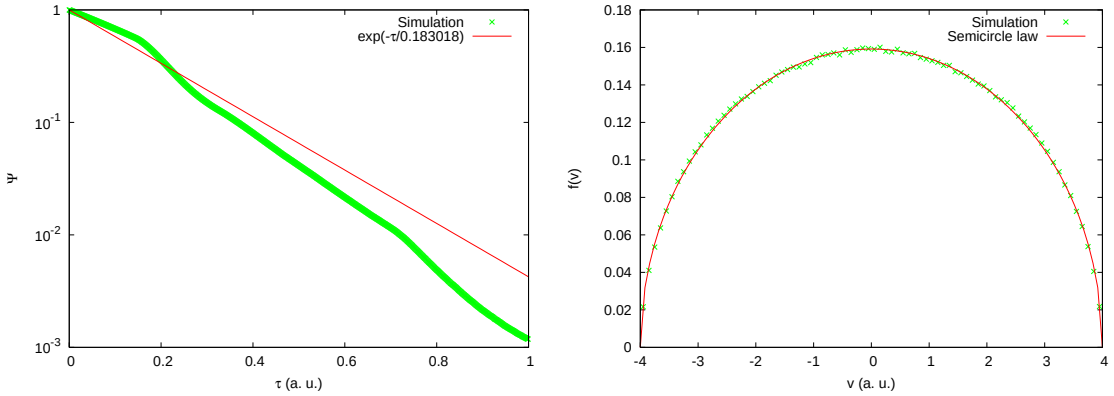

Figure 6.1: Survival function of the waiting times between collisions (left) and density of the components of the velocities (right) for a system of $N = 3$ hard discs in two dimensions with $\langle E\rangle/N = \langle v^2\rangle/2 = 4$. The simulation data is compared with the theoretical exponential distribution $\exp(-t/\langle\tau\rangle)$, where $\langle\tau\rangle$ is the average waiting time, and the semicircle law $f(v) = \frac{1}{2\pi\langle E\rangle}\sqrt{4\langle E\rangle - v^2}$.

A further reason why a process may remember its history and thus be non-Markovian is that the system is trapped in a certain region of the available phase space, which means ergodicity breaking. A common example for ergodicity breaking is a ferromagnetic system, where a non-zero magnetization is adopted below the Curie temperature, while the ergodic hypothesis would imply zero magnetization.

There are various systems exhibiting non-ergodic behaviour. For example it has been suggested that the glass transition in cooled simple liquids is a dynamic transition from an ergodic to a nonergodic state due to the "cage effect" where the particles get increasingly localized, see [40] and references included therein.

Of course complex fluids like liquid crystals, where the phase space includes additional degrees of freedom, can behave in a non-ergodic way as well. Examples are given in reference [41], where mode-coupling theory is used to determine non-ergodicity parameters in a system composed of hard ellipsoids, and in reference [42], where non-ergodic behaviour is reported in a liquid-crystalline system.

The present chapter will be structured as follows. In section 6.1 the most important liquid crystalline phases will be reviewed briefly. Section 6.2 introduces the nematic order parameter and order tensor. In section 6.3 the two most common molecular theories of nematic order, the Onsager hard rod model and the Maier-Saupe mean field theory, will be sketched, and the following sections will be devoted to the studies of our system of interest, a Gay-Berne mesogen confined in a cylindrical geometry.

6.1 The liquid crystalline phase

Even though the expression "liquid crystal" has grown historically and is nowadays established, it may be somehow misleading. In 1888 the Austrian botanical physiologist Friedrich Reinitzer found evidence of a new state of matter by examining the physico-chemical properties of various derivatives of cholesterol. Upon heating cholesteryl benzoate he observed two "melting points": at 145.5°C the crystals turned into a cloudy liquid which became clear at 178.5°C. This phenomenon was further investigated by Otto Lehmann, who coined the term "liquid crystal", since the substances could flow like liquids and exhibited crystalline properties like birefringence as well. More properly, one could say that the substances are found in "mesomorphic phases", i.e. in intermediate phases.

Liquid crystalline phases are characterized by a long-range orientational order and a partial or complete positional disorder responsible for the flow properties. There are different mechanisms leading to these phases. The long-range orientational order of *lyotropic* liquid crystals is induced by addition of a solvent, whereas *thermotropic* liquid crystals organize themselves in a certain temperature range. The different degrees of order are characterized by different phases for different anisotropies of the constituent molecules. The two main classes of anisotropic molecules are constituted of *calamitic*, i.e. rodlike, and *discotic*, i.e. platelike, shapes. Typical structures of calamitic and discotic liquid crystals can be seen in Fig. 6.2.

6.1.1 Nematics

The main properties of the nematic mesophase are preferential alignment of the constituent molecules and no positional order of the centers of mass. The alignment is characterized by a unit vector, the so-called director $\hat{\mathbf{n}}$, where the states $\hat{\mathbf{n}}$ and $-\hat{\mathbf{n}}$ are indistinguishable in the case of non-polar cylindrically symmetric molecules.

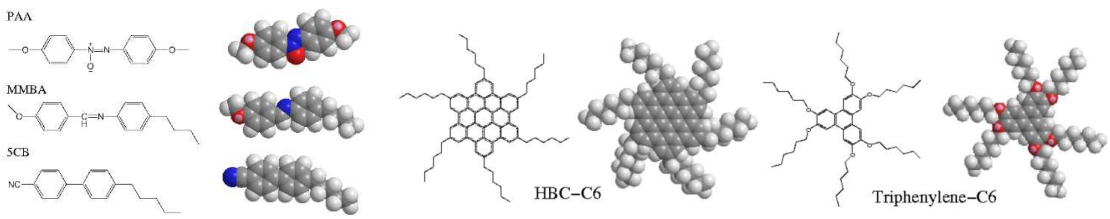

Figure 6.2: Typical thermotropic liquid crystals [43]. Left: three calamitic mesogens. Center and right: two discotic mesogens, a derivative of hexabenzocoronene and 2,3,6,7,10,11-hexakishexyloxytriphenylene.

Figure 6.3: Nematic (left) and cholesteric phases (middle and right) for a calamitic liquid crystal [44]. The phase shown on the right is called smectic C*, where the molecules are arranged in layers, and the tilt angle varies from layer to layer.

6.1.2 Smectics

Additionally to the preferential alignment of the molecules, a smectic liquid crystal shows one-dimensional positional order: the molecules organize themselves in layers. Inside the layers there is no long-range order of the centers of mass, corresponding to a two-dimensional liquid. There are different smectic phases. For example in the smectic A phase the orientation of the molecules is perpendicular to the layer, whereas in the smectic C phase the orientation of the molecules is tilted. Fig. 6.4 shows a smectic A and a smectic C phase.

6.1.3 Cholesterics

Cholesteric phases are composed of chiral molecules, i.e. of molecules that are not identical with their mirror image. Locally the cholesteric phase looks like a nematic or smectic phase, however the director varies in space forming a helix. If the director is measured in equidistant planes perpendicular to the helical axis, a well defined distortion angle can be observed. A nematic and two cholesteric phases are shown schematically in Fig. 6.3.

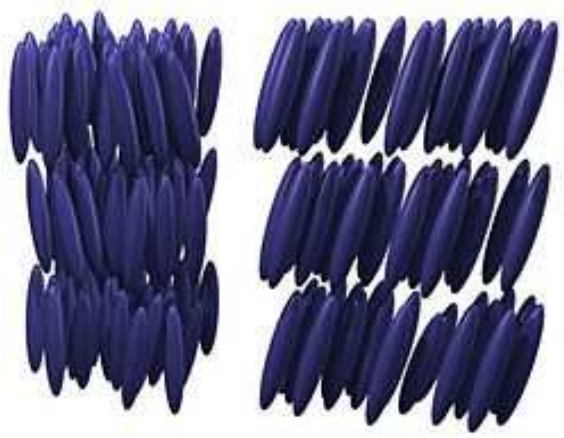

Figure 6.4: Smectic A (left) and smectic C phase (right) for a calamitic liquid crystal [44].

6.1.4 Columnar phases

Since the discovery of liquid crystalline phases, there have been many technical applications arising from this state of matter, especially for calamitic liquid crystals. The most famous among them are liquid crystal displays (LCDs) and liquid crystal thermometers. For a relatively long period the accepted principle was that the occurrence of liquid crystalline phases was coupled to a rodlike shape of the constituent molecules. However, in 1977 Chandrasekhar and his coworkers [45] discovered that disc-shaped molecules exhibit stable mesophases as well, showing a nematic phase and an even more ordered phase than the smectic one, the columnar phase, where molecules are stacked on each other like coins in a pile. The latter property is of practical interest, since the overlap of π-orbitals in the columnar phase leads to a good conductivity along the column axis [46, 47] but not across it, and hence applications in organic optoelectronic devices like light emitting diodes, field effect transistors and solar cells can be achieved.

6.2 Order parameter and order tensor

The orientation of uniaxial molecules, both calamitic and discotic, can be described by a unit vector $\hat{\mathbf{e}}_i$, where the index i labels the molecule. In the reference frame of the director, where $\hat{\mathbf{n}} = (0, 0, 1)$, the unit vector $\hat{\mathbf{e}}_i$ can be written in spherical coordinates:

$$\begin{aligned} e_{i,x} &= \sin\theta\cos\phi \\ e_{i,y} &= \sin\theta\sin\phi \\ e_{i,z} &= \cos\theta. \end{aligned} \tag{6.1}$$

The orientational order can be described by the density function $f(\theta, \phi)$, where $f(\theta, \phi)d\Omega$ gives the probability that the orientation of a molecule points in a small solid angle $d\Omega = \sin\theta d\theta d\phi$ around the direction (θ, ϕ). Unlike for ferromagnetic systems, where the order is measured by the magnetization vector $\mathbf{M}$, the choice

of an order parameter in a nematic phase is less trivial, because we have no ϕ-dependence in the density function, i.e. $f(\theta, \phi) = f(\theta)$, and $f(\theta) = f(\pi - \theta)$, which means that, as mentioned before, the directions $\hat{\mathbf{n}}$ and $-\hat{\mathbf{n}}$ are equivalent. Hence the first intuition of measuring the degree of alignment by the average

$$\langle \cos\theta \rangle = \langle \hat{\mathbf{e}}_i \cdot \hat{\mathbf{n}} \rangle = \int_\Omega \cos\theta f(\theta)\, d\Omega \tag{6.2}$$

fails, because Eq. (6.2) vanishes and therefore we do not get the desired information. Furthermore all the odd moments $\langle \cos^{2k+1}\theta \rangle$ with $k \in \mathbb{N}$ vanish too. A possible order parameter can be constructed by using as the first non-vanishing moment the average of the second Legendre polynomial

$$\begin{aligned} S &= \langle P_2(\cos\theta) \rangle = \frac{1}{2} \left\langle 3\cos^2\theta - 1 \right\rangle \\ &= \frac{3}{2} \int_\Omega \cos^2\theta f(\theta)\, d\Omega - \frac{1}{2}. \end{aligned} \tag{6.3}$$

In the case of perfect alignment with the molecules parallel to the preferred direction in space $\hat{\mathbf{n}}$, we have $\cos\theta = \pm 1$ and hence $S = 1$. If the molecules are oriented perpendicular to $\hat{\mathbf{n}}$, $\cos\theta = 0$ and $S = -1/2$. A completely disordered state is characterized by a uniform distribution of $f(\theta)$. Because of the normalization condition

$$\int_\Omega f(\theta)\, d\Omega = 1 \tag{6.4}$$

the density function is $f(\theta) = 1/4\pi$. Inserting this into Eq. (6.3), the order parameter for an isotropic sample is $S = 0$; see also Eq. (6.18) below.

The order parameter of the next non-vanishing moment is

$$\langle P_4(\cos\theta) \rangle = \frac{1}{8} \left\langle 35\cos^4\theta - 30\cos^2\theta + 3 \right\rangle. \tag{6.5}$$

The Legendre polynomials form a complete orthogonal set, and hence the choice

$$S_l = \langle P_l(\cos\theta) \rangle \tag{6.6}$$

is convenient because it allows to expand the density function $f(\theta)$ in this basis:

$$f(\cos\theta) = \sum_{l=0}^{\infty} c_l P_l(\cos\theta). \tag{6.7}$$

Defining the inner product $\langle f(x), g(x) \rangle = \int_{-1}^{1} f(x) g(x)\, dx$ for two arbitrary functions $f(x)$ and $g(x)$ mapping the interval $(-1, 1)$ onto the real numbers $\mathbb{R}$, and applying it on Eq. (6.7) from both sides, we have

$$\langle P_m(\cos\theta), f(\cos\theta) \rangle = \sum_{l=0}^{\infty} c_l \langle P_m(\cos\theta), P_l(\cos\theta) \rangle. \tag{6.8}$$

Using the orthogonality relation [48]

$$\langle P_m(x), P_l(x) \rangle = \frac{2}{2l+1} \delta_{ml} \tag{6.9}$$

the expansion coefficient is

$$\begin{aligned} c_m &= \frac{2m+1}{2}\int_{-1}^{1} P_m(\cos\theta) f(\cos\theta)\, d\cos\theta \\ &= \frac{2m+1}{2}\int_{0}^{\pi} P_m(\cos\theta) f(\theta)\sin\theta\, d\theta \\ &= \frac{2m+1}{4\pi}\int_{\Omega} P_m(\cos\theta) f(\theta)\, d\Omega \\ &= \frac{2m+1}{4\pi} S_m, \end{aligned} \tag{6.10}$$

and, upon inserting the expansion coefficient into Eq. (6.7), one obtains the final expansion of the density function:

$$f(\theta) = \sum_{l=0}^{\infty} \frac{2l+1}{4\pi} S_l P_l(\cos\theta). \tag{6.11}$$

A natural generalization of Eq. (6.3) for systems where the director is not known *a priori* is the symmetric second-rank tensor

$$\begin{aligned} \mathbf{Q} &= \frac{1}{N}\sum_{i=1}^{N}\left(\frac{3}{2}\hat{\mathbf{e}}_i \otimes \hat{\mathbf{e}}_i - \frac{1}{2}\mathbf{I}\right) \\ &= \frac{1}{2}\left\langle 3\hat{\mathbf{e}}_i \otimes \hat{\mathbf{e}}_i - \mathbf{I}\right\rangle, \end{aligned} \tag{6.12}$$

with components

$$Q_{\alpha\beta} = \frac{1}{2}\left\langle 3e_{i,\alpha}e_{i,\beta} - \delta_{\alpha\beta}\right\rangle, \tag{6.13}$$

and $\alpha, \beta = (x, y, z)$. The order tensor $\mathbf{Q}$ is traceless since

$$\text{tr } \mathbf{Q} = \frac{3}{2}\left\langle e_{i,x}^2 + e_{i,y}^2 + e_{i,z}^2\right\rangle - 3\cdot\frac{1}{2} = 0 \tag{6.14}$$

which, together with the symmetry of $\mathbf{Q}$, reduces the number of independent components from 9 to 5. A perfect alignment, where the molecules are oriented parallel to the z-axis, means that $\hat{\mathbf{e}}_i = (0, 0, 1)$ and Eq. (6.12) delivers

$$\mathbf{Q} = \begin{pmatrix} -\frac{1}{2} & 0 & 0 \\ 0 & -\frac{1}{2} & 0 \\ 0 & 0 & 1 \end{pmatrix}. \tag{6.15}$$

If the molecules are oriented perpendicular to the z-axis we have

$$\mathbf{Q} = \begin{pmatrix} -\frac{1}{4} & 0 & 0 \\ 0 & -\frac{1}{4} & 0 \\ 0 & 0 & -\frac{1}{2} \end{pmatrix}. \tag{6.16}$$

It suffices to compute Q_{zz} to prove this: due to the rotational symmetry with respect to ϕ we know that $\langle e_x\rangle = \langle e_y\rangle$ and $\langle e_x e_y\rangle = \langle e_y e_x\rangle = 0$, and hence $Q_{xx} = Q_{yy}$ and $Q_{xy} = Q_{yx} = 0$. Additionally using the fact that the order tensor is traceless, we can compute Q_{xx} and Q_{yy} from Q_{zz}, which is

$$Q_{zz} = \frac{3}{2}\langle e_z^2\rangle - \frac{1}{2} = -\frac{1}{2}. \tag{6.17}$$

This proves Eq. (6.16), since all off-diagonal elements where e_z is included vanish due to $e_z = 0$. For the isotropic phase the order tensor is the zero matrix. It is easy to see that the mixed components $Q_{\alpha\beta}$ with $\alpha \neq \beta$ vanish, and in the following only $Q_{zz} = 0$ will be proven. Knowing that in the isotropic phase $f(\theta, \phi) = 1/4\pi$ one obtains:

$$\begin{aligned} Q_{zz} &= \left\langle \frac{3}{2} e_z^2 - \frac{1}{2} \right\rangle \\ &= \frac{3}{2} \int_\Omega \cos^2\theta f(\theta,\phi)\, d\Omega - \frac{1}{2} \\ &= \frac{3}{4} \int_0^\pi \cos^2\theta \sin\theta\, d\theta - \frac{1}{2} \\ &= \frac{3}{4} \int_{-1}^1 u^2 du - \frac{1}{2} \\ &= \frac{1}{2} - \frac{1}{2} = 0. \end{aligned} \tag{6.18}$$

The director is determined diagonalising the order tensor and is associated with the eigenvector corresponding to the largest eigenvalue.

6.3 Molecular theories

The Onsager hard rod model and the Maier-Saupe mean field theory were the first to describe the formation of the nematic phase on a molecular level. Although these models have been improved and refined to account for more realistic situations, they provide a basic understanding of the mechanisms leading to the formation of mesomorphic phases. Hence the key thoughts of these two models will be presented in the next two subsections.

6.3.1 Onsager hard rod model

A simple model predicting phase transitions from the isotropic to the nematic state with varying concentration is the hard rod model proposed by Lars Onsager [49]. This theory considers the volume excluded from the center of mass of one idealized cylinder as it approaches another. If the cylinders are oriented parallel to each other, the excluded volume of the centers of mass is small as compared to the situation where two cylinders are at some angle towards each other. This means that in the former case there are more states accessible to the positions of the cylinders, and hence the positional entropy is larger for a parallel arrangement, whereas an isotropic hard rod fluid is characterized by a higher orientational entropy since there is no preferred direction. The degree of order results from a competition between positional and orientational effects, and the concentration of cylinders is the parameter determining which effect dominates. Intuitively for low densities the isotropic state is more stable, whereas for higher concentrations the aligned state is favoured, and indeed Onsager's theory predicts a first order isotropic-nematic phase transition as the density increases.

Starting from the free energy per particle of a dilute gas of hard spheres with

concentration c,

$$F = F_0 + k_\mathrm{B}T\left(\log c + \frac{1}{2}c\beta_1\right) + o(c^2), \tag{6.19}$$

where F_0 is an additive constant and β_1 is the excluded volume, which for hard spheres with radius r is given by $\beta_1 = \frac{4}{3}\pi(2r)^3$, the generalization for anisotropic particles reads

$$\begin{aligned} F &= F_0 + k_\mathrm{B}T\left(\log c + \int \log\left(4\pi f_{\hat{\mathbf{a}}}\right) f_{\hat{\mathbf{a}}}\, d\Omega \right. \\ &\quad \left. + \frac{1}{2}c\int\int \beta_1(\hat{\mathbf{a}},\hat{\mathbf{a}}') f_{\hat{\mathbf{a}}} f_{\hat{\mathbf{a}}'}\, d\Omega d\Omega'\right) + o(c^2). \end{aligned} \tag{6.20}$$

Here $f_{\mathbf{a}}d\Omega$ is the probability of a rod pointing in a small solid angle $d\Omega$ around the unit vector $\hat{\mathbf{a}}$. In the limit of infinitely long and thin rods the Onsager theory becomes exact since higher order terms vanish. Requiring that the equilibrium distribution corresponds to a minimum of the free energy as a functional of $f_{\hat{\mathbf{a}}}$ under the normalization constraint

$$\int f_{\hat{\mathbf{a}}}\, d\Omega = 1, \tag{6.21}$$

one gets

$$\delta F = k_\mathrm{B}T\lambda \int \delta f_{\hat{\mathbf{a}}} d\Omega, \tag{6.22}$$

and hence

$$\log(4\pi f_{\hat{\mathbf{a}}}) = \lambda - 1 - c\int \beta_1(\hat{\mathbf{a}},\hat{\mathbf{a}}') f_{\hat{\mathbf{a}}'}\, d\Omega'. \tag{6.23}$$

The excluded volume can be approximated by $\beta_1(\hat{\mathbf{a}},\hat{\mathbf{a}}') \approx 2L^2D|\sin\gamma|$, where end effects have been ignored, L and D are the length and the diameter of the idealized cylinders respectively, and $\gamma = \arccos(\hat{\mathbf{a}}\cdot\hat{\mathbf{a}}')$. Since $\sin(\arccos a) = \sqrt{1-a}$, we can also write $\beta_1(\hat{\mathbf{a}},\hat{\mathbf{a}}') \approx 2L^2D\sqrt{1-\hat{\mathbf{a}}\cdot\hat{\mathbf{a}}'}$. Eq. (6.23) can be solved numerically; however in order to reduce the computational effort Onsager proposed a trial function ansatz. The trial function depends on the variational parameter α; using the fact that the molecules are cylindrically symmetric and hence the orientational distribution function depends on the polar angle θ only, it reads:

$$f_{\hat{\mathbf{a}}} = f(\theta) = \frac{\alpha\cosh[\alpha\cos(\theta)]}{4\pi\sinh(\alpha)}. \tag{6.24}$$

Minimizing the free energy given by Eq. (6.20) with respect to α one obtains a function depending on the concentration c exhibiting a first order phase transition from the isotropic to the nematic state.

6.3.2 Maier-Saupe mean field theory

As already mentioned at the beginning of the previous subsection, the Onsager theory is athermal since it uses the density of the mesogens as the parameter determining the degree of order. As a consequence of the fact that the free energy given by Eq. (6.20) results from a virial expansion to second order, the elongation of the particles must be very high as opposed to realistic systems where aspect ratios are modest. The isotropic-nematic transition density predicted by the Onsager theory

is too low compared to that of real thermotropic mesogens, and the jump in density too high. A molecular mean field theory describing the isotropic-nematic transition was introduced by Maier and Saupe [50], who used an analogy to the 'molecular field approximation' introduced by Weiss for ferromagnets.

Since the change in temperature has an influence on the volume, the Gibbs free energy per particle $G(P,T)$ depending on the pressure P and the temperature T is a more suitable thermodynamic potential than the Helmholtz free energy, and has the form

$$G(P,T) = G_{\mathrm{I}}(P,T) + k_{\mathrm{B}}T \int \log(4\pi f_{\hat{\mathbf{a}}}) f_{\hat{\mathbf{a}}}\, d\Omega + G_1(P,T,S), \tag{6.25}$$

where $G_{\mathrm{I}}(P,T)$ is the free enthalpy of the isotropic phase and the second term again accounts for the loss in rotational entropy associated with a non-uniform angular distribution. The third term is assumed to be quadratic in the order parameter $S = \langle P_2(\cos\theta)\rangle$:

$$G_1 = -\frac{1}{2}U(P,T)S^2, \tag{6.26}$$

where U is a positive quantity. The first variation of Eq. (6.25) under the constraint that the angular distribution function is normalized reads

$$\delta G = \lambda \int \delta f_{\hat{\mathbf{a}}}\, d\Omega. \tag{6.27}$$

The variation of the isotropic part is zero, and the variation of G_1 is computed straightforwardly using the definition of the order parameter, which gives

$$\log(4\pi f_{\hat{\mathbf{a}}}) = \lambda - 1 + \frac{1}{2}\frac{US}{k_{\mathrm{B}}T}(3\cos^2\theta - 1), \tag{6.28}$$

or

$$f_{\hat{\mathbf{a}}} = f(\theta) = \frac{1}{4\pi Z}\exp\left(m\cos^2\theta\right), \tag{6.29}$$

with

$$m = \frac{3}{2}\frac{US}{k_{\mathrm{B}}T}, \tag{6.30}$$

and the normalization constant

$$Z = \int_0^1 e^{mx^2} dx. \tag{6.31}$$

The density function given by Eq. (6.29) depends implicitly on the order parameter S, and therefore a self-consistency condition for the latter is needed. Inserting the density function into the definition of the order parameter given by Eq. (6.3) we get:

$$\begin{aligned} S &= \frac{3}{2Z}\int_0^1 x^2 e^{mx^2}\, dx - \frac{1}{2} \\ &= \frac{3}{2Z}\frac{\partial Z}{\partial m} - \frac{1}{2}. \end{aligned} \tag{6.32}$$

Eqs. (6.30) and (6.32) can be solved graphically and the stability of the solutions analyzed. Below a critical temperature T_{c} corresponding to $k_{\mathrm{B}}T_{\mathrm{c}}/U = 4.55$ the nematic phase is stable, whereas for temperatures higher than T_{c} the isotropic phase is stable; there is a first-order phase transition at $T = T_{\mathrm{c}}$. The order parameter jumps from zero to $S = 0.44$ just below the critical temperature.

6.4 Discotics in cylindrical confinement

As already mentioned in Subsection 6.1.4, the occurrence of the columnar phase is of both fundamental and practical interest. Also for technical applications a proper understanding of the thermodynamic properties of the material is useful in order to be able to control certain properties like the overall alignment of liquid crystalline molecules. One possibility to achieve this is confinement. There is experimental evidence that discotic liquid crystals such as triphenylene derivatives like Adamantane-pentakis(butyloxy)triphenylene confined in ordered porous templates such as aluminium oxide (also known as alumina) organize themselves in a columnar phase at the pore center, surrounded by a shell with a broad orientational distribution and homeotropic (face-on) anchoring on the pore walls [51].

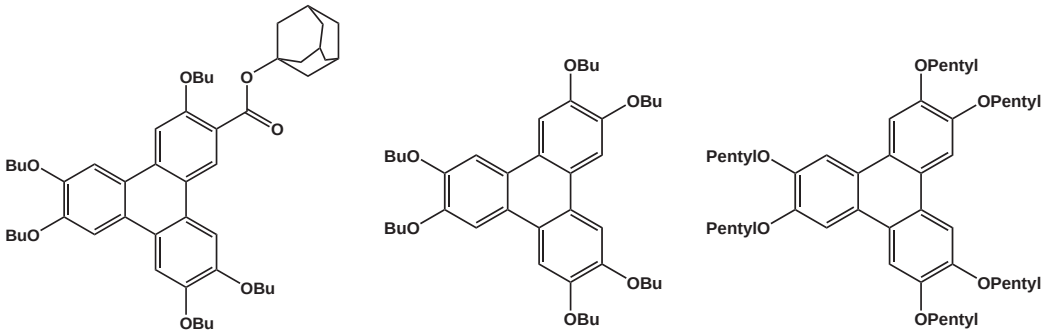

Figure 6.5: From left to right: chemical structures of adamantane-pentakis(butyloxy)triphenylene (Ada-PBT), hexakis(butyloxy)triphenylene (HBT) and hexakis(pentyloxy)triphenylene (HPT). Ada-PBT was investigated experimentally in Refs. [51, 52]; HPT was investigated experimentally in Ref. [53]. The coarse grained potential introduced in this chapter is suited as an approximate model of flat molecules with a symmetry axis like HBT and HPT [54, 55].

The occurrence of the above mentioned structure is not unique: it was found to depend on parameters like the preparation of the cylindrical surface of the wall, favouring different kinds of anchoring [53], the pore radius, and the thermodynamic path along which the system has been brought to its final state. Thus it is particularly interesting to study the influence of the surface interaction and of the pore radius on the supramolecular architecture of the whole system.

Computer simulation is a useful tool for helping to understand these properties since it gives insight at the molecular level, and different parameters and initial configurations can be controlled more easily than in experiments. So far, for discotic liquid crystals fewer simulations have been carried out than for calamitic ones. This applies to the bulk both at molecular [56, 57, 58, 54] and atomic detail [43, 59], and even more to confined geometries There are only few simulations of discotics in slab geometry [60, 55, 61] and just two in cylindrical geometry [52, 62], the first of which one is by ourselves. A reason for this may be that, as a consequence of the geometry, the potential between a molecule and a cylindrical wall is more complicated than in the slab case. This can be readily seen for atoms interacting via the Lennard-Jones

potential,

$$U_{ij}(r_{ij}) = 4\epsilon_0 \left[\left(\frac{\sigma_0}{r_{ij}} \right)^{12} - \left(\frac{\sigma_0}{r_{ij}} \right)^{6} \right], \tag{6.33}$$

where r_{ij} is the interatomic distance, $\sqrt[6]{2}\sigma_0$ is the equilibrium distance, and ε_0 is the corresponding well depth. For a planar wall the atom-surface interaction is easy to work out and has been done by Steele in 1973 [31]. If the wall is taken perpendicular to the z-axis at a distance $(0,\ 0,\ r_{i\mathrm{w}})$ from molecule i, and assuming that the wall consists of a continuum of Lennard-Jones atoms with a density ρ_{w}, the atom-wall potential can be written as an integral over all positions $\mathbf{r}' = (r'_x, r'_y, r'_z)$ of the wall atoms:

$$U_{i\mathrm{w}}(r_{i\mathrm{w}}) = 4\rho_{\mathrm{w}}\epsilon_0 \int V(\mathbf{r}_i, \mathbf{r}')d\mathbf{r}', \tag{6.34}$$

with

$$V(\mathbf{r}_i, \mathbf{r}') = \left(\frac{\sigma_0}{|\mathbf{r}_i - \mathbf{r}'|} \right)^{12} - \left(\frac{\sigma_0}{|\mathbf{r}_i - \mathbf{r}'|} \right)^{6}. \tag{6.35}$$

Due to the translational invariance in the xy-plane, the origin of the coordinate system can be placed at the position $\mathbf{r}_i$ of molecule i; using cylinder coordinates the integral over the half-space $r_z \geq r_{i\mathrm{w}}$ in Eq. (6.34) can then be written in the form

$$U_{i\mathrm{w}}(r_{i\mathrm{w}}) = 8\pi\rho_{\mathrm{w}}\epsilon_0 \int_{r_{i\mathrm{w}}}^{\infty} \int_0^{\infty} \left[\frac{\sigma_0^{12}}{(\varrho^2 + r_z'^2)^6} - \frac{\sigma_0^6}{(\varrho^2 + r_z'^2)^3} \right] \varrho\, d\varrho dr'_z, \tag{6.36}$$

where $\varrho^2 = r_x'^2 + r_y'^2$. This can be evaluated by elementary means and finally Steele's potential for a flat wall can be written as

$$U_{i\mathrm{w}}(r_{i\mathrm{w}}) = \frac{2\pi\rho_{\mathrm{w}}\epsilon_0\sigma_0^3}{3} \left[\frac{2}{15} \left(\frac{\sigma_0}{r_{i\mathrm{w}}} \right)^9 - \left(\frac{\sigma_0}{r_{i\mathrm{w}}} \right)^3 \right]. \tag{6.37}$$

Finding the molecule-surface potential for systems confined in a cylindrical geometry is not as easy. The integral over an infinitely thick region outside a cylinder of radius R is awkward even for Lennard-Jones atoms, leading to elliptic type integrals and hypergeometric functions of the type ${}_2F_1(a, b; c, x)$ [63]:

$$\begin{aligned} U_{i\mathrm{w}}^{p,q}(r_{i\mathrm{w}}) &= 2\pi^2\rho_{\mathrm{w}}\varepsilon_0 C_{p,q} \\ &\quad \times \left[\frac{(q-5)!!}{(q-2)!!} \frac{\sigma_0^q R^{q-3}}{(R^2 - r_{i\mathrm{c}}^2)^{q-3}} {}_2F_1 \left(\frac{3-q}{2}, \frac{5-q}{2}; 1; \left(\frac{r_{i\mathrm{c}}}{R} \right)^2 \right) \right. \\ &\quad \left. - \frac{(p-5)!!}{(p-2)!!} \frac{\sigma_0^p R^{p-3}}{(R^2 - r_{i\mathrm{c}}^2)^{p-3}} {}_2F_1 \left(\frac{3-p}{2}, \frac{5-p}{2}; 1; \left(\frac{r_{i\mathrm{c}}}{R} \right)^2 \right) \right], \end{aligned} \tag{6.38}$$

where $r_{i\mathrm{c}} = R - r_{i\mathrm{w}}$, $C_{\mathrm{p,q}} = \frac{q}{q-p} \left(\frac{q}{p} \right)^{\frac{p}{q-p}}$, and p, q are the exponents of the inverse distance; in the Lennard-Jones case $C_{6,12} = 4$. However, if the radius of the confining cylinder ist not too small, the first attempt to simplify Eq. (6.38) is to use Eq.(6.37), thus disregarding the curvature of the wall. Fiq. (6.4) shows three dimensional plots of the two potentials.

In what follows, the phase behaviour of a model Gay-Berne ellipsoid in cylindrical confinement will be studied via MD simulation, and therefore the next three subsections will be devoted to the used intermolecular and wall potentials and the derivation of the forces and torques therefrom.

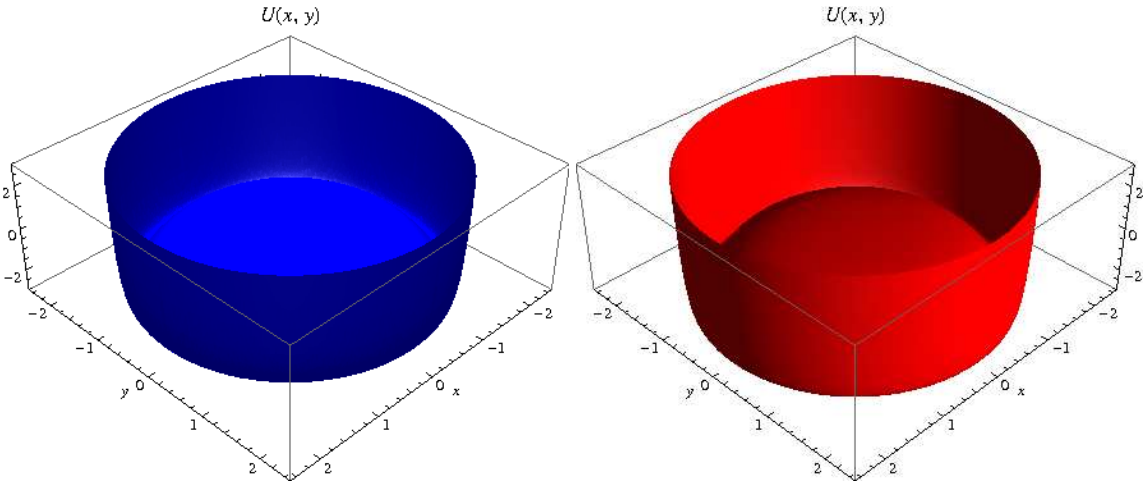

Figure 6.6: Comparison of the wall potentials for the cylindrical confinement given by Eqs. (6.37) (left, blue) and (6.38) (right, red).

6.4.1 Intermolecular interactions

For the interaction between two particles we use the Gay-Berne [64] potential with the Luckhurst extension for discotic molecules [57]:

$$U_{ij}(\mathbf{r}_{ij}, \hat{\mathbf{e}}_i, \hat{\mathbf{e}}_j) = 4\varepsilon(\hat{\mathbf{r}}_{ij}, \hat{\mathbf{e}}_i, \hat{\mathbf{e}}_j) \left[\varrho_{ij}^{-12}(\mathbf{r}_{ij}, \hat{\mathbf{e}}_i, \hat{\mathbf{e}}_j) - \varrho_{ij}^{-6}(\mathbf{r}_{ij}, \hat{\mathbf{e}}_i, \hat{\mathbf{e}}_j)\right], \tag{6.39}$$

with reduced distance

$$\varrho_{ij}(\mathbf{r}_{ij}, \hat{\mathbf{e}}_i, \hat{\mathbf{e}}_j) = \frac{r_{ij} - \sigma(\hat{\mathbf{r}}_{ij}, \hat{\mathbf{e}}_i, \hat{\mathbf{e}}_j) + \sigma_{\mathrm{ff}}}{\sigma_{\mathrm{ff}}}, \tag{6.40}$$

where σ and ε are shape and energy anisotropy functions depending on the distance between the molecular centers of mass $\mathbf{r}_{ij}$ and on the molecular orientations $\hat{\mathbf{e}}_i, \hat{\mathbf{e}}_j$. $\hat{\mathbf{r}}_{ij} = \mathbf{r}_{ij}/r_{ij}$ is the normalized intermolecular distance vector. The shape function $\sigma(\hat{\mathbf{r}}_{ij}, \hat{\mathbf{e}}_i, \hat{\mathbf{e}}_j)$ is given by

$$\sigma(\hat{\mathbf{r}}_{ij}, \hat{\mathbf{e}}_i, \hat{\mathbf{e}}_j) = \sigma_0 \left\{1 - \frac{\chi}{2}\left[\frac{(\hat{\mathbf{r}}_{ij}\cdot\hat{\mathbf{e}}_i + \hat{\mathbf{r}}_{ij}\cdot\hat{\mathbf{e}}_j)^2}{1+\chi\,\hat{\mathbf{e}}_i\cdot\hat{\mathbf{e}}_j} + \frac{(\hat{\mathbf{r}}_{ij}\cdot\hat{\mathbf{e}}_i - \hat{\mathbf{r}}_{ij}\cdot\hat{\mathbf{e}}_j)^2}{1-\chi\,\hat{\mathbf{e}}_i\cdot\hat{\mathbf{e}}_j}\right]\right\}^{-1/2}, \tag{6.41}$$

and the orientation-dependent well depth is given by

$$\begin{aligned}
\varepsilon(\hat{\mathbf{r}}_{ij}, \hat{\mathbf{e}}_i, \hat{\mathbf{e}}_j) &= \varepsilon_0[\varepsilon_1(\hat{\mathbf{e}}_i, \hat{\mathbf{e}}_j)]^\nu[\varepsilon_2(\hat{\mathbf{r}}_{ij}, \hat{\mathbf{e}}_i, \hat{\mathbf{e}}_j)]^\mu \\
\varepsilon_1(\hat{\mathbf{e}}_i, \hat{\mathbf{e}}_j) &= \left[1 - (\chi\,\hat{\mathbf{e}}_i\cdot\hat{\mathbf{e}}_j)^2\right]^{-1/2} \\
\varepsilon_2(\hat{\mathbf{r}}_{ij}, \hat{\mathbf{e}}_i, \hat{\mathbf{e}}_j) &= 1 - \frac{\chi'}{2}\left[\frac{(\hat{\mathbf{r}}_{ij}\cdot\hat{\mathbf{e}}_i + \hat{\mathbf{r}}_{ij}\cdot\hat{\mathbf{e}}_j)^2}{1+\chi'\,\hat{\mathbf{e}}_i\cdot\hat{\mathbf{e}}_j} + \frac{(\hat{\mathbf{r}}_{ij}\cdot\hat{\mathbf{e}}_i - \hat{\mathbf{r}}_{ij}\cdot\hat{\mathbf{e}}_j)^2}{1-\chi'\,\hat{\mathbf{e}}_i\cdot\hat{\mathbf{e}}_j}\right],
\end{aligned} \tag{6.42}$$

where ν and μ are parameters of the model changing the broadness and the depth of the potential, and

$$\begin{aligned}
\chi &= \frac{\kappa^2 - 1}{\kappa^2 + 1}, \qquad \kappa = \frac{\sigma_{\mathrm{ff}}}{\sigma_{\mathrm{ee}}} \\
\chi' &= \frac{\kappa'^{1/\mu} - 1}{\kappa'^{1/\mu} + 1}, \qquad \kappa' = \frac{\varepsilon_{\mathrm{ee}}}{\varepsilon_{\mathrm{ff}}}.
\end{aligned} \tag{6.43}$$

In the isotropic case, these functions are constants, and the potential depends only on the modulus r of the intermolecular distance risen to the well-known 6–12 powers. In our simulations we used the exponents $\mu = 1,\ \nu = 2$, the shape anisotropy $\kappa = 0.2$ and the energy anisotropy $\kappa' = 0.1$ which suits approximately molecules like HBT or HPT shown in Fig. 6.5 [54, 55]. Fig. 6.7 shows the Gay-Berne potential for particles with fixed orientations towards each other, where different scales have been used in the left and the right picture in order to clarify the magnitudes of the well-depths.

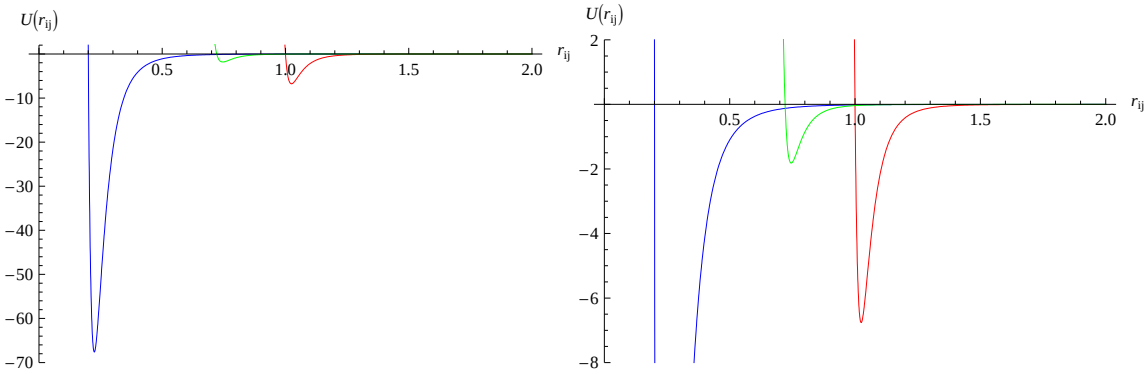

Figure 6.7: Intermolecular Gay-Berne potential for disclike particles with fixed orientation in different scales: the blue curve corresponds to the face-to-face configuration, where $\hat{\mathbf{r}}_{ij}\cdot\hat{\mathbf{e}}_i = \hat{\mathbf{r}}_{ij}\cdot\hat{\mathbf{e}}_j = \hat{\mathbf{e}}_i\cdot\hat{\mathbf{e}}_j = 1$, the red one to the edge-to-edge configuration, where $\hat{\mathbf{r}}_{ij}\cdot\hat{\mathbf{e}}_i = \hat{\mathbf{r}}_{ij}\cdot\hat{\mathbf{e}}_j = 0,\ \hat{\mathbf{e}}_i\cdot\hat{\mathbf{e}}_j = 1$, and the green one to the T-configuration, where $\hat{\mathbf{r}}_{ij}\cdot\hat{\mathbf{e}}_i = 1,\ \hat{\mathbf{r}}_{ij}\cdot\hat{\mathbf{e}}_j = \hat{\mathbf{e}}_i\cdot\hat{\mathbf{e}}_j = 0$, i.e. the orientations are perpendicular to each other in an edge-to-face configuration. The parameters are $\mu = 1$, $\nu = 2$, $\kappa = 0.2$ and $\kappa' = 0.1$.

6.4.2 Molecule-surface interactions

For systems of spherically asymmetric molecules confined in a slab geometry, the evaluation of the half-space integral includes orientational degrees of freedom, and therefore requires numerical techniques [60], which is computationally expensive. Hence a simple generalization of Steele's wall-potential given by Eq. (6.37) is useful, and was first proposed by Wall and Cleaver [60] for calamitic liquid crystals:

$$\begin{aligned} U_{i\mathrm{w}}(z,\theta_{i\mathrm{w}}) &= \alpha\epsilon_{\mathrm{w}}(\theta_{i\mathrm{w}})\frac{3}{\sqrt{10}(1-\chi^2)^{\nu/2}} \\ &\times\left[\frac{2}{15}\left(\frac{z-\sigma_{\mathrm{w}}(\theta_{i\mathrm{w}})+\sigma_0}{\sigma_0}\right)^{-9} - \left(\frac{z-\sigma_{\mathrm{w}}(\theta_{i\mathrm{w}})+\sigma_0}{\sigma_0}\right)^{-3}\right], \end{aligned} \tag{6.44}$$

with

$$\begin{aligned} \sigma_{\mathrm{w}}(\theta_{i\mathrm{w}}) &= \sigma_0[1-\chi\cos^2\theta_{i\mathrm{w}}]^{-\frac{1}{2}} \\ \varepsilon_{\mathrm{w}}(\theta_{i\mathrm{w}}) &= \varepsilon_0[1-\chi'\cos^2\theta_{i\mathrm{w}}]^{\mu}, \end{aligned} \tag{6.45}$$

where z is the distance between the particle and the wall, and $\theta_{i\mathrm{w}}$ is the angle between the disc axis and the normal to the wall. Furthermore, there are again energy- and shape-anisotropy functions similar to those occurring in the Gay-Berne

potential. The only new parameter is the scalar α, that governs the strength of the particle-substrate interaction.

A surface potential for discotic systems was proposed by Bellier-Castella et al. [55]:

$$\begin{aligned} U_{i\mathrm{w}}(z,\theta_{i\mathrm{w}}) &= \epsilon_{\mathrm{w}}(1+AP_2[\cos(\theta_{i\mathrm{w}})]) \\ &\quad \times\left[\frac{2}{15}\left(\frac{z-z_{\mathrm{shift}}(\theta_{i\mathrm{w}})}{\sigma_{\mathrm{ff}}}\right)^{-9}-\left(\frac{z-z_{\mathrm{shift}}(\theta_{i\mathrm{w}})}{\sigma_{\mathrm{ff}}}\right)^{-3}\right], \end{aligned} \tag{6.46}$$

where P_2 is the second Legendre polynomial and ε_{w} an energy parameter. This potential bears similarities to the Wall-Cleaver potential for calamitic mesogens. Two forms of z_{shift} are considered here. In case I $z^{\mathrm{I}}_{\mathrm{shift}}(\theta)$ is chosen to be zero, which implies a full factorization of the z and θ dependencies of the potential. In case II have

$$z^{\mathrm{II}}_{\mathrm{shift}}(\theta_{i\mathrm{w}}) = \frac{1}{2}\left[\sigma_0\left(1-\frac{2\chi}{1+\chi}\cos^2\theta_{i\mathrm{w}}\right)^{-\frac{1}{2}}-\sigma_{\mathrm{ff}}\right]. \tag{6.47}$$

Here we have an orientation-dependent shift that increases from zero for a face-on disc orientation up to a maximum value of $(\sigma_{\mathrm{ee}}-\sigma_{\mathrm{ff}})/2$ for an edge-on orientation. No significant difference between these two potentials was found [55]. The potential given by Eq. (6.46) has a minimum located at

$$z_{\mathrm{min}} = (2/5)^{1/6}\sigma_{\mathrm{ff}} + z_{\mathrm{shift}}(\theta_{i\mathrm{w}}), \tag{6.48}$$

and the corresponding value of the potential at an arbitrary fixed orientation is

$$U_{i\mathrm{w}}(\theta_{i\mathrm{w}}, z_{\mathrm{min}}) = -\epsilon_{\mathrm{w}}(10/9)^{1/2}(1+AP_2[\cos(\theta_{i\mathrm{w}})]). \tag{6.49}$$

The parameter A ranges from $-1/2$, favouring an edge-on orientation of the discs with respect to the surface, to 1, favouring a face-on orientation, both of which can be achieved experimentally [53].

As already mentioned, a potential function for particles confined in a cylindric geometry is not simple: even in the case of spherically symmetric Lennard-Jones particles, hypergeometric functions crop up; thus the complication and the computational cost become higher. The inclusion of orientational degrees of freedom for Gay-Berne systems makes the problem even more complicated, and it is useful to compare the surface potentials for the Lennard-Jones system given by Eqs. (6.37) and (6.38) in order to find a reasonable potenial for the anisotropic system in the cylindrical confinement. Of course, in Eq. (6.37) r_{iw} is replaced by $R-r_{\mathrm{ic}}$ to account for the geometry. Before following the physical intuition that the influence of the curvature should vanish when the radius of the cylinder exceeds a certain value, we first have a look at small radii, when the curvature should not be negligible. In Fig. 6.8 the cross-sections $U(x,0)$ of Steele's potential and the potential found by Jiang et al. are compared. In the left picture there is clearly a difference between Steele's and Jiang's potential, and a first possibility to adapt Steele's potential to the cylindric geometry is to increase the density of the wall: for a large curvature the Gay-Berne molecule is surrounded by more wall atoms than in the flat case. In

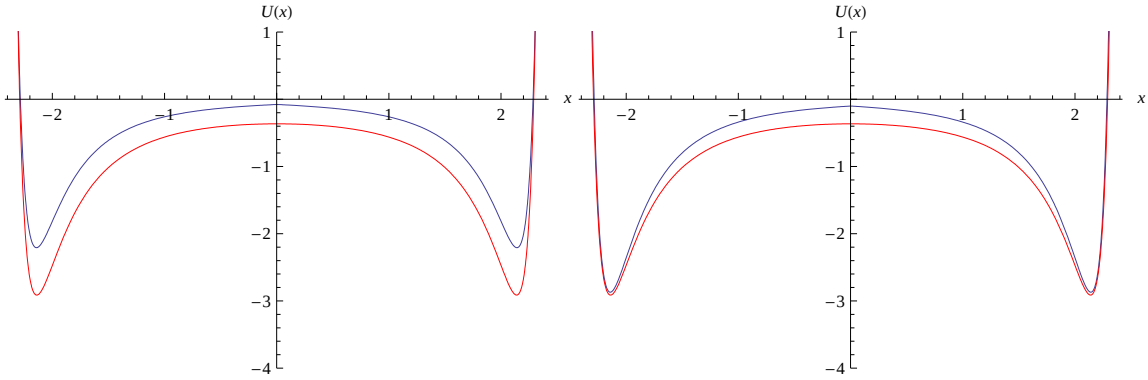

Figure 6.8: Cross sections of the potentials by Steele (blue) and Jiang et al. (red) for a cylinder with the radius $R = 3$. In the left picture the density of the wall is set to $\rho_w = 1$ for both potentials, whereas in the right picture the wall density for the Steele potential is increased to $\rho_w = 1.3$ to model the larger effective density due to the curvature of the wall.

the outer regions the well depths agree well, but in the middle of the cylinder the potential is overestimated.

Now we can study the difference of the two potentials depending on the cylinder radius, which is done in Fig. 6.9. As expected before, the difference vanishes if the radius gets large as compared to the dimensions of the particles. We shall carry out simulations for a radius of $R = 17.5$, the reason of which will be explained later; thus we can disregard the curvature of the wall in a good approximation, as indicated by Fig. 6.9.

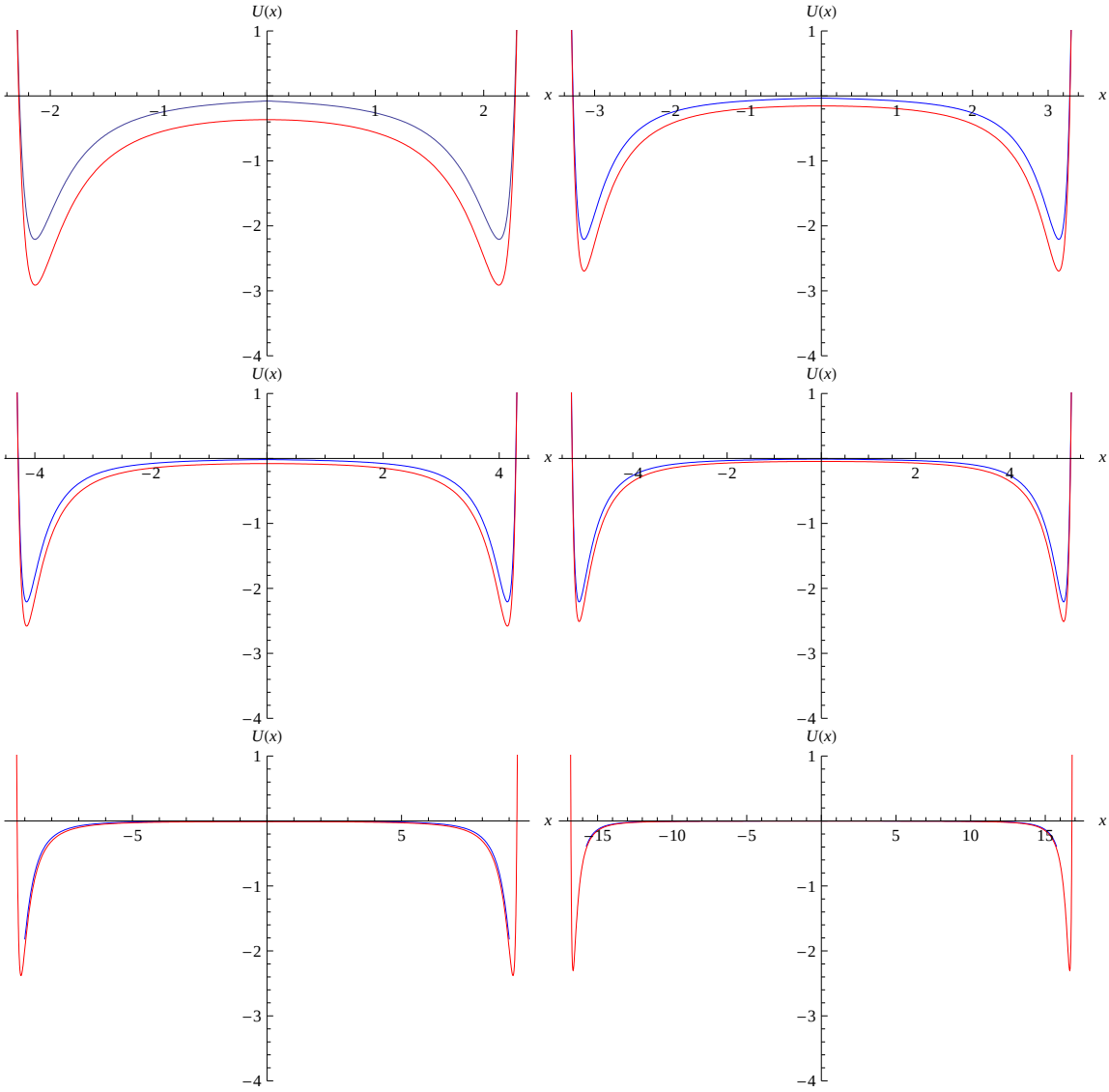

Figure 6.9: Cross-sections $U(r_{iw}))$ with $r_{iw} = |x|$ of the potentials by Steele (blue) and by Jiang et al. (red) for cylinder radii $R = 3$ (top left), $R = 4$ (top right), $R = 5$ (middle left), $R = 6$ (middle right), $R = 10$ (bottom left) and $R = 17.5$ (bottom right). For $R = 3$ there is a clear difference, that becomes smaller and smaller until it is not visible any more for $R = 17.5$.

The discussion of the cross-sections of the potentials for the cylindrically confined Lennard-Jones system shows that it is fair to model the surface-wall interaction for a Gay-Berne fluid confined in a nanopore with the Bellier-Castella potential Eq. (6.46), where $z = r_{iw} = R - r_{ic}$, yielding

$$U_{iw}(r_{ic}, \theta_{iw}) = \epsilon_w(1 + AP_2[\cos(\theta_{iw})]) \times \left[\frac{2}{15}\left(\frac{R - r_{ic} - r_{shift}(\theta_{iw})}{\sigma_{ff}}\right)^{-9} - \left(\frac{R - r_{ic} - r_{shift}(\theta_{iw})}{\sigma_{ff}}\right)^{-3}\right], \tag{6.50}$$

where r_{shift} has the shape (6.47). Fig. 6.10 shows cross-sections of this potential for fixed orientations with respect to the wall normal.

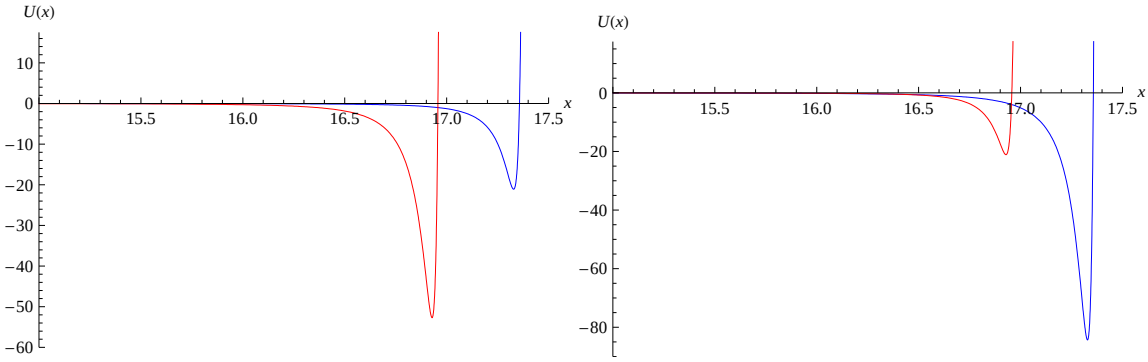

Figure 6.10: Cross-sections $U(r_{ic})$) with $r_{ic} = |x|$ of the potential given by Eq. (6.50) for a cylinder with radius $R = 17.5$, $\epsilon_w = 40$, and fixed angles $\theta_{iw} = 0$ (blue) and $\theta_{iw} = \pi/2$ (red). In the left picture edge-on anchoring is favoured ($A = -0.5$), in the right one face-on anchoring ($A = 1$).

6.5 Derivation of the forces and torques due to the wall

In this section the calculation of the forces and torques due to the influence of the cylindrical wall will be presented. Readers interested in details of the calculation of forces and torques resulting from anisotropic potentials might have a look at Ref. [65].

To find the forces and torques acting on particle i due to particle j, one has to consider the anisotropic potential $U_{ij} \equiv U_{ij}(\mathbf{r}_{ij}, \hat{\mathbf{e}}_i, \hat{\mathbf{e}}_j)$ as a function of the interparticle distance $\mathbf{r}_{ij}$ and the particle orientations $\hat{\mathbf{e}}_i, \hat{\mathbf{e}}_j$; the total force and torque acting on particle i is the sum of the contributions of all the other particles. Because of Newton's third law only $N(N-1)/2$ pairs must be evaluated. Actually the distance and the orientations enter the potential only in the form of their scalar products

$$c_i = \hat{\mathbf{r}}_{ij} \cdot \hat{\mathbf{e}}_i, \quad c_j = \hat{\mathbf{r}}_{ij} \cdot \hat{\mathbf{e}}_j, \quad c_{ij} = \hat{\mathbf{e}}_i \cdot \hat{\mathbf{e}}_j. \tag{6.51}$$

For the calculation of the contribution of the wall, the latter takes the role of particle j and the wall potential given by Eq. (6.50) can be regarded as a function $U_{iw} \equiv U_{iw}(r_{ic}, c_i)$, where $c_i = \hat{\mathbf{r}}_{ic} \cdot \hat{\mathbf{e}}_i = \cos(\theta_{iw})$. The calculation of the forces and torques can be simplified taking into account the translational symmetry with respect to the direction parallel to the cylinder axis: assuming that the z-axis of the coordinate system coincides with the cylinder axis, the origin can be chosen such that its z-component coincides with the z-component of the reference particle i. Then the difference vector $\mathbf{r}_{ic}$ can be identified with the particle's position $\mathbf{r}_i$ in this coordinate system and the forces acting on particle i due to the wall are

$$\begin{aligned} \mathbf{f} &= -\frac{\partial}{\partial \mathbf{r}_i} U_{iw} \\ &= -\frac{\partial U_{iw}}{\partial r_i} \hat{\mathbf{r}}_i - \frac{\partial U_{iw}}{\partial c_i} \left(\frac{\hat{\mathbf{e}}_i - c_i \hat{\mathbf{r}}_i}{r_i} \right). \end{aligned} \tag{6.52}$$

The torques acting on the particles due to the wall are

$$\boldsymbol{\tau}_i = \hat{\mathbf{e}}_i \times \mathbf{g}_i, \tag{6.53}$$

with the generalised forces (or "gorques") $\mathbf{g}_i$ defined by

$$\mathbf{g}_i = -\frac{\partial}{\partial \hat{\mathbf{e}}_i} U_{i\mathrm{w}} = -\frac{\partial U_{i\mathrm{w}}}{\partial c_i} \hat{\mathbf{r}}_i. \tag{6.54}$$

The partial derivatives needed in Eqs. (6.52) and (6.54) are readily evaluated. Defining a reduced distance as for the intermolecular Gay-Berne potential

$$\rho(r_{ic}, \theta_{i\mathrm{w}}) = \frac{R - r_i - r_{\mathrm{shift}}(\theta_{i\mathrm{w}})}{\sigma_{\mathrm{ff}}}, \tag{6.55}$$

one has

$$\begin{aligned}
\frac{\partial U_{i\mathrm{w}}}{\partial r_i} &= \frac{3\epsilon_{\mathrm{w}}}{\sigma_{\mathrm{ff}}}[1 + AP_2(c_i)] \left(\frac{2}{5}\rho^{-10} - \rho^{-4} \right) \\
\frac{\partial U_{i\mathrm{w}}}{\partial c_i} &= 3\epsilon_{\mathrm{w}} A c_i \left(\frac{2}{15}\rho^{-9} - \rho^{-3} \right) - \frac{\partial U_{i\mathrm{w}}}{\partial r_i} \sigma_{\mathrm{ff}} \frac{\partial \rho}{\partial c_i} \\
\frac{\partial \rho}{\partial c_i} &= -\frac{\sigma_0 c_i \chi}{\sigma_{\mathrm{ff}}(1+\chi)} \left(1 - \frac{2c_i^2 \chi}{1+\chi} \right).
\end{aligned} \tag{6.56}$$

6.6 Results

We simulated a discotic Gay-Berne mesogen confined in a cylindrical pore of radius $R = 17.5\sigma_0$. Reduced units [29] will be employed throughout this section. We used a velocity Verlet integrator in the NVT-ensemble realized with a Nosé-Hoover thermostat. The time step was $\Delta t = 0.0002$.Assuming that the molecular diameter σ_0 corresponds approximately to 1 nm, the pore diameter corresponds to the smaller one of those studied in the experiments [52], i.e. 35 nm and 400 nm. The computational cost of a larger diameter would be huge.

A face-on configuration near the wall was enforced setting by $A = 1$ in Eq. (6.50). We studied three different anchoring strengths $\epsilon_w = 14,\ 30$ and 40, as illustrated in Fig. 6.11; the lowest anchoring strength corresponds to the choice of Bellier-Castella [55].

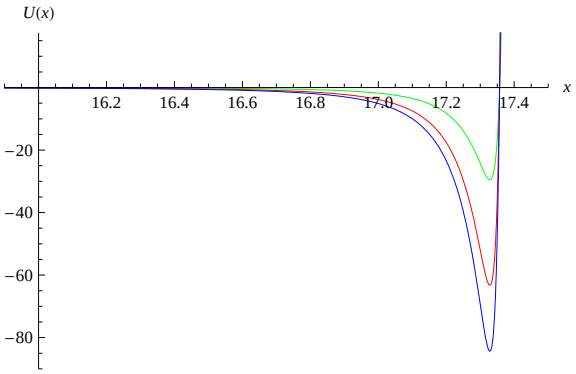

Figure 6.11: Cross-sections $U(r_{ic}))$ with $r_{ic} = |x|$ of the wall potential given by Eq. (6.50) for $\epsilon_w = 14$ (green), $\epsilon_w = 30$ (red) and $\epsilon_w = 40$ (blue) at a fixed homeotropic (face-on) orientation of the molecule at the wall ($\theta_{iw} = 1$), as favoured by the choice $A = 1$.

We started our simulation from a bulk nematic phase and threw away all the particles fulfilling the condition $x^2 + y^2 > r^2$, where r was chosen slightly smaller than the actual cylinder radius in order to allow the sample to expand, thus avoiding an initial bad overlap with the wall. In this way we first prepared configurations of 97 448 particles and then configurations of 584 688 particles by stacking 5 smaller configurations on each other. These big configurations resulted in a length of the cylinder ranging from $120\sigma_0$ to $300\sigma_0$, thus almost reaching the micrometer scale in the z-direction, as it is the case in the experiments. We started from a configuration at density $\rho = 2$ and temperature $T = 15$ and equilibrated over 100 000 time steps. Already at this low density and high temperature an influence of the wall can be noticed.

To detect this we analyzed radial density and order parameter profiles as well as the orientational density function. The radially dependent quantities are computed accumulating over all the particles located in a cylindric shell with the radial coordinate $r = \sqrt{x^2 + y^2}$ between r and $r + \Delta r$, and normalizing in an appropriate way. The density is normalized dividing by the volume $V = \pi z \Delta r(2r + \Delta r)$ of the

cylindric shell; the order parameter as defined in Eq. (6.3) is computed as

$$S(r) = \frac{1}{2n(r)} \sum_{i \in I} (3\mathbf{e}_i \cdot \mathbf{e}_i - 1)\,, \tag{6.57}$$

where $n(r)$ is the number of molecules lying between r and $r + \Delta r$, and the index set I consists of all i for which $r < \sqrt{x_i^2 + y_i^2} \leq r + \Delta r$. Due to the large simulated number of particles the statistics is good enough if the average is taken over space only at a single time.

Figs. 6.12 and 6.13 show radial density, order parameter profiles and orientational distribution functions for the system in equilibrium at $\rho = 2$ and $T = 15$.

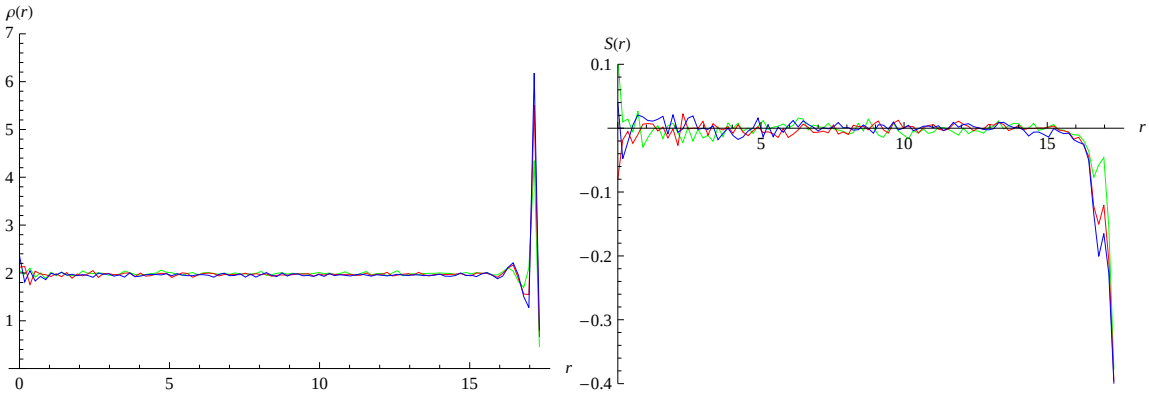

Figure 6.12: Radially dependent density (left) and order parameter (right) for the anchoring strenghts $\epsilon_w = 14$ (green), $\epsilon_w = 30$ (red) and $\epsilon_w = 40$ (blue).

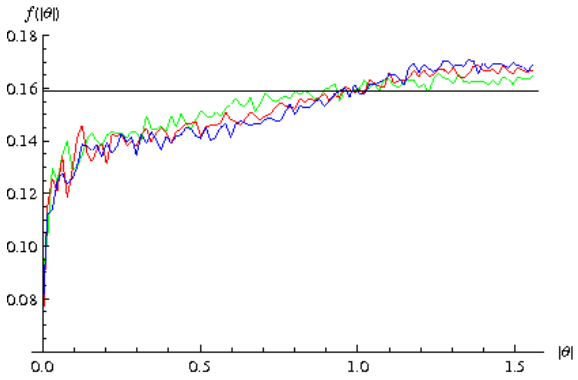

Figure 6.13: Orientational distribution for the anchoring strengths $\epsilon_w = 14$ (green), $\epsilon_w = 30$ (red) and $\epsilon_w = 40$ (blue) and the uniform distribution (black).

For the orientational distribution (or, more properly, the orientational density function), we have assumed invariance with respect to the equatorial angle ϕ due to the cylindric symmetry of the problem, and hence it is a function of the polar angle θ alone. Due to the invariance with respect to rotations by π it is also symmetric around $\pi/2$, and only the modulus of the polar angle $|\theta|$ between 0 and $\pi/2$ has to be considered.

For $\epsilon_w = 14$, which corresponds to the green curves, the influence of the wall is smaller than for $\epsilon_w = 30$ and $\epsilon_w = 40$: the orientational distribution is closer to the

uniform distribution and the radial order parameter increases faster with decreasing radial coordinate r; near the wall we have $S \approx -0.4$ and in the inner regions of the cylinder S fluctuates around zero, corresponding to an isotropic phase, at least as an average over z.

We compressed and cooled sequentially from $(\rho, T) = (2, 15)$ to (2.5, 13), (3, 11) and (3.5, 9), equilibrating samples over 100 000 time steps. Then we further compressed and cooled to reach the state (4, 7), and equilibrated the samples over a longer period to check whether the structure was still changing. For $\epsilon_w = 40$ we monitored the structure over more than 2 million time steps, and observed no significant change in the structures after some 100 000 steps, as Fig. 6.14 shows. For visualization we have used our own open source program QMGA [66], which is available under the GNU Public Licence on the website http://qmga.sourceforge.net.

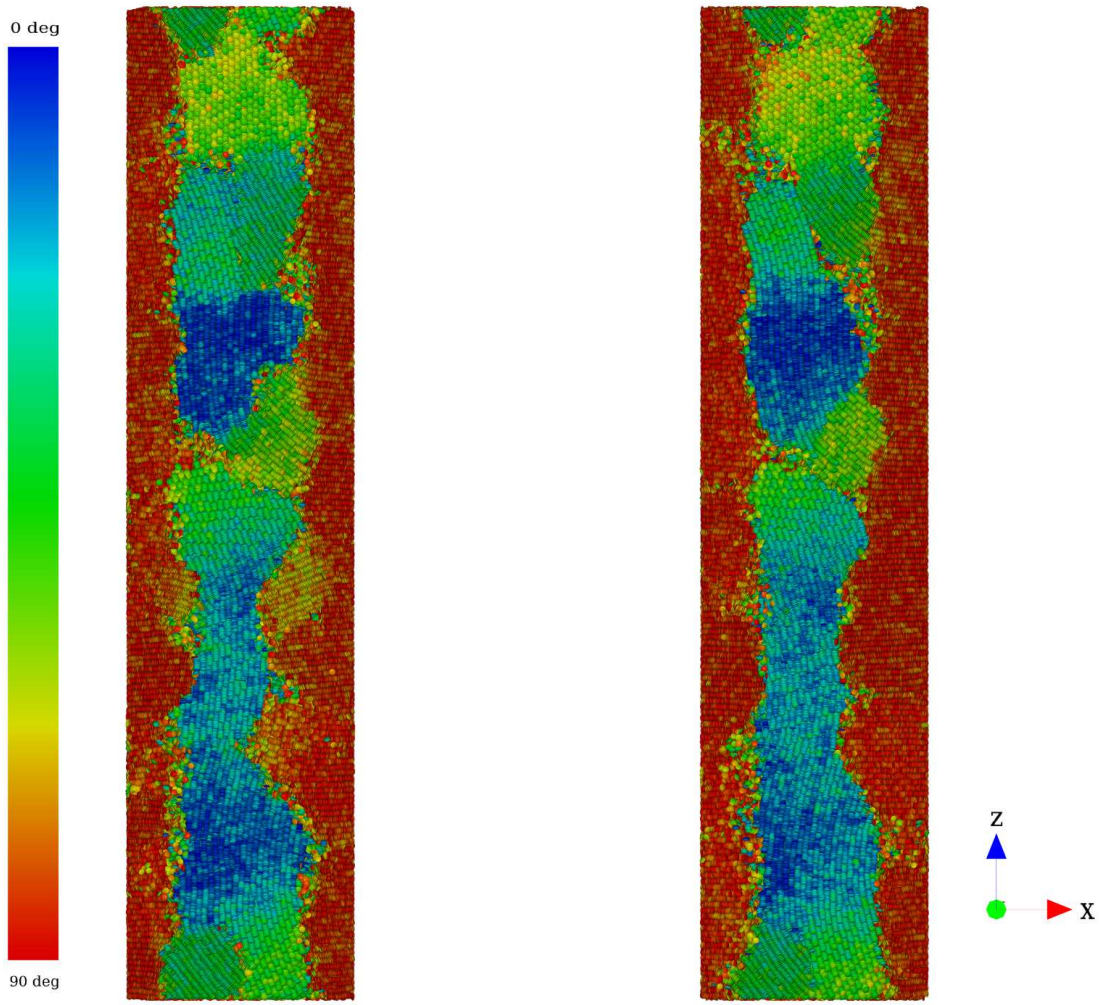

Figure 6.14: Cross sections of configurations taken from a run at $\rho = 4$ and $T = 7$ for the anchoring strength $\epsilon_w = 40$. The left snapshot is taken at time step 500 000, and the right one after more than two million time steps. The structures do not change significantly. The molecules are coloured according to the colour map on the left, where blue corresponds to an orientation parallel to the cylinder axis, and red to a perpendicular one.

We decided to further compress and cool in order to show that structures as conjectured by Stillings et al. in their experiments actually occur: homeotropic

(face-on) alignment close to the wall, and a sudden switch to an alignment parallel to the cylinder axis in the inner regions. Since the structures were stable after some 100 000 steps and $(\rho, T) = (4, 7)$ was not our final state, we did not simulate this state for as many time steps with the other two anchoring strengths as with $\epsilon_w = 40$ (about 800 000 steps for $\epsilon_w = 30$ and 300 000 for $\epsilon_w = 14$). We now compare the radial density and order parameter profiles for the three anchoring strengths at the state $(\rho, T) = (5, 3)$ in Figs. 6.15 and 6.16.

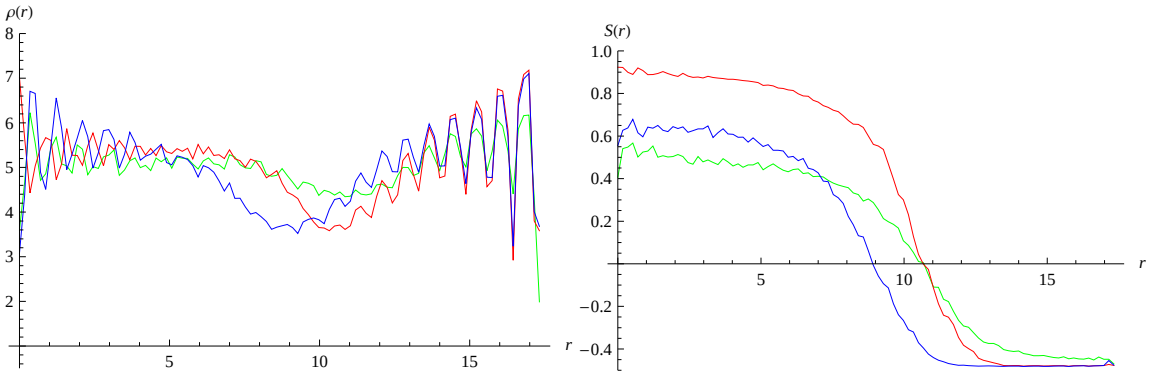

Figure 6.15: Radially dependent density (left) and order parameter (right) for different anchoring strenghts. Again the green curves refer to $\epsilon_w = 14$, the red curves to $\epsilon_w = 30$ and the blue curves to $\epsilon_w = 40$.

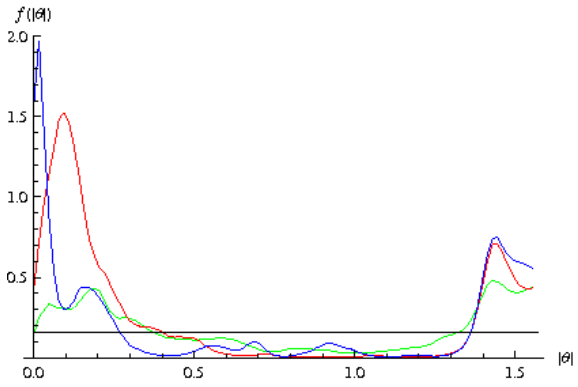

Figure 6.16: Orientational distribution for the anchoring strengths $\epsilon_w = 14$ (green), $\epsilon_w = 30$ (red) and $\epsilon_w = 40$ (blue) and the uniform distribution (black).

The density profiles show a regular pattern, where fluctuations around the average density are large near the wall, and small in the middle of the cylinder, originating respectively from layered structures in the vicinity of the wall, and columnar domains in the middle. For intermediate values of the radial coordinate r there are minima of the density depending on the anchoring strengths, and we notice that these minima correspond to the zero crossings of the order parameters, which can be explained by the fact that the packing in the isotropic phase is not as dense as in nematic or columnar phases, where the excluded volume is smaller. For $\epsilon_w = 14$ the alignment of the molecules near the wall with the disc normals pointing perpendicular to the wall surface is less pronounced than in the case of the two other anchoring strengths, corresponding to a less stable state imposed by the potential;

the green curve in the right picture of Fig. 6.15 does not approach the lowest possible value $S = -0.5$ as closely as the other two curves. Furthermore the influence of the wall reaches over a larger length scale for stronger anchorings, however the increase of the order parameter as the distance from the wall gets larger is steepest in the case $\epsilon_w = 30$ (red curve), and the degree of alignment parallel to the cylinder axis is the highest of all the three anchorings. Fig. 6.17 further clarifies the structures which are consistent with the orientational distribution function shown in Fig. 6.16, where the peaks correspond to the domains seen in the graphic visualization. Three dimensional plots of the orientational distributions $f(r, |\theta|)$ are shown in Fig. 6.18.

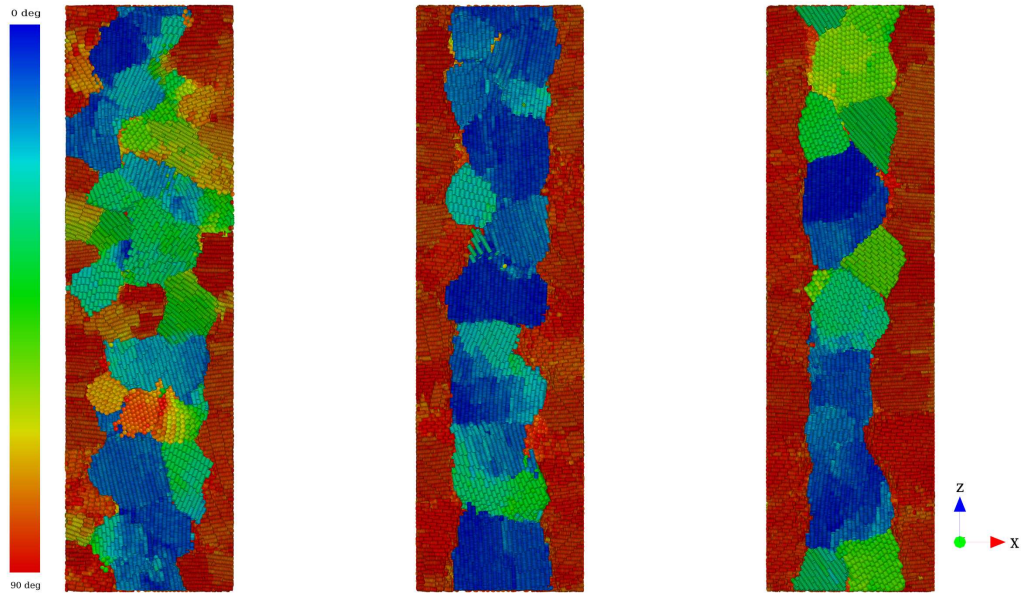

Figure 6.17: Cross sections of configurations obtained after compressing from $\rho = 4$ to $\rho = 5$ and cooling from $T = 7$ to $T = 3$ after about half a million time steps for $\epsilon_w = 14$ (left), 30 (middle) and 40 (right).

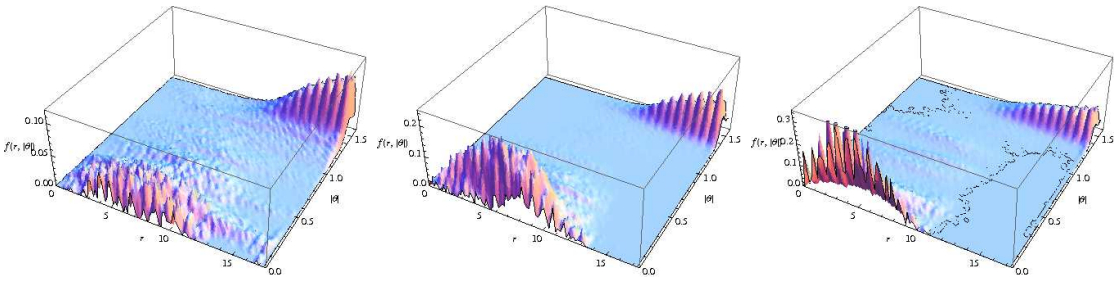

Figure 6.18: Radially dependent orientation distributions $f(r, |\theta|)$ corresponding to the pictures in Fig. 6.17, where the anchoring strengths are in the same order as in the previous visualizations.

The observed sructures are not unique; depending on the initial conditions and the thermodynamic path along which the system has been brought to its final state other structures can be observed. In the experiments too, the structures depend e.g. on the cooling rate. In order to point out the difference, we started again from the equilibrated sample at $\rho = 2$ and $T = 15$, but first reduced the temperature to $T = 7$

and equilibrated for more than 1 million time steps, before sequentially compressing to $\rho = 4$ while keeping the temperature constant. Thereafter we compressed and cooled again, until the final state $(\varrho, T) = (5, 3)$ of the first path was reached. The molecular graphics and the orientational distribution in Fig. 6.19 show the resulting structures.

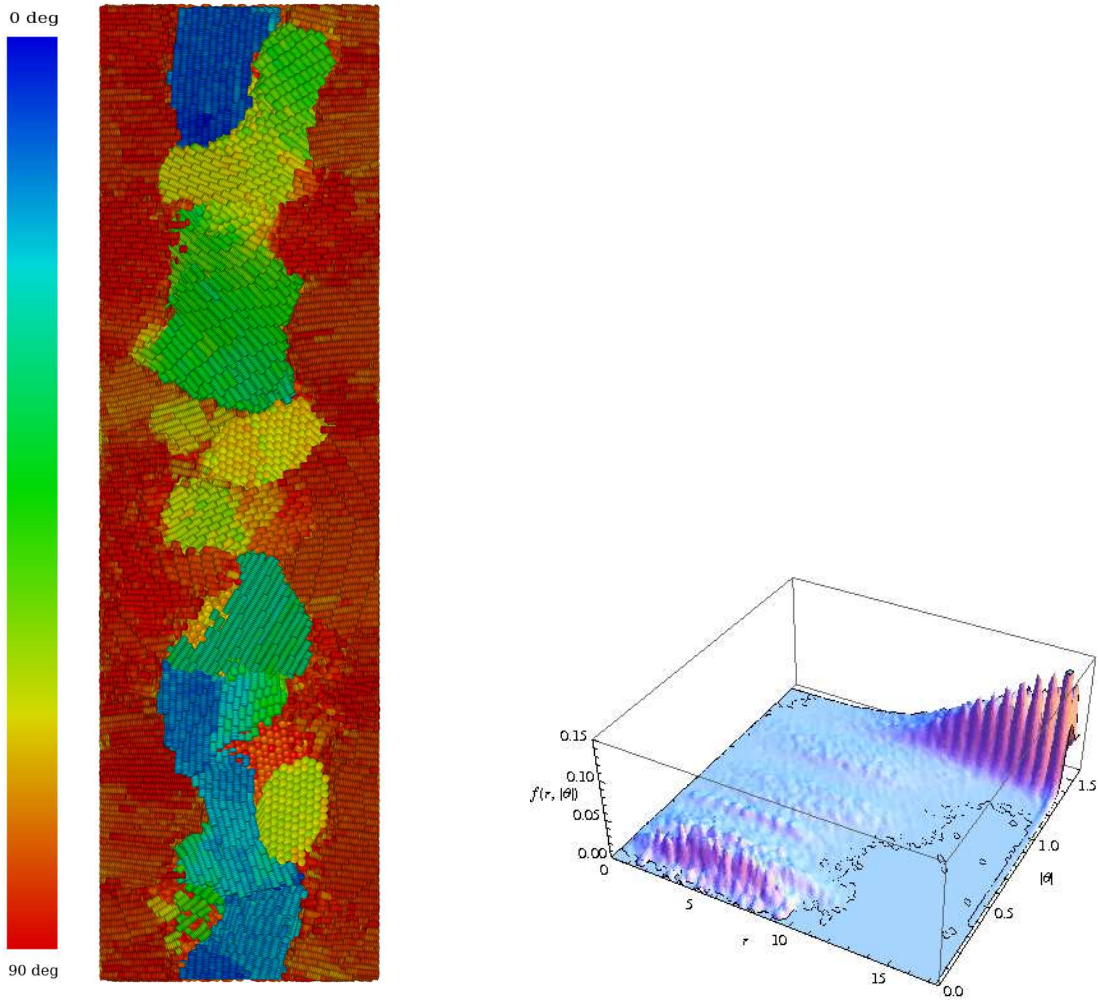

Figure 6.19: Visualization of the cross section of the end configuration obtained if the system is brought to the state $\rho = 5$ and $T = 3$ along an alternative thermodynamic path (left) and the corresponding orientational distribution $f(r, |\theta|)$.

The perpendicular alignment of the disc normals relative to the wall in the end configuration obtained via the second path is extended to more central regions as compared to the first path, which can already be recognized in the visualization. This impression is confirmed by Fig. 6.20, where radially dependent densities and order parameters are compared for the two paths. The change of the order parameter from negative values in regions close to the wall to positive values in the middle takes place at a smaller radial coordinate for the second path (red curve), and the maximum value of the order parameter is smaller as compared to the structures resulting from the first path (blue curve). The different peaks in the orientational distributions $f(r, |\theta|)$ and $f(r)$ shown in the right part of Fig. 6.19 and in the left part of Fig. 6.21 are again consistent with the domains seen in the visualization.

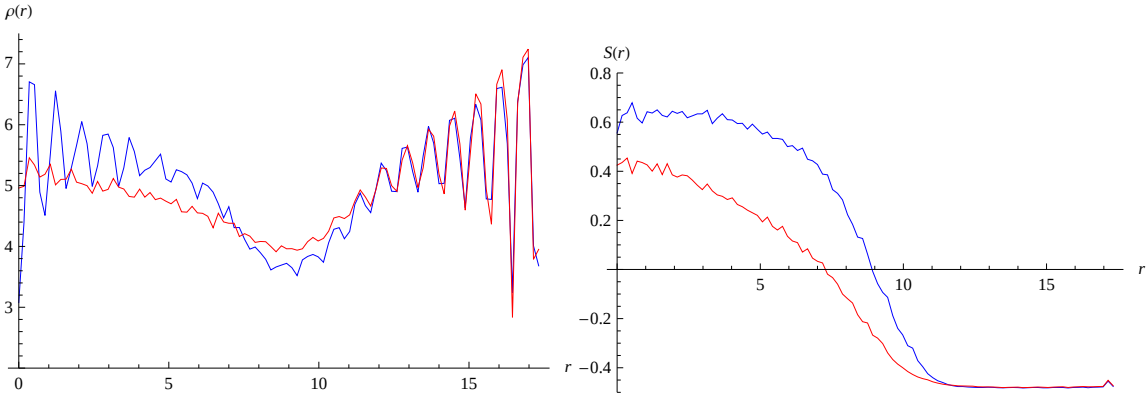

Figure 6.20: Radially dependent density (left) and order parameter (right) for the end configurations at $\rho = 5$ and $T = 3$ resulting from different thermodynamic paths. The blue curves refer to the first path described in the text and the red curves to the second.

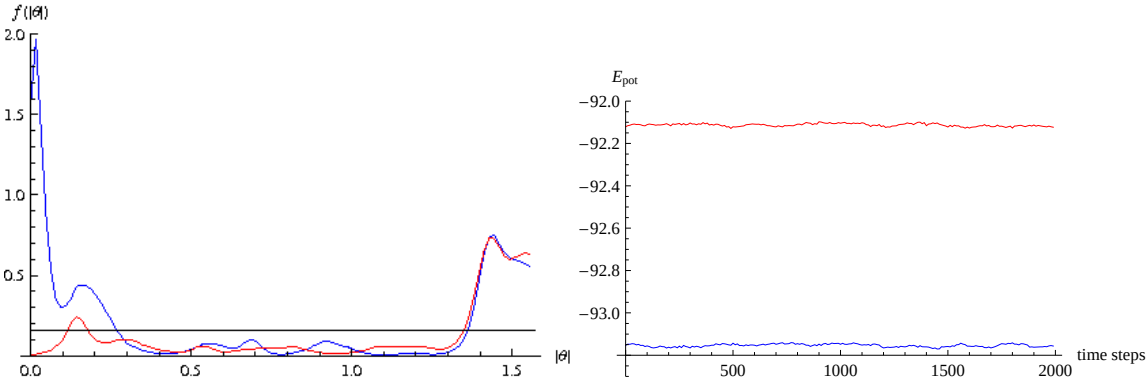

Figure 6.21: Orientational distribution (left) and potential energy per particle (right) for the first (blue) and the second (red) path.

We have shown that the obtained structures depend on the thermodynamic history of the system; one could claim that, regarding the local director a stochastic process in time, the latter is non-Markovian and thus ergodicity is broken. Trying to interprete the memory of the system in a qualitative way, we can extract some information about mechanisms of pattern formation. The temperature quench leads to an orientational relaxation of the molecules near the wall, where the face-on orientation is preferentially adopted due to the deeper minimum of the wall potential compared to other orientations. The next layers tend to align parallel to the molecules at the wall, because the face-to-face configuration is favoured and the particles are still in the range of the attractive wall potential. This mechanism alone would lead to a perfect perpendicular alignment of the disc normals throughout the pore leading to a topological defect in its middle; hovever, in the configurations obtained via both paths there is a tendency of the order parameter to become positive as the distance from the wall increases. We believe that packing effects are responsible for the switch: in the limit case of a cylinder with a diameter equal to that of a molecule, a perpendicular orientation of the disc normals leads to a density five times ($\equiv 1/\kappa$) higher than for a stack of parallel molecules, which, in accordance with Onsager's theory, corresponds to a lower configurational entropy.

The desire to control the alignment direction over macroscopic scales in order to achieve e.g. a good electric conductivity along the column axis leads to the question which structures are more stable. In a canonical ensemble the free energy

$$F = U - TS \tag{6.58}$$

has a minimum in thermodynamic equilibrium, however the wealth of structures seen in the simulations indicates a complex free energy landscape. To compare the stability of the structures resulting from the two thermodynamic paths in a qualitative way, we shall have a look at the free energy per particle. The internal energy is the sum of the kinetic energy and the potential energy. The former is equal for both systems; in a canonical ensemble it only depends on the temperature. The potential energy per particle of the two systems is shown in the right plot of Fig. 6.21 and is significantly lower for the first path (blue curve). The quantity that remains to be analyzed is the entropy of the system, which consists of configurational and rotational contributions. This is hard to calculate explicitly, but, consistently with Onsager's approach, its qualitative behaviour can be discussed. As indicated by the left plot in Fig. 6.20, the packing in the middle of the cylinder and hence the configurational entropy is significantly denser for the first path, whereas in the outer regions the densities are in comparable ranges. The orientational part of the entropy is proportional to the amount of orientational states, which is expressed by the term $\int f \log(4\pi f)\, d\Omega$ in the Onsager theory, where $f \equiv f(\theta)$ is the orientational distribution depending the polar angle. Since we considered only the modulus of the polar angle, the density function f should be multiplied with 2π inside the logarithm for our calculations. At this point it is worth observing the analogy to Boltzmann's H given by Eq. (4.1),

$$H = \int_\mu f \log f dv_\mu, \tag{6.59}$$

where the density function f is a function of the generalized positions and momenta, and hence the integration goes over the complete μ-space. The density function used in the definition of Boltzmann's H is a joint probability density, and finding the marginal probability density $f(\theta)$ is not trivial, since the complete density function does not necessarily factorize and coupling terms have to be taken into account. However, the above discussion of potential energy, local density, as well as the dicussion of the rotational term allow a qualitative understanding of the problem. Restricting to the information given by the orientational states and thus choosing the coarse-graining of μ-space such that, corresponding to the symmetry of the system, only the modulus of the polar angle $|\theta|$ distinguishes one state from the other, the transformation into spherical coordinates transforms the volume element into the infinitesimal solid angle $d\Omega$, since the radial coordinate is constantly equal to one. Finally integration over the equatorial angle delivers the factor 2π.

The integral giving the rotational part of the entropy becomes a sum if the modulus of the polar angle is discretized. Dividing the interval $(0, \pi/2]$ into k subintervals,

we obtain

$$\begin{aligned}\int f\log(2\pi f)d\Omega &= 2\pi\int_0^{\pi/2} f\log(2\pi f)\sin(|\theta|)\,d|\theta| \\ &\approx 2\pi\sum_{i=1}^{k} f(\theta_i)\log(2\pi f(\theta_i))\sin(\theta_i)\Delta|\theta| \\ &= \sum_{i=1}^{k}\frac{n_i}{N}\log\left[\frac{n_i}{N\sin(i\Delta|\theta|)\Delta|\theta|}\right], \end{aligned} \tag{6.60}$$

where $\theta_i = i\Delta|\theta|$ is measured in steps of $\Delta|\theta|$, N is the total number of particles, and n_i is the number of particles with $\theta_{i-1} \leq |\theta| < \theta_i$. This quantity can be implemented straightforwardly in a computer code, and the numerical values within a precision of two digits are 0.85 for the first path and 0.76 for the second, which means that the configuration resulting from the first path would have a lower free energy than the ones resulting from the second path. As illustrated in Fig. 6.21, the mean values for the potential energies are around -93.1 for the first path and -92.1 for the second, and the difference of the potential energies is one order of magnitude larger than for the two rotational contributions. Additionally the molecules are packed significantly denser for the first path, as discussed above. According to these considerations it seems that the configuration obtained by choosing the first path is more stable than the one resulting from the second path.

6.7 Discussion

When confining discotic liquid crystals into a cylindric geometry a wealth of structures can be observed both experimentally as well as in simulations. The understanding of this pattern formation is of great practical interest but highly nontrivial, since it depends on many parameters like the cylinder radius, the anchoring strength and the preferential orientation of the molecules near the wall, but also on dynamical features like the thermal history of the system. Reality is complicated to understand. To consider atomic degrees of freedom or even the chemical structure for many particles would be both conceptionally and computationally a tremendous task. Therefore we restrict to a simpler model, the Gay-Berne model, to check whether the most important characteristics of the structures are reproduced quantitaviely when keeping only essential features of molecular interactions. We have simulated a discotic Gay-Berne mesogen to do this and have found an agreement with experimental data. The main result is the tendency of the molecules to orient themselves parallel to the cylinder axis in the middle of the pore, surrounded by a shell of molecules with perpendicular alignment, which is due to the face-on anchoring imposed by the wall potential. The thickness of the shell depends on the depth of the wall potential. Depending on the thermal history of the system different structures can be observed, however a configuration with molecules aligned along the pore axis in the middle seems more stable than a less ordered one. We believe that this is due to packing reasons.

Many things have to be done in the future before technical applications of these systems can be achieved. The constantly inhcreasing computer power will make it possible to simulate pores with larger diameters, and hence the radius dependence

of the patterns can be studied over a wide scale. This may be one of our fourthcoming projects. Finding potentials with more detail, though not at full atomic level, for both the intermolecular and molecule-substrate interactions in order to be able to better compare simulations with experiments will also be a route to follow. Finally it is important to consider dynamical features, in order to be able to describe phenomena like e.g. wetting, which can have a major influence on the equilibrium configurations. Systems like the one studied are also suited for investigating phase ordering or domain growth kinetics, which can conveniently be detected in simulations.

Chapter 7

First passage times in complex systems

7.1 Introduction

In the theory of stochastic processes, the first passage time is defined as the time when a certain condition is fulfilled by the random variable of interest for the first time and is, of course, a random variable itself. In mathematics books a standard example of a first passage time problem is the decision of an investor to sell a stock whenever its fluctuating price leaves a certain region. However, first passage times play an important role also in chemical physics; early examples are given by models describing the dissociation of diatomic molecules as a first passage time problem, where dissociation occurs if a certain critical energy level is reached through collisions [67, 68, 69]. A view on diffusion in fluids based on first passage times has been proposed by Munakata [70], where self-diffusion is measured via the first passage time with respect to a boundary marked by a sphere centered at the original position of a labeled particle. Problems like neuron dynamics, self-organized criticality or dynamics of spin systems can be viewed as first passage processes in one dimension [71]. The first passage problem is closely connected to persistence, which is the probability that a random variable does not leave a certain region up to a certain time, i.e. the complementary event to a first passage at the same time. The problem of persistence in spatially extended nonequilibrium systems has attracted great interest both theoretically and experimentally, see [72] and references included therein, where persistence is defined as the probability that for an arbitrary nonequilibrium field $\boldsymbol{\phi}(\mathbf{r}, t)$ the quantity $\boldsymbol{\phi}(\mathbf{r}, t) - \langle \boldsymbol{\phi}(\mathbf{r}, t) \rangle$ does not change sign. The nonequilibrium field can also be a scalar or tensorial order parameter field. Yurke et al. [73] have measured the probability that the local order parameter in a twisted nematic liquid crystal system has not switched its state up to a time t. Persistence phenomena have also been studied in the context of diffusion fields [74], reaction-diffusion systems [75] and phase-ordering dynamics [76, 77]. All these systems share the characteristic property that persistence, and hence also the first passage time distribution, follows a power-law with some non-trivial exponent. However, as far as we are aware, the reference point with respect to which persistence was measured has always been the zero level. In this work we shall consider the first passage or first exit problem with respect to a certain level b for a stochastic process that may not be able to cross the origin, depending on the nature of the boundary at zero. In the following, we shall

introduce the model that we wish to analyze and explain its physical relevance.

7.2 The model

Our model can be described by the Itô stochastic differential equation

$$dX_t = \frac{nD}{X_t}\,dt + \sqrt{2D}\,dW_t, \tag{7.1}$$

where W_t is the Wiener process with zero mean

$$\langle W_t \rangle = 0, \tag{7.2}$$

and the autocorrelation function

$$\langle W_t W_{t'} \rangle = \min(t, t'). \tag{7.3}$$

D is the diffusion coefficient, and hence a positive real number; n is also a real number, the different ranges of which will be discussed later. Intuitively one might think that the stochastic process cannot cross the origin for a nonzero n: due to the singularity at $x = 0$ it should be bounded to the interval $(0, \infty)$ or $(-\infty, 0)$, depending on whether the initial value x_0 of the process is positive or negative. As we shall see later, this is only the case for a certain range of n.

Eq. (7.1) is a special case of different types of stochastic processes. On the one hand it is a special Rayleigh process that is widely employed in physics, economics and finance, see Ref. [78] and references included therein. It reads

$$dX_t = \left(\frac{a}{X_t} + bX_t\right)\,dt + \sigma\,dW_t, \tag{7.4}$$

where a and b are some constants. Clearly, setting $\sigma = \sqrt{2D}$, $a = nD$ and $b = 0$ reproduces Eq. (7.1). On the other hand our process can be mapped onto the Bessel process

$$dY_t = a\,dt + b\sqrt{Y_t}\,dW_t, \tag{7.5}$$

which can e.g. be used to generalize the Black-Scholes option-pricing model [79]. The mapping is done via the transformation $Y_t = X_t^2$: multiplying Eq. (7.1) with X_t and using Itô's lemma, one recovers Eq. (7.5) with $a = 2D(n+1)$ and $b = \sqrt{8D}$, where we have assumed $Y_t \geq 0$.

7.3 Physical motivation

The physical context in which the relevance of Eq. (7.1) arises will now be explained starting from generic considerations and then proceeding further with specific physical problems. In Ref. [80] Godrèche and Luck introduced a classification of stochastic processes into a group with "narrow" distributions, where all moments are finite, and "broad" distributions, where densities exhibit a power-law decay, and hence only a finite number of moments converge. Then the probability density functions of the persistence therewith also of the first passage time will respectively decay either faster than any power-law or algebraically, depending on the nature of the

process imposed by its distribution. The Wiener process imposes a density $f(t)$ with a tail behaving as $t^{-3/2}$ for the first passage problem with respect to a level b: to mention just one elegant way to compute it with respect to the process defined by Eq. (7.1) for $n = 0$, a simple scaling argument [81] delivers

$$f(t) = \frac{|b - x_0| t^{-\frac{3}{2}}}{\sqrt{4\pi D}} e^{-\frac{(b-x_0)^2}{4Dt}}. \tag{7.6}$$

In the case of a nonzero drift the situation is not so clear any more; the symmetry of the problem is broken and the first passage time also depends on the relative position of the starting point of the process with respect to the level of interest.

Eq. (7.1) appears in various physical, chemical and biological problems. The motion of atoms in a one-dimensional optical lattice formed by two counterpropagating laser beams with linear perpendicular polarization can be studied by a similar equation in the high momentum region [82], where the momentum takes the role of the stochastic variable x. The Barkhausen noise can be described phenomenologically by a model where the domain wall velocity as a function of the magnetization is also described by a similar Langevin equation if the demagnetizing factor is neglected [83, 84]. The magnetization takes the role of time.

Fogedby and Metzler, the former of which had already analyzed the generic Langevin equation before [85, 86], have applied the model for studying the variable size of a DNA "bubble" [87], which emerges when at a certain temperature hydrogen bonds connecting base pairs from the opposite strands of the double helix are broken. The bubble size is measured by the number of broken bonds; in a continuum limit the discrete number of broken bonds can be replaced by a continuous variable x and, according to the Poland-Scheraga model [88], the free energy of the system can be approximated for small bubble sizes as

$$\mathcal{F} \simeq c k_{\mathrm{B}} T \log x, \tag{7.7}$$

where c is a positive constant. Equilibrium is reached for a minimum of the free energy and the dynamics follows the Langevin equation

$$\frac{dx}{dt} = -D \frac{d\mathcal{F}}{dx} + \xi(t), \tag{7.8}$$

where $\xi(t)$ is the thermal noise, which is assumed to be Gaussian with the autocorrelation function $\langle \xi(t)\xi(t') \rangle = 2D k_{\mathrm{B}} T \delta(t - t')$. A similar model can be employed when studying the translocation of a polymer through a pore, where the number of monomers on one side is chosen as the "translocation coordinate" [89].

An interesting application of the model was found by Bray [90], who showed that persistence and nonequilibrium critical dynamics are related in the context of the two-dimensional XY-model with non-conserved order parameter, where the critical temperature is the temperature T_{KT} of the Kosterlitz-Thouless phase transition. The dynamics of a vortex-antivortex pair can be mapped to a one-dimensional Langevin equation of the shape of Eq. (7.1) by a series of transformations.

It is impossible for us to discuss all the publications dealing with similar models; too many of them exist, and therefore we shall only briefly mention three of them [91, 92, 93].

7.4 Simulation method

We have used the Euler-Maruyama method [94] to simulate the process governed by the Itô stochastic differential equation (7.1). A generic equation of the shape

$$dX_t = \mu(t, X_t)\, dt + \sigma(t, X_t)\, dW_t \tag{7.9}$$

can be integrated between two instants of time t_n and t_{n+1} with $t_n < t_{n+1}$ giving

$$X_{t_{n+1}} = X_n + \int_{t_n}^{t_{n+1}} \mu(t_s, X_s)\, ds + \int_{t_n}^{t_{n+1}} \sigma(t_s, X_s)\, dW_s. \tag{7.10}$$

The approximations

$$\begin{aligned} \mu(t_s, X_s) &\approx \mu(t_n, X_n) \\ \sigma(t_s, X_s) &\approx \sigma(t_n, X_n) \end{aligned} \tag{7.11}$$

yield the Euler-Maruyama method

$$X_{t_{n+1}} = X_{t_n} + \mu(t_n, X_n)\Delta t + \sigma(t_n, X_n)\Delta W_n, \tag{7.12}$$

where $\Delta t = t_{n+1} - t_n$, and $\Delta W_n = W_{t_{n+1}} - W_{t_n}$. Since the random variable ΔW_n is Gaussian with probability density

$$p(w) = \frac{1}{\sqrt{2\pi\Delta t}} \exp\left(-\frac{w^2}{2\Delta t}\right), \tag{7.13}$$

Eq. (7.12) can be implemented straightforwardly in code (we used C++).

However, measuring the first passage time with respect to a certain level needs a further refinement, since there is a finite hitting probability during each discretized time interval Δt, and thus the first passage time is overestimated. An analytic expression for the probability that the process hits the level b during a discretization interval Δt was found by Mannella [95]. If we introduce the abreviations $\mu_{t_i} = \mu(X_{t_i}, t_i)$, $\mu_b = \mu(b, t)$ and $\mu_b' = \partial\mu(x,t)/\partial x|_{x=b}$, the hitting probability reads

$$P(\text{hit}) = \exp\left\{-\frac{\mu_b'}{2D\left(e^{2\mu_b'\Delta t} - 1\right)}\left(X_{t_{n+1}} - b + (X_{t_n} - b)e^{\mu_b'\Delta t} - \frac{\mu_b}{\mu_b'}\right)^2 + \frac{1}{4D\Delta t}\left[X_{t_{n+1}} - \left(X_{t_n} + \frac{\mu_{t_n} + \mu_{t_{n+1}}}{2}\Delta t\right)\right]^2\right\}.$$

We can now summarize the simulation algorithm. We draw a Gaussian random number using e.g. the Box-Muller method and propagate the process by a time step Δt. Then we check for missed hits in the discretization interval by drawing a uniformly distributed random number between zero and one, and accepting the hitting hypothesis if the hitting probability is larger than the drawn random number. If the latter is the case the process is terminated. The second terminating condition for the process is fulfilled if the propagated value exceeds the level b for the first time. In both cases the first passage time is set to t_n, i.e. the value before the propagation.

In some cases a further refinement of the algorithm is possible. We will discuss this later, because some knowledge of the nature of the process is required for this purpose.

7.5 Theory and simulation results

In the following two subsections the theory for the computation of the first passage time probability density will be developed. After discussing the solution of the Fokker-Planck equation corresponding to Eq. (7.1) and classifying the nature of the boundaries, we compute the first-passage time probability density analytically and compare the results with the simulations.

7.5.1 Classification of the boundaries

The quantity we are interested in is the first passage time with respect to a certain level b, where we assume without loss of generality that the initial value x satisfies $0 < x < b$, because the case $b < x < 0$ is symmetric to the former one. The stochastic process can be viewed as a particle in a logarithmic potential driven by Gaussian white noise. In order to compute the first passage time probability density, the boundaries of the process must be found and classified. Clearly, for a mathematical reason, namely because we intend to measure the first passage time, the upper limit of the process is the artificially set absorbing boundary $x = b$. The identification and classification of the lower boundary requires some more analysis. We shall first analyze the heuristic argumentation adopted by Bray in Ref. [90] and then apply a more rigorous approach, which is necessary for a proper understanding of the problem.

Heuristic classification

The Fokker-Planck equation corresponding to the Itô stochastic differential equation (7.1) is

$$\frac{\partial p(x,t)}{\partial t} = -\frac{\partial}{\partial x}\left(\frac{nD}{x}p(x,t)\right) + D\frac{\partial^2 p(x,t)}{\partial x^2}. \tag{7.14}$$

Using the separation ansatz

$$p(x,t) = x^{\frac{1+n}{2}} R_k(x) e^{-Dk^2 t} \tag{7.15}$$

as done in Ref. [90], one gets

$$\frac{d^2 R_k}{dx^2} + \frac{1}{x}\frac{dR_k}{dx} + \left(k^2 - \frac{\nu^2}{x^2}\right) R_k = 0, \tag{7.16}$$

with

$$\nu = \frac{1-n}{2}. \tag{7.17}$$

The Bessel functions of the first kind $J_\nu(kx)$ and of the second kind $Y_\nu(kx)$ are two linearly independent solutions of Eq. (7.16), therefore the general solution of the Fokker-Planck equation (7.14) is

$$p_\nu(x,t) = x^{1-\nu} \int_0^\infty \left[A(k)J_\nu(kx) + B(k)Y_\nu(kx)\right] \exp(-Dk^2 t)\, dk. \tag{7.18}$$

For non-integer ν the Bessel functions of the first kind $J_\nu(kx)$ and $J_{-\nu}(kx)$ are linearly independent, and in the general solution the Bessel functions of the second

kind Y_ν can be replaced by $J_{-\nu}$. In order to find and classify the lower boundary of our problem, we consider the probability current

$$j(x) = D\left(\frac{n}{x}p(x) - \frac{\partial p(x)}{\partial x}\right), \tag{7.19}$$

and analyze its behaviour as the singular point $x = 0$ is approached. Considering the case $\nu \notin \mathbb{Z}$ we regard the contributions of the two terms in Eq. (7.18) separately, and call the contribution of the first term j_ν and of the second term $j_{-\nu}$. The Bessel function of the first kind is given by [96]

$$J_\nu(kx) = \sum_{l=0}^{\infty} \frac{(-1)^l}{l!\,\Gamma(l+\nu+1)}\left(\frac{kx}{2}\right)^{2l+\nu}. \tag{7.20}$$

Hence the behaviour of the Bessel function of the first kind J_ν as x approaches the origin is determined by the leading order term proportional to x^ν, and the first term in Eq. (7.18) behaves as x for $x \to 0$. On the other hand, for $x \to 0$ the function $J_{-\nu}$ behaves as $x^{-\nu}$ and the corresponding contribution involving the second term behaves as x^n. Inserting this behaviour into Eq. (7.19) one can analyze the behaviour of the two contributions of the probability current. For the contribution of J_ν one gets

$$j_\nu \overset{x\to 0}{\sim} D\left(n - \frac{\partial}{\partial x}x\right) = D(n-1). \tag{7.21}$$

Higher order contributions vanish, since the next correction is a term proportional to x^2. The contribution $j_{-\nu}$ behaves as

$$\begin{aligned} j_{-\nu} &\overset{x\to 0}{\sim} D\left(nx^{n-1} - \frac{\partial}{\partial x}x^n\right) \\ &= D\left(nx^{n-1} - nx^{n-1}\right) = 0. \end{aligned} \tag{7.22}$$

In this case higher order contributions are of the form

$$\begin{aligned} j_{-\nu} &\overset{x\to 0}{\sim} D\left(n(-1)^l x^{2l+n-1} - (-1)^l \frac{\partial}{\partial x}x^{2l+n}\right) \\ &= (-1)^l D\left(nx^{2l+n-1} - (2l+n)x^{2l+n-1}\right) \\ &= (-1)^{l+1} 2lDx^{2l+n-1}, \quad l = 1, 2, \ldots \end{aligned} \tag{7.23}$$

It is easy to see that higher order contributions vanish too as x approaches zero, since the exponent in Eq. (7.23) is positive.

The nature of the boundary at $x = 0$ clearly depends on n. From Eqs. (7.21–7.23) we can see that the probability current $j = j_\nu + j_{-\nu}$ is negative for $0 < n < 1$ and positive for $n > 1$.

This means that in the first case we have a natural absorbing boundary, as has also been stated by Bray. The corresponding solution of the Fokker-Planck equation only contains contributions of the J_ν: we have $0 < \nu < 1/2$ and thus the J_ν vanish at $x = 0$, whereas the $J_{-\nu}$ diverge. Hence the absorbing boundary condition, which requires $\lim_{x\to 0} p(x,t)$, can only be fulfilled if $B(k)$ is zero. The solution must satisfy the initial condition

$$p(x, 0) = \delta(x - x_0). \tag{7.24}$$

Using the orthogonality relation [48]

$$\delta(\alpha-\beta)=\alpha\int_0^\infty kJ_\nu(\alpha k)J_\nu(\beta k)\,dk, \tag{7.25}$$

one gets from Eq. (7.18)

$$\begin{aligned} p(x,t) &= x^{1-\nu}x_0^\nu\int_0^\infty kJ_\nu(kx_0)J_\nu(kx)\exp\left(-Dk^2t\right)\,dk \\ &= x^{1-\nu}x_0^\nu\frac{1}{2Dt}\exp\left(-\frac{x^2+x_0^2}{4Dt}\right)I_\nu\left(\frac{xx_0}{2Dt}\right). \end{aligned} \tag{7.26}$$

To obtain the second line of the previous equation, we have used the identity [97]

$$\int_0^\infty kJ_\nu(\alpha k)J_\nu(\beta k)\exp\left(-\rho^2k^2\right)\,dk=\frac{1}{2\rho^2}\exp\left(-\frac{\alpha^2+\beta^2}{4\rho^2}\right)I_\nu\left(\frac{\alpha\beta}{2\rho^2}\right), \tag{7.27}$$

where the I_ν are the modified Bessel functions of the first kind defined by

$$I_\nu(x)=\sum_{k=0}^\infty\frac{1}{k!\,\Gamma(k+\nu+1)}\left(\frac{x}{2}\right)^{\nu+2k}. \tag{7.28}$$

On the other hand in the case $n>1$ we have a positive probability current at the origin, which means that the latter is a reflecting boundary.

It is difficult to discuss the behaviour of the probability current for an arbitrary value of n since the behaviour of the Bessel functions at the origin has to be regarded separately for some n. For $\nu\in\mathbb{Z}$ the Bessel functions of the second kind must be considered instead of the $J_{-\nu}$ term, which is more difficult to do analytically; moreover the orthogonality relation given by Eq. (7.25) is valid only for $\nu>-1/2$, i.e. $n<2$. However, the nature of the boundaries of a process determined by the Itô stochastic differential equation (7.9) should only depend on the functions μ and σ. This is why a more formal and general classification of the boundaries is useful. Furthermore we shall see that this general classification is also very helpful for a more proper understanding of the mechanism of zero-crossings.

Formal classification

The modern classification of the boundaries of diffusion processes has been developed by Feller [98] and is based on semigroup operator arguments. We shall now briefly review the necessary theory for the boundary classification employing the notation of Karlin and Taylor [99], in order to be able to classify the origin for our process.

In the following let X_t be a process defined on the interval $I=(l,r)$, where the two boundaries can be both finite or infinite. Also let the process start at the initial value $X_0=x$, and a and b be two finite real numbers such that the inequality $l<a<x<b<r$ holds. We shall consider regular diffusion processes in the interior of I, i.e. processes for which the first passage time T_y with respect to an arbitrary level y in the interior of I is finite with a positive probability:

$$P(T_y<\infty|X_0=x)>0. \tag{7.29}$$

The three central quantities are

$$u(x) = P(T_b < T_a | X_0 = x) \tag{7.30}$$
$$v(x) = \langle T^* | X_0 = x \rangle \tag{7.31}$$
$$w(x) = \left\langle \int_0^{T^*} g(X_s) ds | X_0 = x \right\rangle, \tag{7.32}$$

where g is an arbitrary functional of the stochastic process, and we have defined $T^* = T_{a,b} = \min\{T_a, T_b\}$. It can be shown [99] that under certain conditions these quantities satisfy the boundary value problems

$$Lu(x) = 0, \qquad u(a) = 0, \quad u(b) = 1 \tag{7.33}$$
$$Lv(x) = -1, \qquad v(a) = 0, \quad v(b) = 0 \tag{7.34}$$
$$Lw(x) = -g(x), \quad w(a) = 0, \quad w(b) = 0, \tag{7.35}$$

with the differential operator L acting on a function $f(x)$ as follows:

$$Lf(x) = \mu(x) f'(x) + \frac{1}{2}\sigma^2(x) f''(x). \tag{7.36}$$

The proof for $u(x)$ invokes the law of total probability, and uses a Taylor expansion to the second order around x of the functional $u(X_h)$ at a small instant of time h. The proof for $w(x)$ uses a similar procedure, and finally the case $v(x)$ follows as a special case of $w(x)$ by setting $g(x) \equiv 1$.

The differential operator given by Eq. (7.36) can be written as

$$\begin{aligned} Lf(x) &= \frac{1}{2}\sigma^2(x) \left(\frac{2\mu(x)}{\sigma^2(x)} f'(x) + f''(x) \right) \\ &= \frac{1}{2m(x)} \frac{d}{dx} \left[\frac{1}{s(x)} \frac{df(x)}{dx} \right], \end{aligned} \tag{7.37}$$

with

$$s(x) = \exp\left[- \int^x \frac{2\mu(\xi)}{\sigma^2(\xi)} \, d\xi \right], \tag{7.38}$$

and the speed density

$$m(x) = \frac{1}{\sigma^2(x) s(x)}. \tag{7.39}$$

Introducing the scale function

$$S(x) = \int^x s(\eta) \, d\eta, \tag{7.40}$$

and the speed function

$$M(x) = \int^x m(\eta) \, d\eta, \tag{7.41}$$

Eq. (7.37) can be rewritten in the form

$$Lf(x) = \frac{1}{2} \frac{d}{dM(x)} \left[\frac{df(x)}{dS(x)} \right]. \tag{7.42}$$

The definitions given by Eqs. (7.38–7.41) naturally induce measures of closed intervals $J = [c, d]$, the scale measure

$$S[J] = S[c, d] = S(d) - S(c) = \int_c^d s(x)dx, \tag{7.43}$$

and the speed measure

$$M[J] = M[c, d] = M(d) - M(c) = \int_c^d m(x)dx. \tag{7.44}$$

These measures are fundamental for the classification of diffusion processes. The scale measure for an infinitesimal interval $J = [x, x + dx]$ is symbolically written as $S[dx] = S(x + dx) - S(x) = dS(x) = s(x)dx$ and, of course the same applies for the speed measure.

Then Eqs. (7.33) and (7.35) can be easily integrated first with respect to the speed measure, and then with respect to the scale measure. Using the notation introduced above the solutions can be expressed in compact form

$$u(x) = \frac{S[a, x]}{S[a, b]}, \tag{7.45}$$

and herewith

$$w(x) = 2\left\{u(x)\int_x^a S[\eta, b]g(\eta)\, dM(\eta) + [1 - u(x)]\int_x^a S[a, \eta]g(\eta)\, dM(\eta)\right\}. \tag{7.46}$$

The solution of Eq. (7.34) follows again from the special case of $g(x) \equiv 1$ in Eq. (7.46).

In the following only those definitions relevant for our classification will be mentioned and not every proof can be given in detail. Ref. [99] is excellent for a deeper understanding. For the classification of the left boundary l of a process the procedure is to regard $u(x)$ and $v(x)$ in the limit $a \to l$. An analogous approach is employed for the right boundary; however we shall only be interested in the left boundary, which in our case is the zero level.

The first definition which is important for the understanding of whether a boundary can be reached is the attractiveness. A left boundary is called *attractive* if $S(l, x] := \lim_{a\to l} S[a, x] < \infty$ for some $x \in (l, r)$. If the scale measure $S(l, x]$ is finite for some $x \in (l, r)$, this is also true for all x in this interval. Hence it follows directly from Eq. (7.45) that $P\left(T_l \le T_b | X_0 = x\right) > 0$ for all $l < x < b < r$, i.e. there is a positive probability that the left boundary is reached before the level b in the interior of the interval, provided that the former is finite.

The next question is whether a boundary is attainable in finite time. This can be measured by $\lim_{a\to l} v(x)$, which is the expectation value of the first exit time from the interval (l, b). Provided that the boundary is attracting, and using the solution $v(x)$ given by setting $g(x) \equiv 1$ in Eq. (7.46), it can be shown that it suffices to check if a certain functional called $\Sigma(l)$ is finite in order to check the attainability of the boundary. Hence a left boundary is said to be *attainable* if it is attracting and the functional

$$\Sigma(l) := \int_l^x S(l, \xi]\, dM(\xi) = \int_l^x M[\eta, x]\, dS(\eta) \tag{7.47}$$

is finite, otherwise it is said to be *unattainable*. Similarily one can define

$$N(l) := \int_l^x M(l,\xi]\, dS(\xi) = \int_l^x S[\eta, x]\, dM(\eta). \tag{7.48}$$

The classification of the left boundary of a process is based on whether the functionals $S(l,x]$, $M(l,x]$, $\Sigma(l)$, and $N(l)$ are finite or not. Of course these functionals are not independent of each other and some combinations are impossible. For example an attainable boundary is always attracting.

Using Feller's terminology, four types of boundaries can be distinguished. A process can both enter or leave from a *regular boundary*. The criteria for a left boundary to be regular are $S(l,x] < \infty$ and $M(l,x] < \infty$. In the case of an *exit boundary* it is impossible to reach any interior state b if the starting point approaches l. A boundary is an exit boundary if $\Sigma(l) < \infty$ and $M(l,x] = \infty$. An *entrance boundary* cannot be reached from the interior of the state space, but it is possible to consider processes beginning there. It suffices to show that $S(l,x] = \infty$ while $N(l) < \infty$ to prove that l is an entrance boundary. Finally a *natural* or Feller boundary can neither be reached in finite mean time nor be the starting point of a process, and the corresponding criteria are $\Sigma(l) = \infty$ and $N(l) = \infty$.

We are now able to classify the zero level of our process. The first step is to check the attractivity. The parameters determining our process are $\mu(x) = nD/x$ and $\sigma^2(x) = 2D$. Since the scaling function only depends on the upper integration limit, we can choose the lower limit in a convenient way such that

$$s(\eta) = \exp\left(\int_1^\eta \frac{n}{z}\, dz\right) = \eta^{-n}. \tag{7.49}$$

Then the scale measure of interest is

$$S(0,x] = \lim_{a\to 0}\int_a^x \eta^{-n}\, d\eta = \begin{cases} \frac{1}{1-n}\left(x^{1-n} - \lim_{a\to 0} a^{1-n}\right) & \text{for } n \neq 1 \\ \log x - \lim_{a\to 0}\log a & \text{for } n = 1 \end{cases}, \tag{7.50}$$

and thus the origin is attractive ($S(0,x] < \infty$) for $n < 1$, and non-atrractive ($S(0,x] = \infty$) for $n \geq 1$.

The speed density of the process is

$$m(\eta) = \frac{\eta^n}{2D}, \tag{7.51}$$

and we can evaluate the speed measure of an interval $(0,x]$ as

$$M(0,x] = \frac{1}{2D}\lim_{a\to 0}\int_a^x \eta^n\, d\eta = \begin{cases} \frac{1}{2D(n+1)}\left(x^{n+1} - \lim_{a\to 0} a^{n+1}\right) & \text{for } n \neq -1 \\ \frac{1}{2D}\left(\log x - \lim_{a\to 0}\log a\right) & \text{for } n = -1 \end{cases}. \tag{7.52}$$

Hence we have $M(0,x] < \infty$ for $n > -1$ and $M(0,x] = \infty$ for $n \leq -1$. We now have established the nature of the zero level for $n < 1$: if $n \leq -1$ the origin is an exit boundary and in the case $-1 < n < 1$ it is a regular boundary.

The last step is to compute $N(0)$ for the classification of the case $n \geq 1$. Using

Eq. (7.48) we get

$$\begin{aligned} N(0) &= \int_0^x S[\eta, x]\, dM(\eta) \\ &= \int_0^x \left(\int_\eta^x s(\xi)\, d\xi \right) m(\eta)\, d\eta \\ &= \frac{1}{2D} \int_0^x \left(\int_\eta^x \xi^{-n}\, d\xi \right) \eta^n\, d\eta. \end{aligned} \tag{7.53}$$

It is easy to show that this double integral is always finite, and thus the origin is an entrance boundary for $n \geq 1$.

Summarizing, the nature of the boundary at zero has the following behaviour: exit if $n \in (-\infty, -1]$, regular if $n \in (-1, 1)$, and entrance if $n \in [1, \infty)$.

7.5.2 Derivation of the backward Fokker-Planck equation

In this section we use a special Fokker-Planck technique proposed by Kearney and Majumdar [100] to obtain a differential equation for the first passage time density in Laplace space. Their method is very powerful, because the boundary conditions can be easily established in Laplace space and the functional $V[X_t]$ can be chosen such that different relevant quantities can be computed. Therefore we present the application of this method to our problem in some detail.

Considering a stochastic process starting at $X_0 = x$ governed by the stochastic differential equation (7.1), we are interested in the probability density function $f(T_b, x)$ of the first passage time T_b with respect to a certain level b, i.e. the time when the process has reached the level b for the first time.

First of all we define an arbitrary functional $V[X_t]$ by

$$T = \int_0^{T_b} V[X_t]\, dt. \tag{7.54}$$

T can have several meanings; in the special case $V[X_t] \equiv 1$ it is simply the first passage time T_b. The strategy is to find a differential equation in Laplace space for $f(T, x)$. The Laplace transform of $f(T, x)$ with respect to T is given by

$$\begin{aligned} \tilde{f}(s, x) &= \mathcal{L}_T[f(T, x)](s) \\ &= \int_0^\infty f(T, x) e^{-sT} dT = \langle e^{-sT} \rangle_T, \end{aligned} \tag{7.55}$$

where $s \in \mathbb{C}$. Splitting the interval $[0, T_b]$ into a small interval $[0, \Delta t]$ and an interval $(\Delta t, T_b]$, we can expand the integral over the small interval to first order in Δt:

$$\int_0^{\Delta t} V[X_t] dt = V[x]\Delta t + o(\Delta t). \tag{7.56}$$

Thus Eq. (7.54) becomes

$$T = V[x]\Delta t + \int_{\Delta t}^{T_b} V[X_t] dt =: T_1 + T_2. \tag{7.57}$$

Inserting Eq. (7.57) into Eq. (7.55) gives

$$\begin{aligned}\tilde{f}(s,x) &= \langle e^{-sT}\rangle_T = \langle e^{-sT_1}e^{-sT_2}\rangle_T \\ &= \int_0^\infty f(T,x)e^{-sT_1}e^{-sT_2}\,dT. \end{aligned} \tag{7.58}$$

If we split the interval $[0,T_b]$ as described above, we must take into account that we also split our trajectory in two, where the starting point of the second part, $y := X_{\Delta t} = x + \Delta x$, is random itself. Therefore the probability density takes the form

$$\begin{aligned} f(T,x) &= \int_0^b f(T_1,x)f(T_2,y)\,dy \\ &= \int_{-x}^{b-x} f(T_1,x)f(T_2,x+\Delta x)\,d(\Delta x). \end{aligned} \tag{7.59}$$

Inserting this into Eq. (7.58) and taking into account that T_1 is constant, and hence $dT = dT_2$, we obtain

$$\tilde{f}(s,x) = e^{-sV[x]\Delta t}\langle \tilde{f}(s,x+\Delta x)\rangle, \tag{7.60}$$

where the average is done over all realizations of Δx. With Taylor expansions around x of $e^{-sV[x]\Delta t}$ to the first order and of $\tilde{f}(s,x+\Delta x)$ to the second order, Eq. (7.60) becomes

$$\tilde{f}(s,x) = (1 - sV[x]\Delta t)\left(\tilde{f}(s,x) + \frac{\partial \tilde{f}(s,x)}{\partial x}\langle \Delta x\rangle + \frac{1}{2}\frac{\partial^2 \tilde{f}(s,x)}{\partial x^2}\langle \Delta x^2\rangle\right). \tag{7.61}$$

In a first order approach

$$\Delta x = \frac{nD}{x}\Delta t + \sqrt{2D}\Delta W_t, \tag{7.62}$$

where $\Delta W_t = W_{t+\Delta t} - W_t$, and thus, using Eq. (7.2),

$$\langle \Delta x\rangle = \frac{nD}{x}\Delta t. \tag{7.63}$$

Then the mean value of $\langle \Delta x^2\rangle$ is, making again use of the zero mean property of the Wiener process, as well as of its autocorrelation function given in Eq. (7.3),

$$\langle \Delta x^2\rangle = 2D\Delta t + o(\Delta t). \tag{7.64}$$

Finally, putting $V[X_t] \equiv 1$, we get the desired backward Fokker-Planck equation for the first passage time probability density in Laplace space:

$$\frac{\partial^2 \tilde{f}(s,x)}{\partial x^2} + \frac{n}{x}\frac{\partial \tilde{f}(s,x)}{\partial x} - \frac{s}{D}\tilde{f}(s,x) = 0. \tag{7.65}$$

7.5.3 Formulation of the boundary value problem

We now proceed to the formulation of the boundary value problems corresponding to the solutions of the first passage time probability densities, distinguishing between the three classes of boundaries the origin can belong to, as discussed in Section 7.5.1. However, as for the right boundary, we impose an absorbing boundary at b: The first passage time vanishes for $x \to b^-$, and hence the exponent in Eq. (7.55) is zero, giving

$$\lim_{x \to b^-} \tilde{f}(s, x) = 1. \tag{7.66}$$

The simplest case is if the zero level is an entrance boundary, i.e. $n \geq 1$. Starting from an intitial value $X_0 = x > 0$, the zero level can never be reached, which corresponds to a reflecting wall at the origin. Applying standard arguments for reflecting boundaries [5], the corresponding boundary condition is

$$\lim_{x \to 0^+} \frac{\partial \tilde{f}(s, x)}{\partial x} = 0. \tag{7.67}$$

For $n \leq -1$ the origin is an exit boundary. This means that it is impossible to reach any interior point of the state space if the initial point approaches the origin. This means that we have an absorbing boundary corresponding to

$$\lim_{x \to 0^+} \tilde{f}(s, x) = 1, \tag{7.68}$$

and the first passage time will not converge. Instead of the first passage time the analysis of the previous section resulting in the backward Fokker-Planck equation (7.65) together with the boundary conditions (7.66) and (7.68) gives us the first exit time from the interval $(0, b)$.

In the case of a regular boundary, which happens for $-1 < n < 1$, the behaviour is the most complicated. The process can both reach and leave the boundary, which means that also zero crossings are possible and the support of the process is the whole real axis. The first exit time from $(0, b)$ is again given by the same boundary condition problem as in the case of the exit boundary.

For the sake of simplicity we change the variable names from $\tilde{f}$ to y. Restricting the process to the positve half axis our boundary value problem for the three different kinds of boundaries the origin can belong to reads

$$y''(x) + \frac{n}{x} y'(x) - \frac{s}{D} y(x) = 0 \tag{7.69}$$

$$\mathbf{A}\mathbf{y}(0) + \mathbf{B}\mathbf{y}(a) = \mathbf{c}, \tag{7.70}$$

where

$$\mathbf{y}(x) = \begin{pmatrix} y(x) \\ y'(x) \end{pmatrix}, \quad \mathbf{B} = \begin{pmatrix} 0 & 0 \\ 1 & 0 \end{pmatrix}. \tag{7.71}$$

An absorbing boundary at zero corresponds to

$$\mathbf{A} = \begin{pmatrix} 1 & 0 \\ 0 & 0 \end{pmatrix}, \quad \mathbf{c} = \begin{pmatrix} 1 \\ 1 \end{pmatrix}, \tag{7.72}$$

whereas a reflecting boundary at zero corresponds to

$$\mathbf{A} = \begin{pmatrix} 0 & 1 \\ 0 & 0 \end{pmatrix}, \quad \mathbf{c} = \begin{pmatrix} 0 \\ 1 \end{pmatrix}. \tag{7.73}$$

Multiplying Eq. (7.69) with the integrating factor $e^{\int \frac{n}{x} dx}$ leads to

$$-(x^n y')' = -\frac{s}{D} x^n y. \tag{7.74}$$

This is the canonical Sturm-Liouville form [101]

$$-(py')' + qy = \lambda w y, \tag{7.75}$$

with $p(x) = x^n$, the weighting function $w(x) = x^n$, $q(x) \equiv 0$, and the spectral parameter $\lambda = -s/D$.

We now observe that $u := y - 1$ transforms the homogeneous problem (7.69) with inhomogeneous boundary conditions (7.70) into an inhomogeneous problem with homogeneous boundary, conditions

$$-(pu')' = \lambda w u + \lambda w \tag{7.76}$$

$$\mathbf{A}\mathbf{u}(0) + \mathbf{B}\mathbf{u}(a) = 0, \tag{7.77}$$

where $\mathbf{u}(x) = (u(x),\ u'(x))^{\mathsf{T}}$, and the two possible choices of $\mathbf{A}$ and $\mathbf{c}$ correspond to the Dirichlet problem and the Dirichlet-Neumann problem respectively. This is easier to solve, since it determines a self-adjoint operator $\mathcal{L}$ defined by

$$\mathcal{L}u = \frac{1}{w}\left[-(pu')'\right] \tag{7.78}$$

in the weighted Hilbert space $H = L^2(J, w)$, where we have defined the open interval $J = (0, b)$. This operator is not to be confused with the Laplace transformation operator in Eq. (7.55), which can be recognized from the index indicating the transformed variable.

This can be seen as follows: Let $u, v \in H$. Then the inner product is given by $\langle u, v\rangle = \int_0^b \bar{u} v w \, dx$; taking into account that u and v satisfy the homogeneous boundary conditions (7.77), we get after integrating twice by parts

$$\begin{aligned} \langle u, \mathcal{L}v\rangle &= -\int_0^b \bar{u}(pv')' \, dx \\ &= \left[p(v\bar{u}' - \bar{u}v')\right]_0^b - \int_0^b (p\bar{u}')' v \, dx \\ &= \langle \mathcal{L}u, v\rangle. \end{aligned} \tag{7.79}$$

Using the definition from Eq. (7.78) the boundary value problem given by Eqs. (7.69–7.70) can be simplified to

$$(\mathcal{L} - \lambda \mathbf{1})u = \lambda, \tag{7.80}$$

$$\mathbf{A}\mathbf{u}(0) + \mathbf{B}\mathbf{u}(b) = 0. \tag{7.81}$$

7.6 Formal solution of the boundary value problem

We now exploit the property that the homogeneous boundary value problem with homogeneous boundary conditions

$$\begin{aligned} (\mathcal{L} - \alpha \mathbf{1})u &= 0, \\ \mathbf{A}\mathbf{u}(0) + \mathbf{B}\mathbf{u}(b) &= 0, \end{aligned} \tag{7.82}$$

has nontrivial solutions u_k with eigenvalues α_k, $k = 1, 2, \ldots$

$$\mathcal{L}u_k = \alpha_k u_k. \tag{7.83}$$

Because of the self-adjointness of $\mathcal{L}$, the eigenvalues α_k are real and the eigenfunctions u_k form an orthonormal basis of H. Furthermore $\alpha_k > 0$ holds, since $\alpha_k = \langle u_k, \mathcal{L}u_k \rangle$.

Hence the solution u of the inhomogeneous problem given by Eqs. (7.80) and (7.81) can be expressed as an expansion in this basis,

$$u = \sum_{k=1}^{\infty} c_k u_k, \tag{7.84}$$

with $c_k = \langle u_k, u \rangle$. The coefficients c_k can be derived from Eq. (7.80):

$$\langle u_k, \mathcal{L}u \rangle - \langle u_k, \lambda u \rangle = \langle u_k, \lambda \rangle. \tag{7.85}$$

Again, making use of the definition of a self-adjoint operator, we can pull $\mathcal{L}$ into the first component of the inner product. Employing Eq. (7.83) we get

$$c_k = \frac{\langle u_k, \lambda \rangle}{\alpha_k - \lambda}. \tag{7.86}$$

The solution of the inhomogeneous problem reads

$$u = \sum_{k=1}^{\infty} \frac{\langle u_k, \lambda \rangle}{\alpha_k - \lambda} u_k, \tag{7.87}$$

and hence

$$y = 1 + \sum_{k=1}^{\infty} \frac{\langle u_k, \lambda \rangle}{\alpha_k - \lambda} u_k. \tag{7.88}$$

The eigenfunctions u_k do not depend on $\lambda = -s/D$, and making use of the linearity of the inverse Laplace transformation one gets

$$\begin{aligned} y(t,x) &= \mathcal{L}_s^{-1}[y(s,x)](t) \\ &= \mathcal{L}_s^{-1}[1] + \sum_{k=1}^{\infty} \langle u_k, 1 \rangle u_k \, \mathcal{L}_s^{-1}\left[\frac{\lambda}{\alpha_k - \lambda}\right] \\ &= \delta(t) + \sum_{k=1}^{\infty} \langle u_k, 1 \rangle u_k (\alpha_k D e^{-\alpha_k D t} - \delta(t)). \end{aligned} \tag{7.89}$$

This can be further simplified. Using Eq. (7.84) we know that $\sum_{k=1}^{\infty} \langle u_k, 1 \rangle u_k = 1$ and hence the two delta functions cancel out. Then we have

$$y(t,x) = \sum_{k=1}^{\infty} \langle u_k, 1 \rangle u_k \alpha_k D e^{-\alpha_k D t}. \tag{7.90}$$

This function is normalized because, knowing that α_k is positive,

$$\begin{aligned} \int_0^{\infty} y(t,x)\, dt &= \sum_{k=1}^{\infty} \langle u_k, 1 \rangle u_k \alpha_k D \int_0^{\infty} e^{-\alpha_k D t}\, dt \\ &= \sum_{k=1}^{\infty} \langle u_k, 1 \rangle u_k = 1. \end{aligned} \tag{7.91}$$

We are now able to solve the specific boundary value problems for the three different kinds of boundaries at zero.

7.6.1 Entrance boundary

As we know from the classification of the origin, we have an entrance boundary for $n \geq 1$ or $\nu \leq 0$. The general solution of the homogeneous differential equation (7.82) is

$$u(x) = Ax^{\nu} J_{\nu}\left(\sqrt{\alpha}x\right) + Bx^{\nu} Y_{\nu}\left(\sqrt{\alpha}x\right), \tag{7.92}$$

where J_ν and Y_ν are the Bessel functions of the first and second kind respectively. The derivative of the general solution reads

$$u'(x) = x^{\nu}\sqrt{\alpha}\left[AJ_{\nu-1}\left(\sqrt{\alpha}x\right) + BY_{\nu-1}\left(\sqrt{\alpha}x\right)\right]. \tag{7.93}$$

In the limit $x \to 0$ and for $\nu \in \mathbb{Z}$ the term containing the Bessel functions of the second kind diverges whereas the one involving the Bessel functions of the first kind is zero; the boundary condition $\lim_{x\to 0} u'(x) = 0$ can only be fulfilled if $B = 0$. The second boundary condition $u(b) = 0$ gives us the eigenvalues of the problem by the requirement that $J_\nu(\sqrt{\alpha_k}b) = 0$. Calling the ith zero of the Bessel function of the first kind j_i, one can use the orthogonality relation for Bessel functions [96]

$$\int_0^b J_{\nu}\left(j_m\frac{x}{b}\right) J_{\nu}\left(j_n\frac{x}{b}\right) x\, dx = \frac{1}{2}b^2 J_{\nu+1}^2(j_m)\delta_{mn} \tag{7.94}$$

to compute the constant A. Identifying j_i with $\sqrt{\alpha_i}b$, the normalized eigenfunctions of the problem read

$$u_k(x) = \frac{\sqrt{2}b^{\nu-1}\left(\frac{x}{b}\right)^{\nu} J_{\nu}\left(j_k\frac{x}{b}\right)}{J_{\nu+1}\left(j_k\right)}. \tag{7.95}$$

For non-integer ν the Bessel functions J_ν and $J_{-\nu}$ are two linear independent solutions of Eq. (7.82), and writing the general solution as the linear combination

$$u(x) = Ax^{\nu} J_{\nu}\left(\sqrt{\alpha}x\right) + Bx^{\nu} J_{-\nu}\left(\sqrt{\alpha}x\right) \tag{7.96}$$

instead of using Eq. (7.92) makes the analysis easier. The derivative reads

$$u'(x) = x^{\nu}\sqrt{\alpha}\left[AJ_{\nu-1}(\sqrt{\alpha}x) - BJ_{1-\nu}(\sqrt{\alpha}x)\right]. \tag{7.97}$$

In this case the function $x^\nu J_{\nu-1}(\sqrt{\alpha}x)$ diverges as we approach the origin, and hence we have to set $A = 0$ in order to fulfill the left boundary condition. The right boundary condition determines the eigenvalues by a similar requirement as in the previous case, namely that $j_k = \sqrt{\alpha_k}b$ is a root of the Bessel function $J_{-\nu}$. Again the second constant is evaluated using Eq. (7.94), and the normalized functions are

$$u_k(x) = \frac{\sqrt{2}b^{\nu-1}\left(\frac{x}{b}\right)^{\nu} J_{-\nu}\left(j_k\frac{x}{b}\right)}{J_{1-\nu}(j_k)}. \tag{7.98}$$

It is easy to prove that the eigenfunctions given by Eqs. (7.95) and (7.98) fulfill the normalization condition (7.91). Evaluating the scalar products we get after some tedious but straightforward algebra:

$$\begin{aligned}
\sum_{k=1}^{\infty}\langle u_k, 1\rangle u_k &= \sum_{k=1}^{\infty}\frac{2^{\frac{1}{2}}a^{1-\nu}}{j_k}\left(\frac{2^{1-\nu}j_k^{\nu-1}}{\Gamma(\nu)J_{\nu+1}(j_k)} + 1\right)\frac{2^{\frac{1}{2}}a^{\nu-1}}{J_{\nu+1}(j_k)}z^{\nu}J_{\nu}(j_k z) \\
&= \sum_{k=1}^{\infty}\frac{2^{2-\nu}z^{\nu}j_k^{\nu-1}}{j_k\Gamma(\nu)J_{\nu+1}^2(j_k)}J_{\nu}(j_k z) + \sum_{k=1}^{\infty}\frac{2z^{\nu}}{j_k J_{\nu+1}(j_k)}J_{\nu}(j_k z) \\
&= z^{\nu}\sum_{k=1}^{\infty}\frac{2^{2-\nu}j_k^{\nu-1}}{j_k\Gamma(\nu)J_{\nu+1}^2(j_k)}J_{\nu}(j_k z) + z^{\nu}\sum_{k=1}^{\infty}\frac{2}{j_k J_{\nu+1}(j_k)}J_{\nu}(j_k z),
\end{aligned} \tag{7.99}$$

where we have set $z = x/b$. Making use of the Fourier-Bessel expansion

$$z^\nu = \sum_{k=1}^{\infty} \frac{2}{j_k J_{\nu+1}(j_k)} J_\nu(j_k z), \tag{7.100}$$

we obtain

$$\sum_{k=1}^{\infty} \langle u_k, 1 \rangle u_k = z^\nu \left[\sum_{k=1}^{\infty} \left(\frac{2}{j^k} \right)^{2-\nu} \frac{1}{\Gamma(\nu) J_{\nu+1}^2(j_k)} J_\nu(j_k z) + z^\nu \right], \tag{7.101}$$

and identifying the sum with the Fourier-Bessel expansion of $z^{-\nu} - z^\nu$ the desired property is shown.

Fig. 7.1 shows the comparison between the theoretical curves and simulations for the case of an entrance boundary at the origin.

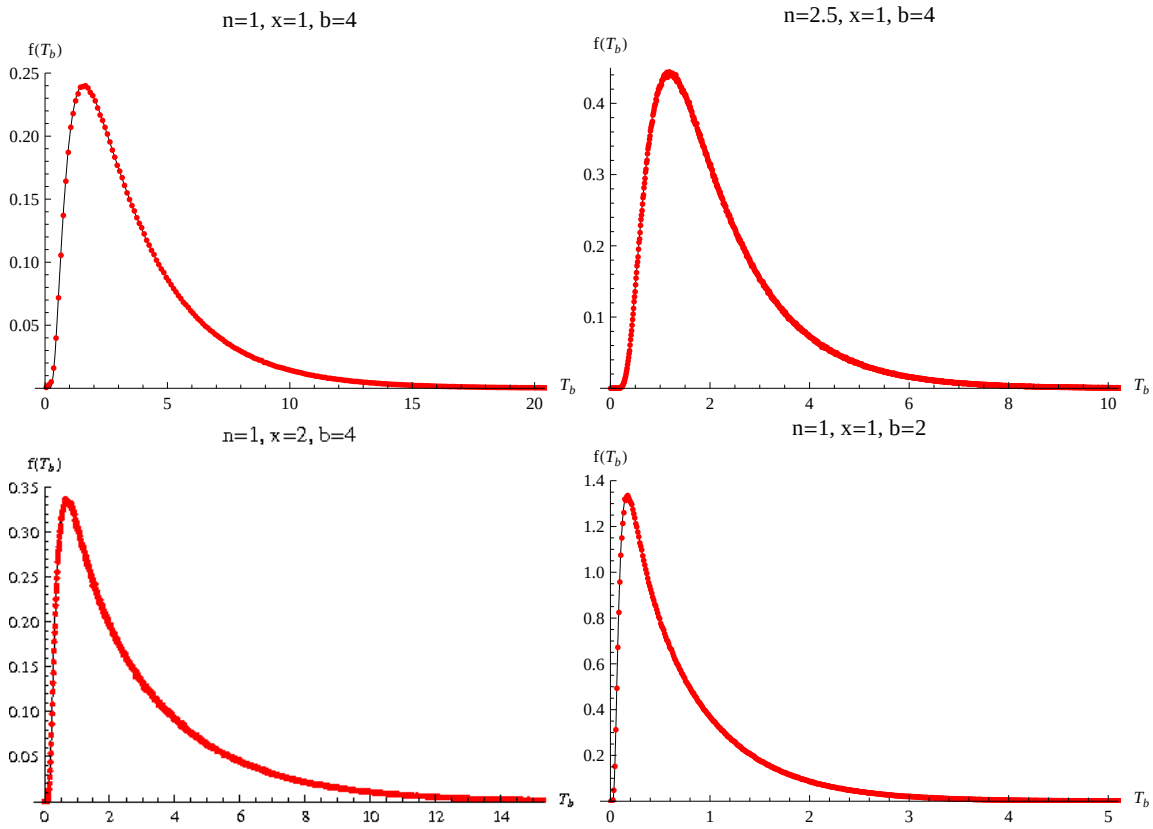

Figure 7.1: First passage time probability density function for an entrance boundary at the origin. The parameters n, x and b are varied. The diffusion coefficient is always $D = 1$. The continuous lines are the theoretical curves obtained by truncating the sum (7.90) after the first 200 terms, and the dots are the values obtained by Monte Carlo simulations.

In the case of an entrance boundary a further refinement of the simulation algorithm is possible. Knowing that the zero level can never be reached from the interior of the state space of the process, it is clear that negative values in the simulations must result from discretization errors. If this is the case we can reduce the time step until the propagated value of the process is positive.

7.6.2 Exit boundary

If the zero level is an exit boundary it is impossible to reach any interior point b, provided that the starting point of the process is "sufficiently close" to the boundary. Hence the first passage time will not converge in general. However, the analysis of the previous sections together with an absorbing boundary condition at the origin delivers the probability density of the first exit time $T_{0,b} = \min\{T_0, T_b\}$ from the interval $(0, b)$. For $n \leq -1$ the first terms in Eqs. (7.92) or (7.96) vanish in the limit $x \to 0$, whereas the second terms are finite. Therefore the constant B must be zero in order to fulfill the required boundary condition $u(b) = 0$. Thus the eigenfunctions are given by Eq. (7.95), just as in the case of an entrance boundary for $\nu \in \mathbb{Z}$.

In Fig. 7.2 the theoretical curves are again compared with the results obtained via Monte Carlo simulations. It is interesting to notice that the density is bimodal for some choices of the parameters.

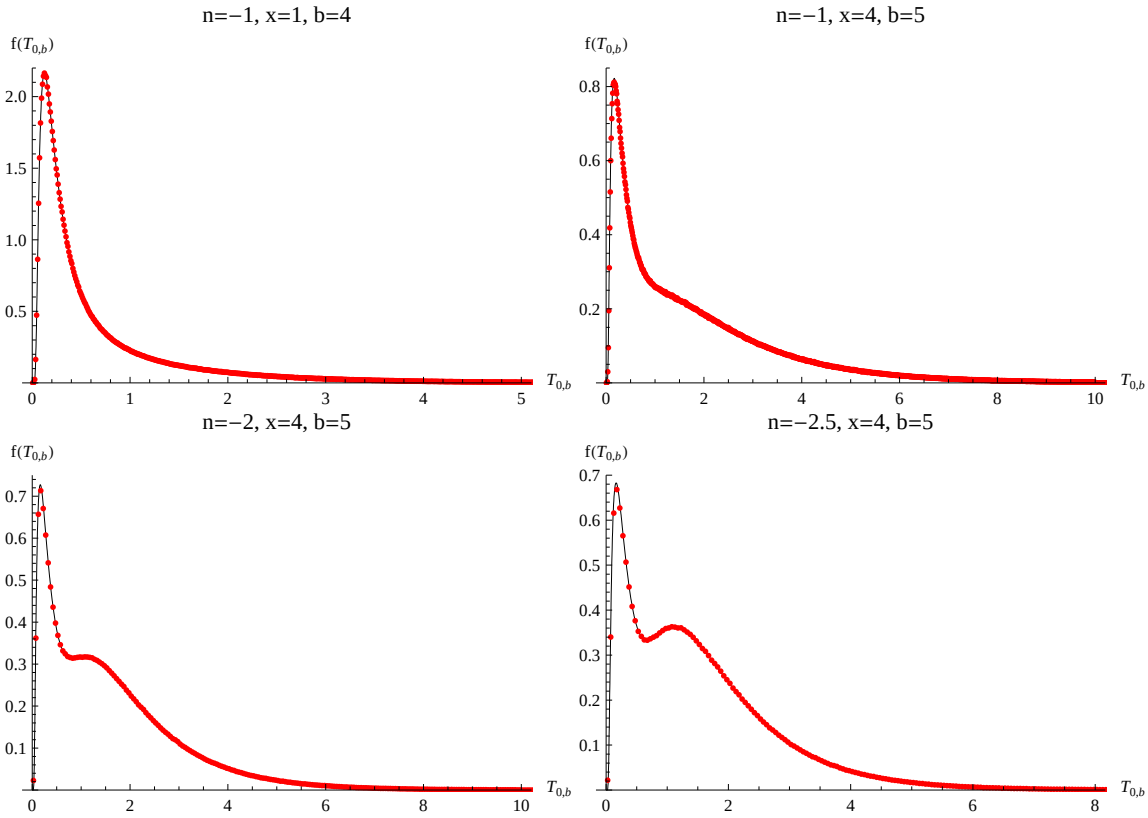

Figure 7.2: First exit time probability density functions for an entrance boundary at the origin. The continuous lines represent again the theoretical curves and the dots the points obtained from the simulations.

7.6.3 Regular boundary

The case when the origin is a regular boundary is the most complicated one. In Ref. [99] the regular boundary is described as follows:

> *For a regular boundary a variety of boundary behaviour can be prescribed in a consistent way, including the contingencies of complete absorption or reflecting, elastic or sticky barrier phenomena, and even the possibility*

of the particle (path), when attaining the boundary point, waiting there for an exponentially distributed duration followed by a jump into the interior of the state space according to a specified probability distribution function. In the latter event, the process only exhibits continuous sample paths over the interior of the state space.

However, we first observe that imposing an absorbing boundary condition at the origin gives us the probability densities of the first exit times. The eigenfunctions are computed in the same way as in the case of an exit boundary at the origin, and are again given by Eq. (7.95). Fig. 7.3 illustrates the results.

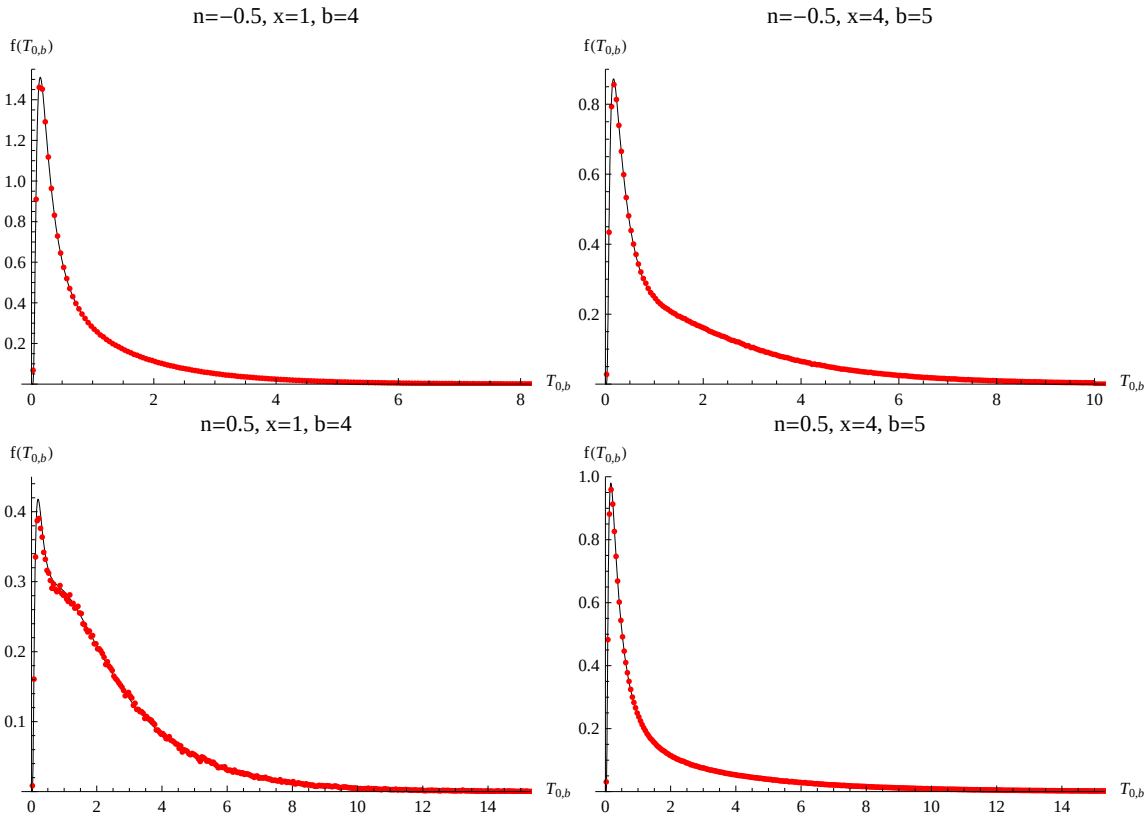

Figure 7.3: First exit time probability densities in the case when the origin is a regular boundary

If $n > 0$ the first passage time probability density is approximated well for small times imposing a reflecting boundary at the origin, but the maximum of the distribution obtained from the simulations is higher then the one in the theoretical curve, as Fig. 7.4 indicates.

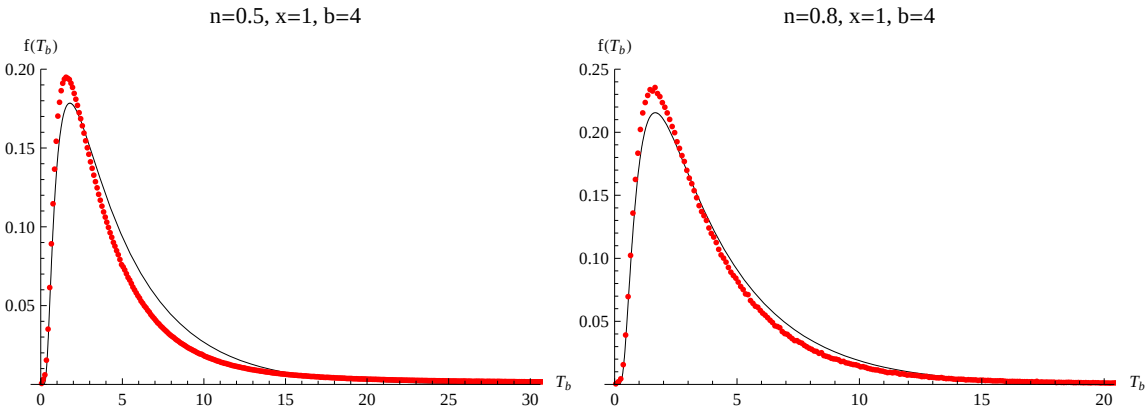

Figure 7.4: First passage time probability densities for a regular boundary at the origin.

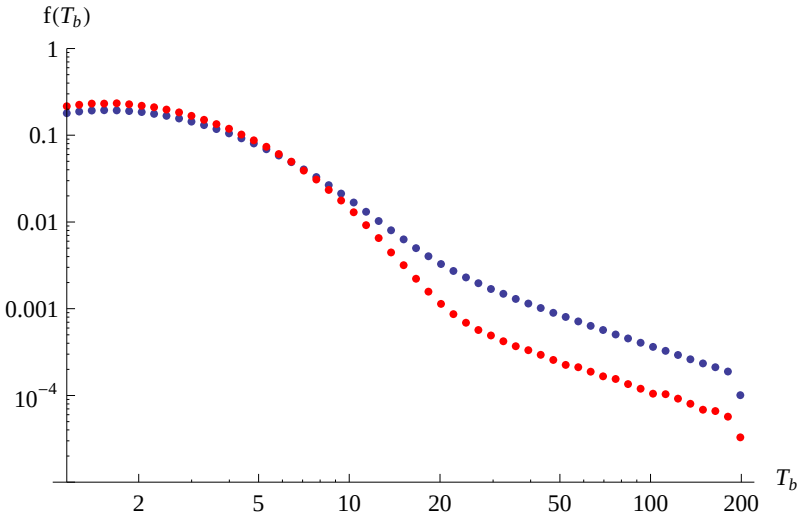

Figure 7.5: Logarithmic plot of first passage time densities for a regular boundary at the origin. The blue curve corresponds to the choice $n = 0.5, x = 1, b = 4$, and the red one to $n = 0.8, x = 1, b = 4$.

Fig. 7.5 shows a logarithmic plot of the first passage time densities, and one can see that the latter are heavy-tailed, i.e. they exhibit a power law decay for long times. A possible interpretation of the power law decay for a regular boundary at the origin as opposed to the exponential decay observed for the entrance boundary are the possible zero crossings of the path and the positive amount of time spent in the vicinity of the "sticky" boundary.

It is interesting to note that sticky boundaries may have applications e.g. for the simulation of the partial adsorption of polymer molecules to walls and for the modeling of solvent quality [102].

7.7 Conclusions

We have computed first passage time and first exit time probability densities for a stochastic process with applications in many physical, chemical and biological problems. Depending on the nature of the boundary at the origin we have found analytical solutions for the first passage time and first exit time densities for all cases, except for the first passage time density in the case of a regular boundary at the origin. In the latter case we have found an analytical solution for the first exit time density and approximations for the first passage time density for short times. For this specific stochastic process regularity of the boundary at zero can include behaviours ranging from total absorption to total reflection, with intermediate behaviours like elastic and sticky boundaries [99]. In possible future projects this could be investigated more thoroughly and regarded from the perspective of interactions between molecules and boundary surfaces, which is closely connected to our MD simulations in confined geometries.

Summary and outlook

The topic of this thesis is computational chemical physics of simple and complex systems, in particular liquids, including analytical calculations of first passage times in a model stochastic process with a large number of applications. The complexity of the systems of interest was gradually increased: starting from Lennard-Jones fluids we passed to a discotic liquid-crystalline system, and finally a generic phenomenological model which has also applications in complex biological systems was studied.

In Chapter 1 the basic notions of statistical mechanics are reviewed. Statistical mechanics can be reformulated in the language of stochastic processes. While the pioneering works of Boltzmann and Maxwell rely on simple probabilistic assumptions, more and more problems are now considered using the tool of stochastic analysis, which is itself an evolving field of science. In Chapter 2 the most important concepts of stochastic processes were sketched in an informal way. The computational tool used most frequently in this thesis were molecular dynamics simulations; this method was explained in Chapter 3.

Boltzmann's H-theorem, that describes the entropy increase of an ideal gas, lies at the foundation of statistical mechanics. However, in deriving his theorem, Boltzmann used the assumption of molecular chaos, which was subject to the recurrence paradox and the reversibility paradox. The Ehrenfest urn model explains the contradiction between the reversibility of thermodynamics arising from deterministic mechanics. Using molecular dynamics simulations, we have checked that applying the Ehrenfest urn model to a realistic Lennard-Jones fluid the Markov assumption stated by Penrose holds even in the case of the liquid phase. Chapters 4 and 5 are devoted to these problems. Further investigations along this line using an even more basic model of liquids, hard spheres, were done too within this thesis, but have not been presented here because of lack of time. Nevertheless, two publications on the results are in progress.

In Chapters 6 and 7 the complexity of the intermolecular interactions was increased. After an introduction to the basic quantities and phenomenological theories of a liquid-crystalline system, a model Gay-Berne discogen confined in a cylindrical nanopore was studied via molecular dynamics. The obtained structures agree well with experimental findings. Discotic liquid crystals are interesting from a technical point of view because the columnar phase exhibits a stronger conductivity along the column axis than across it, which offers the possibility of optoelectronic applications.

In Chapter 7 first passage times of a stochastic process with respect to a certain level were studied. First passage times play an important role in chemical physics, in particular for models of liquids and liquid crystals. The first passage time probability density was computed analytically and validated via Monte Carlo simulations using the Euler-Maruyama integration algorithm for stochastic differential equations.

Many problems can be treated exploiting both stochastic and deterministic computational methods. An example is measuring diffusion as a first passage problem with respect to a sphere surrounding a tagged particle, as done by Munakata [70]. This is interesting because the process we have discussed in Chapter 7 can be mapped on the Bessel process, which is defined as radial Brownian motion, i.e. the process describing the Euclidean distance from the origin of an N-dimensional Brownian motion.

Danksagung

Denjenigen, die mich auf dem Weg zur Entstehung dieser Arbeit begleitet und einige Höhen und Tiefen miterlebt haben, möchte ich danken. Zunächst gilt mein Dank natürlich meinem Betreuer, Prof. Dr. Guido Germano, der mir die Möglichkeit gegeben hat dieses Projekt zu bearbeiten, mich in die Methoden der Computersimulation eingeführt hat und auch sonst in konstruktiven und lehrreichen Gesprächen ein offenes Ohr für wissenschaftliche und nichtwissenschaftliche Probleme hatte.

Prof. Dr. Enrico Scalas danke ich auch für die fruchtbare Zusammenarbeit und stets interessante und horizonterweiternde Gespräche; es war mir eine Ehre.

Prof. Dr. Ulrich Behn von der Universität Leipzig, der Betreuer meiner Diplomarbeit, hat mit seiner Bereitschaft das Projekt meiner Diplomarbeit weiter zu führen einen wesentlichen Beitrag zu der Entstehung des letzen Kapitels geleistet; auch von ihm habe ich mehr als nur fachliche Unterstützung erfahren. Dafür danke ich.

Dr. Christopher Stillings möchte ich für Einblicke in Experimente danken, es war ebenfalls eine fruchtbare, interessante und manchmal auch lustige Zusammenarbeit.

Danke auch an meine Kollegen Adrian Gabriel, Daniel Fulger, Ulrich Welling und Dr. Mauro Politi, die mir manchen nützlichen Tipp gegeben haben; Adrian war kein Programmierproblem zu schwer, und Mauro hat trotz der ungewohnten deutschen Küche nie vor der Marburger Mensa kapituliert.

Auf privater Ebene möchte ich meiner Freundin Erika Dahlmanns für ihre Unterstützung in schweren Zeiten und vieles mehr danken.

Zu guter Letzt möchte ich meiner Familie, besonders aber meinen Eltern, die mich auf dem ganzen Weg begleitet haben, danken. Ihnen möchte ich diese Arbeit widmen.

Eigenständigkeitserklärung

Ich versichere hiermit, dass ich meine Dissertation selbstständig und ohne unerlaubte Hilfe angefertigt und mich dabei keiner anderen als der von mir ausdrücklich bezeichneten Quellen und Hilfen bedient habe.

Die Dissertation wurde in der jetzigen oder einer ähnlichen Form noch bei keiner anderen Hochschule eingereicht und hat noch keinen sonstigen Prüfungszwecken gedient.

Marburg, März 2009

Edgar Martin

Bibliography

[1] O. Penrose, *Foundations of Statistical Mechanics*, Pergamon Press, Oxford, 1970.

[2] N. Goldenfield and L. Kadanoff, Science **284**, 87 (1999).

[3] P. Ehrenfest and T. Ehrenfest, Begriffliche Grundlagen der statistischen Auffassung in der Mechanik, in *Encyklopädie der Mathematischen Wissenschaften mit Einschluß ihrer Anwendungen*, edited by F. Klein and C. Müller, volume 4, page 3, Teubner, Leipzig, 1911, English translation in P. Ehrenfest and T. Ehrenfest, *The Conceptual Foundations of the Statistical Approach in Mechanics*, Dover, New York (1990).

[4] A. Einstein, Ann. Phys. **17**, 549 (1905).

[5] C. W. Gardiner, *Handbook of Stochastic Methods*, Springer, Berlin, 2nd edition, 2002.

[6] B. J. Alder and T. E. Wainwright, J. Chem. Phys. **27**, 1208 (1957).

[7] W. W. Wood and J. D. Jacobson, J. Chem. Phys. **27**, 1207 (1957).

[8] A. Rahman, Phys. Rev. **136**, A405 (1964).

[9] L. Verlet, Phys. Rev. **159**, 98 (1967).

[10] M. E. Tuckerman, B. J. Berne, and G. J. Martyna, J. Chem. Phys. **97**, 1990 (1992).

[11] H. F. Trotter, Proc. Am. Math Soc. **10**, 545 (1959).

[12] H. C. Andersen, J. Chem. Phys. **72**, 2384 (1980).

[13] S. Nosé, J. Chem. Phys. **81**, 511 (1984).

[14] A. Sergi, M. Ferrario, and D. Costa, Mol. Phys. **97**, 825 (1999).

[15] W. G. Hoover, Phys. Rev. A. **31**, 1695 (1985).

[16] L. Boltzmann, Wien. Ber. **66**, 275 (1872).

[17] J. Loschmidt, Wien. Ber. **73**, 139 (1876).

[18] J. Loschmidt, Wien. Ber. **75**, 67 (1877).

[19] E. Zermelo, Ann. Physik **57**, 485 (1896).

[20] D. ter Haar, *Elements of Statistical Mechanics*, Rinehart & Co., New York, 1954.

[21] D. ter Haar, Rev. Mod. Phys. **27**, 289 (1955).

[22] R. C. Tolman, *The Principles of Statistical Mechanics*, Oxford University Press, Oxford, 1938.

[23] P. Ehrenfest and T. Ehrenfest, Phys. Zeit. **8**, 311 (1907).

[24] P. G. Hoel, S. C. Port, and C. J. Stone, *Introduction to Stochastic Processes*, Houghton Mifflin, Boston, 1972.

[25] D. Costantini and U. Garibaldi, Synthese **139**, 107 (2004).

[26] Y. G. Sinai, *Probability Theory: An Introductory Course*, Springer, Berlin, 1992.

[27] F. Kohlrausch and E. Schrödinger, Phys. Zeit. **27**, 306 (1926).

[28] C. Godrèche and J. M. Luck, J. Phys.: Condens. Matter **14**, 1601 (2002).

[29] M. P. Allen and D. J. Tildesley, *Computer Simulation of Liquids*, Oxford University Press, paperback edition, Oxford, 1989.

[30] D. Frenkel and B. Smit, *Understanding Molecular Simulation*, Academic Press, San Diego, 2nd edition, 2002.

[31] W. A. Steele, Surf. Sci. **36**, 317 (1973).

[32] J. J. Nicolas, K. E. Gubbins, W. B. Street, and D. J. Tildesley, Mol. Phys. **37**, 1429 (1979).

[33] A. Z. Panagiotopoulos, Mol. Phys. **61**, 813 (1987).

[34] W. Swope, H. Andersen, P. Berens, and K. Wilson, J. Chem. Phys. **76**, 637 (1982).

[35] M. R. Wilson, M. P. Allen, M. A. Warren, A. Sauron, and W. Smith, J. Comput. Chem. **18**, 478 (1997).

[36] W. Feller, Ann. Math. Stat. **30**, 1952 (1959).

[37] M. A. Stephens, J. Am. Stat. Assoc. **69**, 730 (1974).

[38] M. Kac, *Probability and Related Topics in Physical Science*, Interscience Publishers, London, 1959.

[39] E. Scalas, E. Martin, and G. Germano, Phys. Rev. E **76**, 011104 (2007).

[40] P. Allegrini, J. F. Douglas, and S. C. Glotzer, Phys. Rev. E **60**, 5714 (1999).

[41] M. Letz and R. Schilling, Phil. Mag. B **79**, 1815 (1999).

[42] P. P. Jose, D. Chakrabarti, and B. Bagchi, Phys. Rev. E **71**, 030701(R) (2005).

[43] D. Andrienko, *Introduction to Liquid Crystals*, International Max Planck Research School in Bad Marienberg, September 2006, http://mpip-mainz.mpg.de/∼andrienk/lectures/IMPRS/liquid_crystals.pdf.

[44] `http://en.wikipedia.org/wiki/Liquid_crystal`.

[45] S. Chandrasekhar, B. K. Sadashiva, and K. A. Suresh, Pramna **9**, 471 (1977).

[46] H. Cordes et al., Phys. Rev. B **63**, 094201 (2001).

[47] K. Kohary et al., Phys. Rev. B **63**, 094202 (2001).

[48] G. Arfken, *Mathematical Methods for Physicists*, Academic Press, Orlando, 3rd edition, 1985.

[49] L. Onsager, Proc. N.Y. Acad. Sci. **51**, 627 (1949).

[50] W. Maier and A. Saupe, Z. Naturforsch. A **13**, 564 (1958).

[51] M. Steinhart et al., Nano Lett. **5**, 429 (2005).

[52] C. Stillings et al., Mol. Cryst. Liq. Cryst. **495**, 285 (2008).

[53] B. Orgasinska, T. S. Perova, K. Merkel, A. Kocot, and J. K. Vij, Mater. Sci. Eng. C **8–9**, 283 (1999).

[54] D. Caprion, L. Bellier-Castella, and J. P. Ryckaert, Phys. Rev. E **67**, 041703 (2003).

[55] L. Bellier-Castella, D. Caprion, and J.-P. Ryckaert, J. Chem. Phys. **121**, 4874 (2004).

[56] A. P. J. Emerson, G. R. Luckhurst, and S. G. Whatling, Mol. Phys. **82**, 113 (1994).

[57] M. A. Bates and G. R. Luckhurst, J. Chem. Phys. **104**, 6696 (1996).

[58] H. Zewdie, Phys. Rev. E **57**, 1793 (1998).

[59] G. Cinacchi, R. Colle, and A. Tani, J. Phys. Chem B **108**, 7969 (2004).

[60] G. D. Wall and D. J. Cleaver, Phys. Rev. E **56**, 4306 (1997).

[61] M. M. Pineiro, A. Galindo, and A. O. Parry, Soft Matter **3**, 768 (2007).

[62] D. Caprion, Discotic molecules in cylindrical nanopores: a Monte Carlo study, Eur. Phys. J. E, submitted (2008).

[63] G. Jiang, J. Zhang, and W. Wang, ANZIAM J. **46**, E70 (2004).

[64] J. G. Gay and B. J. Berne, J. Chem. Phys. **74**, 3316 (1981).

[65] M. P. Allen and G. Germano, Mol. Phys. **104**, 3225 (2006).

[66] A. T. Gabriel, T. Meyer, and G. Germano, J. Chem. Theory Comput. **4**, 468 (2008).

[67] E. W. Montroll and K. E. Shuler, Adv. Chem. Phys. **1**, 361 (1958).

[68] B. J. Widom, J. Chem. Phys **30**, 238 (1959).

[69] F. H. Ree, T. S. Ree, T. Ree, and H. Eyring, Adv. Chem. Phys. **4**, 1 (1962).

[70] T. Munakata and Y. Kaneko, Phys. Rev. E **47**, 4076 (1993).

[71] S. Redner, *A Guide to First-Passage Processes*, Cambridge University Press, New York, 2001.

[72] S. N. Majumdar, Phys. Rev. E **56**, R40 (1999).

[73] B. Yurke, S. N. Pargellis, S. N. Majumdar, and C. Sire, Phys. Rev. E **56**, R40 (1997).

[74] S. N. Majumdar, C. Sire, A. J. Bray, and S. J. Cornell, Phys. Rev. Lett. **77**, 2867 (1996).

[75] E. Ben-Naim, Phys. Rev. E **53**, 1566 (1996).

[76] A. J. Bray, B. Derrida, and C. Godrèche, Europhys. Lett. **27**, 175 (1994).

[77] S. N. Majumdar and C. Sire, Phys. Rev. Lett. **77**, 1420 (1996).

[78] R. Gutiérrez, R. Gutiérrez-Sánchez, and A. Nafidi, Appl. Math. Comput. **175**, 628 (2005).

[79] C. Albanese, G. Campolieti, P. Carr, and A. Lipton, Risk, December 2001, page 99.

[80] C. Godrèche and J. M. Luck, J. Stat. Phys. **104**, 489 (2001).

[81] S. C. Lim and S. V. Muniandy, Phys. Rev. E **66**, 021114 (2002).

[82] E. Lutz, Phys. Rev. Lett. **93**, 190602 (2004).

[83] S. Zapperi, P. Cizeau, G. Durin, and H. E. Stanley, Phys. Rev. B **58**, 6353 (1998).

[84] F. Colaiori, S. Zapperi, and G. Durin, J. Magn. Magn. Mater. **272–276**, e533 (2004).

[85] H. C. Fogedby and V. Poutkaradze, Phys. Rev. E **66**, 021103 (2002).

[86] H. C. Fogedby, Phys. Rev. E **68**, 051105 (2003).

[87] H. C. Fogedby and R. Metzler, Phys. Rev. E **76**, 061915 (2007).

[88] D. Poland and H. A. Scheraga, *Theory of Helix-Coil Transitions in Biopolymers*, Academic Press, New York, 1970.

[89] J. Chuang, Y. Kantor, and M. Kardar, Phys. Rev. E **65**, 011802 (2001).

[90] A. J. Bray, Phys. Rev. E **62**, 103 (2000).

[91] M. Horibe, A. Maroya, and J. Sahamoto, Progr. Theor. Phys. **70**, 1636 (1983).

[92] V. Stohny, Nonlin. Math. Phys. **4**, 132 (1997).

[93] K. Pesz, J. Phys. A **35**, 1827 (2002).

[94] P. E. Kloeden and E. Platen, *The Numerical Solution of Stochastic Differential Equations*, Springer, Berlin, 1992.

[95] R. Mannella, Phys. Lett. A **254**, 257 (1999).

[96] G. N. Watson, *A Treatise on the Theory of Bessel Functions*, University Press, Cambridge, 2nd edition, 1962.

[97] I. S. Gradshteyn and I. M. Rhyzhik, *Table of Integrals, Series, and Products*, Academic Press, New York, 1965.

[98] W. Feller, *An Introduction to Probability Theory and Its Applications*, volume 2, Wiley, New York, 3rd edition, 1971.

[99] S. Karlin and H. M. Taylor, *A Second Course in Stochastic Processes*, Academic Press, New York, 2nd edition, 1981.

[100] M. J. Kearney and S. N. Majumdar, J. Phys. A. **38**, 4097 (2005).

[101] A. Zettl, *Sturm-Liouville Theory*, AMS, Providence, 2005.

[102] E. A. J. F. Peters and T. M. A. O. M. Barenbrug, Phys. Rev. E **66**, 056702 (2002).